Fluid Molecular Layers at the Interface between Mica and 2D Materials Investigated by Optical Spectroscopy and Scanning Force Microscopy

Dissertation

zur Erlangung des akademischen Grades

doctor rerum naturalium (Dr. rer. nat.)

im Fach Physik: Experimentalphysik

Eingereicht an der

Mathematisch-Naturwissenschaftliche Fakultät

der Humboldt-Universität zu Berlin

von

M. Sc. Hu Lin

Präsident (komm.) der Humboldt-Universität zu Berlin:

Prof. Dr. Peter Frensch

Dekan der Mathematisch-Naturwissenschaftlichen Fakultät:

Prof. Dr. Elmar Kulke

Gutachter/innen: 1. Prof. Dr. Jürgen P. Rabe

2. Prof. Dr. Igor M. Sokolov

3. Prof. Dr. Norbert Esser

Tag der mündlichen Prüfung: 28.06.2022

Zusammenfassung

Zweidimensionale (2D) Materialien , wie *z.B.* Graphen oder Übergangsmetalldichalkogenide weisen einige bemerkenswerte mechanische Festigkeiten und eine große Bandbreite an elektronischen Bandlücken auf, die sie zu vielversprechenden Kandidaten für unterschiedliche Technologien macht. Die 2D-Natur führt dazu, dass ihre Eigenschaften sehr empfindlich auf die unmittelbare Umgebung reagieren. So genügt *z. B.* Wasser aus der Umgebung kann entweder an den Oberflächen der 2D-Materialien adsorbieren oder an den Grenzflächen zu festen Substraten interkalieren, wodurch die Eigenschaften der 2D-Materialien zu verändern. Wasser ist in der Umgebung allgegenwärtig, und sein Einfluss auf die 2D-Materialien ist ein komplexes Thema, insbesondere da Wasser in einer dünnen Schicht andere Eigenschaften aufweist als Wasser in einem großen Volumen. Diese Arbeit zielt einerseits auf ein besseres Verständnis der strukturellen Eigenschaften von Wasser an der Grenzfläche zwischen 2D-Materialien und Muskovit-Glimmer, auf den sie exfoliert wurden, sowie andererseits auf den Einfluss des Wassers auf die Eigenschaften der 2D-Materialien.

Experimentelle Untersuchungen von Wasser auf 2D-Materialoberflächen unter Umgebungsbedingungen mit Hilfe von Rastersondenmikroskpie (SPM) sind ziemlich schwierig. Bei Abbildung der Wasserschichten kann die Kapillarkraft zwischen der SPM-Spitze und den Wasserschichten deren Struktur leicht stören. Daher ist die Untersuchung von Wasser, das an der Grenzfläche zwischen 2D-Materisl und Substrat eingeschlossen ist, besser möglich, da die 2D-Materialien die Wasserschichten vor der Störung durch die SPM-Spitze schützen. Allerdings ist die Art der eingeschlossenen Wasserschichten bei Umgebungsbedingungen umstritten, sowie auch ihr Einfluss auf die Eigenschaften der 2D-Materialien. Es ist auch ziemlich schwierig, einen möglichen Unterschied zwischen Wasser, das auf Oberflächen adsorbiert ist, und Wasser, das durch eine Grenzfläche eingeschlossen ist, zu untersuchen. Daher sind große Anstrengungen erforderlich, um grundlegende Fragen zu verstehen, wie *z. B.*: *Welche Dynamik haben die Wassermoleküle, die die Grenzfläche zwischen 2D-Material und Glimmer benetzen? Wie beeinflusst der Benetzungsprozess die elektronischen Eigenschaften der 2D-Materialien, z. B. die Ladungsdotierung? Beeinflussen Wassermoleküle auf der Oberfläche des 2D-Materials diese Eigenschaften ebenfalls? Und wie beeinflussen Wassermoleküle, die zwischen 2D-Materialien und Glimmersubstrat eingeschlossen sind, die Reibung an dieser Grenzfläche?.* Diese Fragen sind von praktischer Bedeutung für den Einsatz von 2D-Materialien in Filtrationsmembranen oder nanoelektronischen Geräten sowie bei tribologischen Anwendungen. Darüber hinaus können die Eigenschaften von 2D-Materialien durch weitere Umgebungskomponenten und Verunreinigungen beeinflusst werden.

In dieser Arbeit verwendete ich ein mechanisches Exfoliationsverfahren, um

ultrasaubere Graphen- und Molybdändisulfid (MoS_2)-Monoschichten auf trockenem Glimmer herzustellen. Die In-situ-Rasterkraftmikroskopie (SFM) wurde eingesetzt, um den Benetzungsprozess von Wasser an der Grenzfläche zwischen trockenem 2D-Material und Glimmer zu visualisieren, während die Proben feuchtem Stickstoff ausgesetzt waren. *In-situ* Raman- und Photolumineszenzmessungen (PL) wurden durchgeführt, um zu untersuchen, wie sich die Ladungsdotierung von Graphen und die Dehnung von Graphen und MoS_2 bei der Benetzung verändern. Um die Mechanismen hinter den Dotierungs- und Dehnungsänderungen durch die eingeschlossenen Moleküle besser zu verstehen, wurden auch Proben untersucht, die organischen Lösungsmitteln (Ethanol, Aceton und 2-Propanol) ausgesetzt waren.

SFM-Ergebnisse zeigen, dass Wassermoleküle, die die trockene Grenzfläche benetzen, bei hoher relativer Luftfeuchtigkeit (RH) eine homogene monomolekulare Schicht ausbilden. Aus Raman-Messungen kann man schließen, dass die Wasserschicht den bei im Trockenen exfolierten Graphen vorhandenen Ladungstransfer vom Glimmer zum Graphen blockiert, während eine Schicht aus Ethanolmolekülen dafür nicht ausreicht. Der Austausch von Ethanol gegen Wasser und umgekehrt ermöglicht eine reversible Umschaltung des Ladungstransfers an der Grenzfläche. Die Ergebnisse lassen sich erklären, wenn man annimmt, dass sich Wassermoleküle, die auf die Graphen-Glimmer-Grenzfläche beschränkt sind, selbst zu einer dipolaren Schicht anordnen, während Ethanolmoleküle weniger geordnet sind. Die Dipolschichten verändern den Ladungstransfer an der Grenzfläche, indem sie elektrostatische Potentialunterschiede an der Grenzfläche erzeugen. Es wird jedoch kein offensichtlicher Einfluss von Wassermolekülen auf 2D-Materialoberflächen beobachtet. Diese Modifikation des Ladungstransfers durch die Flüssigkeiten ist von Interesse für ein besseres Verständnis der Funktionen möglicher hybrider anorganisch-organischer elektronischer Bauelemente.

Es werden nicht nur die Eigenschaften der 2D-Materialien durch die interkalierten Molekularschichten bestimmt, sondern auch die Eigenschaften der molekularen Schichten durch Veränderungen in den 2D-Materialen. Zum Beispiel ändert sich die mechanische Gleitfähigkeit von Graphen auf Glimmer durch eine eingeschlossene Wasserschicht dramatisch. Dies wird in dieser Arbeit durch Dehnung eines Glimmersubstrats mit darauf exfoliertem 2D-Material untersucht. Die dadurch induzierte Dehnung in Graphen und MoS_2 wird durch die Analyse der Veränderungen in den Raman- *bzw.* PL-Spektren ermittelt. Dabei kann eine Dehnungsrelaxation in Graphen beobachtet werden, die sich von einer *„Stick-Slip-Bewegung“* bei trockener Grenzfläche zu viskosem Relaxationsverhalten verändert, wenn Wasser in die Grenzfläche interkaliert. Für Ethanol wird eine schnellere Dehnungsrelaxation von Graphen beobachtet, was auf eine höhere Schmierfähigkeit von Ethanol hindeutet. Im Gegensatz dazu findet man in MoS_2 unabhängig von der Hydratation keine viskose Relaxation. Die Verwendung von 2D-Materialien als Dehnungssensoren bietet einen Ansatz für die Untersuchung der Auswirkungen von Flüssigkeiten auf die Reibung an den Grenzflächen.

Schlüsselwörter: graphen, Molybdändisulfid (MoS_2), flüssige molekulare Schichten, Grenzfläche, Dotierung, Dehnung, Rasterkraftmikroskopie (SFM), Raman-Spektroskopie

Abstract

Two-dimensional (2D) materials, such as graphene or transition metal dichalcogenides, exhibit remarkable mechanical strengths and a broad range of electronic bandgaps, rendering them promising candidates for various technologies. The 2D nature causes their properties to be also highly sensitive to their environments: *e.g.*, ambient water can either adsorb onto the 2D material surfaces, or intercalate at their interfaces with solid substrates, possibly modifying the 2D material properties. Ambient water is ubiquitous and its influence on the 2D materials is a complex issue, especially since the properties of interfacial water may differ from the bulk. This thesis aims at a better understanding of the structural properties of water confined at the interfaces of 2D materials exfoliated on muscovite mica, and its influence on the properties of the 2D materials.

Experimental studies of water on 2D material surfaces under ambient conditions using scanning probe microscopy (SPM) are rather difficult. when imaging the water layers, the capillary force between the SPM tip and water layers can easily disturb their structures. Studying water confined at the 2D material–substrate interface is better feasible, as the 2D materials protect the water layers from the SPM tip perturbation. However, the nature of the confined water layers at ambient conditions is disputed, and also their influences on the properties of 2D materials are in debate. It is rather difficult to investigate a possible difference between water on surfaces and that confined to interfaces. Therefore, major efforts are required to understand fundamental questions like *What is the dynamics of water molecules wetting the 2D material/mica interface? How does the wetting process influence the electronic properties of 2D materials such as charge-doping? Do water molecules on the 2D material surface also influence these properties? And how do water molecules confined between 2D materials and mica substrate influence interfacial frictions?*, *etc*. These problems are practically important for 2D materials used in filtration membranes, nano-electronic devices, and tribological applications. Furthermore, the 2D material properties may be influenced by ambient components and contaminations.

In this work, I employ a mechanical exfoliation method to produce ultra-clean graphene and molybdenum disulfide (MoS_2) monolayers on dry mica. *In-situ* scanning force microscopy (SFM) was used to visualize the wetting process of water at the dry 2D material/mica interface upon exposing samples to humid nitrogen. *In-situ* Raman and photoluminescence (PL) measurements are performed to probe how the charge-doping of graphene, and strain of graphene and MoS_2 change upon wetting. To better understand mechanisms behind the charge-doping and strain changes with the confined molecules, samples exposed to organic molecules (ethanol, acetone, and 2-propanol) were also investigated.

SFM results show that water molecules wetting the dry interface form a monomolecular layer at high relative humidity (RH). From Raman results, it can be concluded that the water layer blocks charge transfer from mica to graphene present in dry conditions, while a layer of ethanol molecules allows for it. Exchanging ethanol and water allows reversibly switching the interfacial charge transfer. The results can be explained assuming that water molecules confined to the graphene-mica interface self-assemble into a dipolar layer, while ethanol molecules organize in a less ordered fashion than water. The dipole layers modify the interfacial charge transfer by producing electrostatic potential differences across the interface. However, no obvious influence of water molecules possibly adsorbed on 2D material surfaces is observed. This charge transfer modification by the volatile liquids is of interest for better understanding of functions of hybrid inorganic−organic electronic devices.

The property changes of 2D materials are determined by the intercalated molecular layers. Similarly, the characteristics of the molecular layers can be also reflected through the changes in 2D material properties, *e.g.*, the mechanical slip of graphene on mica changes dramatically due to the intercalated water layer. This is investigated in this work by stretching a mica substrate with 2D material exfoliated on it. The strain induced in graphene and MoS_2 is inferred by analyzing changes in Raman and PL spectra, respectively. Strain relaxation in graphene changes from *stick-slip* for dry interface to *viscous* when intercalated by water. Faster strain relaxation of graphene on an intercalated ethanol layer implies higher lubricity of ethanol. In contrast, there is no viscous relaxation in MoS_2 regardless of hydration. Using 2D materials as strain sensors provides an approach for investigating the impact of confined liquids on interficial frictions.

Keywords: graphene, molybdenum disulfide (MoS_2), liquid molecular layers, interface, doping, strain, scanning force microscopy (SFM), Raman spectroscopy

Contents

List of Abbreviations

2D	Two-dimensional
SLG	Single-layer graphene
MoS_2	Molybdenum disulfide
h-BN	Hexagonal boron nitride
WS_2	Tungsten disulfide
SFM	Scanning force microscopy
PL	Photoluminescence
MD	Molecular dynamics
UHV	Ultra-high vacuum
SPM	Scanning probe microscopy
RH	Relative humidity
STM	Scanning tunneling microscope
EM	Electromagnetic
IR	Infrared
DR	Double resonance
TR	Triple resonance
FWHM	Full width at half maximum
PMT	Photomultiplier tube
CCD	Charge-coupled device
vdW	Van der Waals

1. Introduction

1.1 Motivation

Two-dimensional (2D) materials are a generic term for a group of materials that have atomic layer thickness in one dimension and relatively larger dimensions in the other two dimensions. In 2004, *K. S. Novoselov* and *A. K. Geim* first obtained the 2D material, single-layer graphene (SLG), from highly oriented pyrolytic graphite by mechanical exfoliation.[1] Graphene exhibits extraordinary properties in many aspects, *e.g.*, large charge mobilities (~10^4 cm^2/ (V·s)) at room temperature.[2] Since then, 2D materials have been developed rapidly, and many new materials have sprung up, such as molybdenum disulfide (MoS_2), tungsten disulfide (WS_2), hexagonal boron nitride (h-BN) and so on. These emerging 2D materials have different bandgaps, covering material types from superconductors, metals, semimetals, semiconductors to insulators. Therefore, they are expected to be used in many fields such as high-performance electronic and optoelectronic devices. Modification of their properties is an important topic in the development of 2D materials, where doping, strain engineering and alloying, *etc*, can be employed to maximize advantages of these materials and avoid their shortcomings. However, due to the 2D nature, properties of these materials are highly sensitive to their surroundings. For example, ambient water adsorbed on graphene affects its electronic properties due to its unique π-electron structure.[3] The susceptibility of graphene properties to the environment is crucial for graphene applications such as transistors and sensors.

Since water covers almost every interface in reality, studying water confined at interfaces comprising of 2D materials and solid substrate surfaces not only contributes to understanding of properties of water confined to nanoscale but also facilitates 2D materials practical applications. Properties of water adsorbed at interfaces and confined to nanoscale are of fundamental and practical importance for understanding various phenomena in geology, biology, tribology, and nanotechnology.[4-7] Properties of water confined to nanoscale are considerably different from those of bulk.[8] Understanding of nano-confined water properties is essential for developing new nano-technological applications. For example, graphene-based membranes were designed for single-molecule filtrations function by confining flows to molecular scales.[9] An improved understanding of this is still required.

Research efforts on water adsorbed on solid surfaces have been undertaken theoretically and experimentally.[10] The early theoretical simulations suggested water molecules can adsorb on hexagonal crystal metal surfaces via hybridization of oxygen lone-pair and metal orbitals, and they can also bond to each other through intermolecular hydrogen bonding. Both O-metal orbital hybridization and hydrogen

bonding are weak bonds with comparable energy. The energy balance between the two weak bond types results in water clusters of various configurations at the interfaces. With the advancement of microscope techniques, the simulation results were confirmed experimentally and diverse water clusters were observed on different substrates in ultra-high vacuum (UHV) and cryogenic temperature conditions. However, experimental access to such structures under ambient conditions is challenging, *e.g.*, direct imaging of water layers by scanning probe microscopy (SPM) utilizing physical probes disturbed the layer structure.[11-14] Recently, graphene coating was employed to protect the water layers from the direct interaction with tips used in SPM.[15-24] It has been shown that graphene, an impermeable and flexible cover,[25-27] lying on mica, an atomically flat natural crystal,[28, 29] protects the water layer from the direct interaction with the SPM tip. Moreover, graphene is highly flexible, such that it replicates the topography of the water layer consequently making it possible to image the water layer. Thus, graphene cover is a promising tool to get experimental access to the behavior of ultrathin films of water as well as other fluids.[15, 17, 18, 21-24, 30, 31] The scanning force microscopy (SFM) study on ambient water trapped between SLG and mica was pioneered by *Xu et al*.[15] The SFM topographic imaging of the trapped water revealed water islands with a uniform thickness of 0.37 nm and multiple 120^{o} corners. This was explained with the water islands being the I_h-ice – the bilayer structure of ordinary ice in nature.[32] The seminal work attracted attention to this field. The subsequent studies not only addressed structural properties and dynamics of the nanoscale liquids,[16, 17, 24, 30, 31, 33] but they also investigated the effects of the intercalated liquids on the confinement,[18, 21, 23, 34-36] *e.g.*, the graphene-mica interface determines the orientation of the intercalated water molecules, meanwhile the confined water influences graphene charge-doping as well.[8] Graphene electronic properties are reported to be very sensitive to both substrates[37-41] and intercalated liquid layers.[18, 34, 39, 40, 42, 43] Thus, a better understanding of the confined liquid layers in nano-slit pores is also envisioned as a promising way to better control graphene properties.

Although the studies using the graphene-mica slit pore are successful and fruitful, the structure and properties of water layers confined in the slit pore remain disputed to some extent. One of the arguments focuses on the number of the water layers confined in the silt pore and their phases under ambient conditions. For example, the early interpretation of two confined water layers being ice-like was challenged later by other researchers.[15] The thickness of the second water layer was later found to be larger than that of the first one.[33] This was attributed to the fluid-like structure of the second water layer, which is less ordered than the ice-like first layer. The role of the water dipoles in the slit pore on tuning charge transfer between graphene and mica remains also debated. Whether the confined water layers can *p*- or *n*-dope, or undope graphene requires further investigation. Moreover, the water molecules adsorbed on graphene top surface may also influence its doping properties. How to distinguish this from the influence of the

confined water at the graphene-mica interface is another challenge. These debates and challenges led to the following targets that I will pursue in my Ph.D. work. 1) Employing SFM and Raman spectroscopy to determine the influence of intercalated liquid films on graphene and MoS_2 properties, particularly concerning graphene charge-doping and strain. Doping and strain are both important effects to graphene application in practice, *e.g.*, both effects can alter graphene electronic band structure and possibly open its bandgap, which is essential for applications such as transistors;[44-46] strain can tune sliding frictions between graphene and substrates, which is vital in tribology.[47] 2) Through *in situ* SFM and Raman measurements on graphene when being wetted by liquids, to obtain a deeper understanding on structural properties and dynamics of the thin confined liquid films as well as their influences on the graphene-mica system. Fulfilling these two targets may allow answering some of the abovementioned questions, such as the structural properties of the water layers confined in the slit pore, the effect of water dipoles on tuning both the interfacial charge transfer and friction, *etc*.

1.2 Overview of the Thesis

I describe in the following the outline of my thesis.

In **Chapter 2** I will provide some background information related to my work. For example, a brief overview of studies of water adsorption on solid surfaces including metals and non-metals such as mica is first described. Then I describe components of the graphene-mica experimental system, *i.e.*, structures and properties of graphene as well as mica, and the tape-free mechanical exfoliation method I used to prepare clean and flat graphenes on mica in this work. In addition, some fundamentals about Raman scattering are introduced.

In **Chapter 3** I will review previous SFM and Raman investigations performed on the graphene-mica slit pore system by other researchers. The first section shows SFM topographic profiles of water and its dynamics as a function of relative humidity (RH) in the slit pore, as well as the disputations on the water layer structure at the molecular level. The second section focuses on Raman spectroscopy of graphene and characterizations of its charge-doping and strain. Finally, the influence of intercalated water layers on graphene and mica is discussed in detail.

Chapter 4 describes the analytical techniques employed, *i.e.*, SFM and Raman spectroscopy, and experimental home-built setups used in my work.

In **Chapter 5**, the main findings of my work are described and discussed. The first section starts with SFM and Raman investigations of dry and hydrated graphene-mica slit pores. I found that a molecularly thin water layer decoupled dry graphene from the ionic mica surface both mechanically and electronically, resulting

in removing charge-doping and strain of graphene (**Section 5.1**). Then, I describe Raman investigations on graphene not only upon hydration of the slit pore, but also upon replacement of water by organic solvents: ethanol, acetone, and 2-proponal (**Section 5.2**). The results in these two chapters contribute to the understanding of the liquid layer structures and their roles on charge transfer at the graphene-mica interface. With the aid of molecular dynamics (MD) simulations accomplished by my colleague *José D. Cojal González*, I proposed a charge transfer model between graphene electronic states and mica trap states, offset by electrostatic potentials produced by the molecular liquid layers confined in the slit pore. The last section mainly focuses on the time evolution of strain in graphene before and after wetting the slit pore with a water or ethanol layer, respectively (**Section 5.3**). The results showed a transition of strain relaxation in graphene from *stick-slip* in dry contact, to *viscus* when hydrated. A faster strain relaxation with the ethanol layer was found than that with the water layer. The experimental method can be extended into investigations of interfacial frictions in other layered materials, *e.g.*, the friction changes between MoS_2 and mica upon interfacial hydration were also studied. But no viscous relaxation was founded with water layer intercalation. The investigations using different 2D materials, different liquids help to understand the lubricity effects of molecular liquid layers at the 2D material-mica interface, and the friction mechanisms at interfaces.

In **Chapter 6**, I summarize the essence of this thesis and propose the prospects of my work based on the current findings.

2. Background

2.1 Water Adsorbed at Interfaces

Water, the most common and abundant substance, is coating almost every surface at ambient conditions. Nano-confined water displays extraordinary structures and properties compared to its bulk.[6, 8, 48-50] For example, water encapsulated in carbon nanotubes may exhibit new ice phases and fast mass transportation.[6, 48, 50] The properties of confined water are associated with the confinement dimension and configuration, and other conditions, *e.g.*, the fast transportation of water in carbon nanotubes was not observed within boron nitride nanotubes.[51] Therefore, understanding water structures and properties in nanoconfined environments is of great importance for both fundamental research and technological applications.

The water-solid interaction has been widely studied with both experimental and theoretical approaches.[11, 52] Among them, well-defined metal surfaces have been frequently used to study water adsorption behavior. The theoretical simulations showed how water monomers absorb on hexagonal crystal metal surfaces.[12, 14, 53] It was generally agreed that water monomers adsorb on or near a top site of metal atoms,[54] with their molecular plane parallel to the metal surfaces (**Figure 2.1a**). The water monomer bonds to the metal through the hybridization of one of its O "lone-pair" orbitals and the metal orbital. The O-metal bonding energy is comparable to the intermolecular hydrogen bond strength (~0.2 eV).[10] The weak binding allows water monomers to diffuse on the metal surface. The competition between the water-metal bonding and water-water hydrogen bonding results in the formation of water dimers and clusters. The motion of water monomers and dimers was observed at temperatures around 40 K with scanning tunneling microscope (STM). However, the mobility of dimers is over three orders of magnitude faster than that of monomers. *Ranea et al*. explained this with the following model: one water molecule bonds to the metal surface through the O-metal bond (as H-bond donor), while the other one connects to it through H-bond (as H-bond acceptor) instead of forming a bond with the metal atom. The water molecule (H-bond acceptor) is farther away from the metal atom compared to the other one (H-bond donor), thus it can rotate freely around the O-metal bond (**Figure 2.1b**).[12] Two water molecules can interchange their roles as the H-bond donor and acceptor, resulting in the faster motion of the dimer. This model was later confirmed experimentally by *Motobayashi et al*.[55] The structure of water clusters on metal surfaces is determined by the energy balance between water-metal and water-water interactions. Such balance leads to diverse configurations of water clusters with different orientations of water molecules. A water molecule may have three common orientations (**Figure 2.1c**), depending on whether its O-atom connects to one or two H-atoms of the

neighbors (Figure 2.1d).

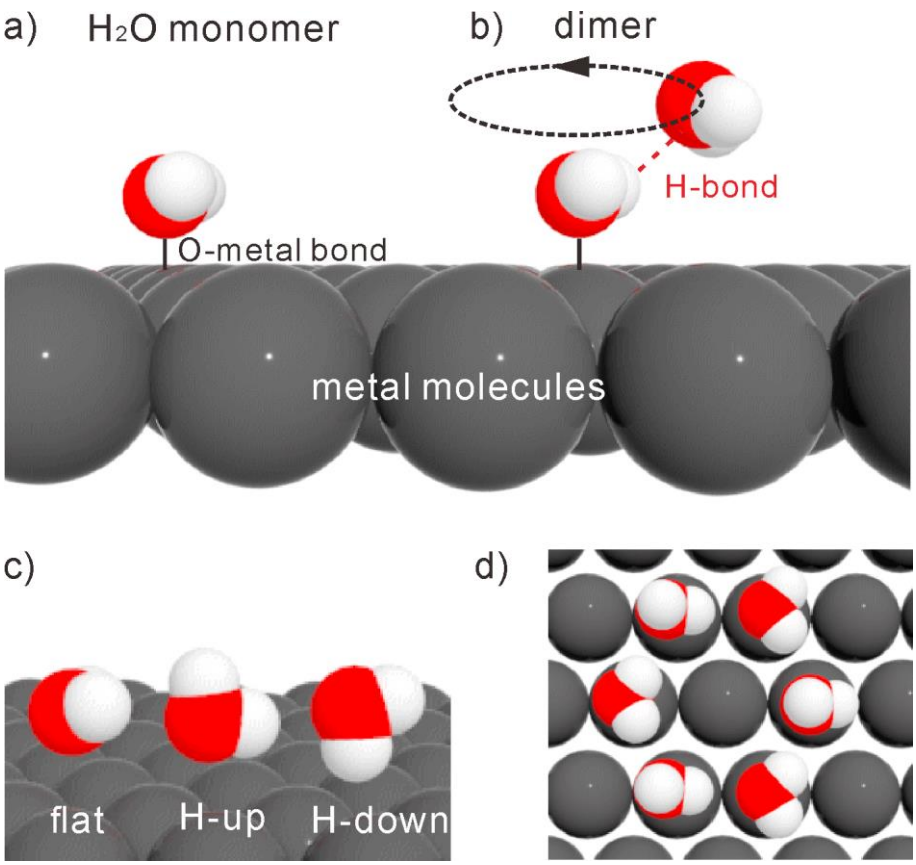

Figure 2.1: Schematic of the typical structure of a a) water monomer and b) dimer adsorbed on a metal surface. c) The three common orientations of water molecules on a metal surface: "flat" and "verticals" ("H-up": H away from the surface, and "H-down": H towards the surface). d) The typical water clusters consist of flat (O connecting to one H-bond) and vertical (O connecting to two H-bonds) oriented water molecules. (Adapted from Ref. [10])

The studies further progressed and different water structures were found on different metal substrates. For instance, one-dimensional water chains were observed on Cu,[56] while a hexagonal structure was observed on both Pd and Ru.[57, 58] The studies on the metal system were mostly theoretical simulations and experimental measurements in UHV condition, since direct imaging of thin water layers without disturbing their molecular structure at ambient conditions was quite difficult. In addition, it is still practically important to investigate interactions between water and other non-metal surfaces at ambient conditions. Over the past decade, the 2D material graphene has been broadly used as an ultrathin coating to study the water films at ambient conditions. This subject quickly attracted attention worldwide, not only because of its experimental feasibility under ambient conditions, but more importantly, it brought further interesting questions. For example, graphene is known to be hydrophobic,[59] what structure and diffusivity will water possess when it is confined between graphene and a hydrophilic substrate such as

mica? Besides, graphene electrons can interact with surroundings due to graphene's 2D structure, which renders graphene electronic properties to be highly sensitive to surface adsorbates. Studying the effects of polar water molecules on graphene electronic properties may pave the way for commercial applications of graphene. Some studies, therefore, attempted to reveal the water structure and diffusion properties at the molecular level, and its interactions with graphene as well as substrates like mica.[17, 18, 20-22, 24, 33, 60-62] It is generally agreed that the hydrogen atoms of water molecules trend to combine with the oxygen atoms of mica forming hydrogen bonds. And this causes water dipoles to take a certain orientation and arrange themselves in a well-ordered structure on the bare mica surface. However, some questions remain disputed, for instance, how many water layers are confined between graphene and mica at ambient conditions? And what is the height of the confined water layers? What is the physical properties of the water layers, ice-like or fluid-like?[15, 17, 20] Moreover, the water layers can influence the local charge-doping of graphene, suppressing or inducing charge-doping?[18, 21, 22, 62] The details will be elaborated in **Chapter 3**. One of the potential reasons for the discrepancies could be different experimental conditions. The foreign molecules in ambient air could preadsorb on the surfaces and influence water and graphene properties. Thus, understanding of surface structures requires a well-defined system with minimal contaminations. In the following section, I will introduce the graphene-mica system used in my work for *in situ* SFM and Raman characterization in well-controlled gas environments.

2.2 A Nano-Confinement Tool for Molecules: Graphene-Mica Slit Pore

2.2.1 Graphene Crystalline, Band Structure and Properties

SLG is a 2D material, which only consists of carbon atoms. The carbon atoms form a hexagonal network. The hexagonal unit cell contains two types of atoms A and B, forming a triangular structure involving A sub-lattice and B sub-lattice, respectively (**Figure 2.2b**). The carbon atoms connect through planar σ-bonds ($a_{c\text{-}c}$ = 1.42 Å). Some defined points in the first Brillouin zone of graphene are displayed in **Figure 2.2c**: the Γ point (at the zone center), and the K and K' points (at the corners of the hexagons). These points are highly symmetrical.[63]

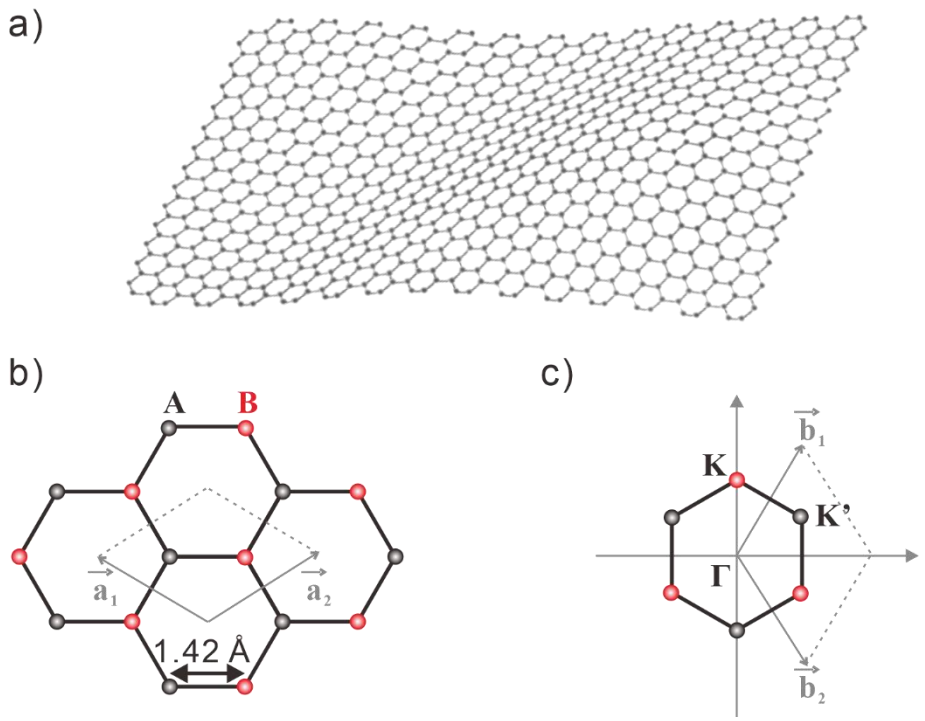

Figure 2.2: a) Graphene sheet. b) The graphene real space unit cell: A sub-lattice (black points) and B sub-lattice (red points), unit vectors $\mathbf{a_1}$ and $\mathbf{a_2}$. c) The first Brillouin zone with some line symmetrical points in its reciprocal space unit cell: the Γ point (at the zone center), the K and K' points (at the corners of the hexagons), and primitive vectors $\mathbf{b_1}$ and $\mathbf{b_2}$.

Covalent bonds form between the sp^2 hybrid orbitals of the neighboring carbon atoms, connecting one another at a 120° angle. As shown in Figure 2.3, the valence band of SLG touches the conduction band directly at the K (or Dirac) point so that SLG is a semiconductor with zero bandgaps. Its electronic structure exhibits linear dispersion near the K point, as shown in the zoom part of Figure 2.3.[64] Each carbon atom contributes a p_z-orbital electron to form a delocalized π bond. The electrons behave as massless relativistic fermions in the crystal, giving graphene excellent electron transport properties.[65]

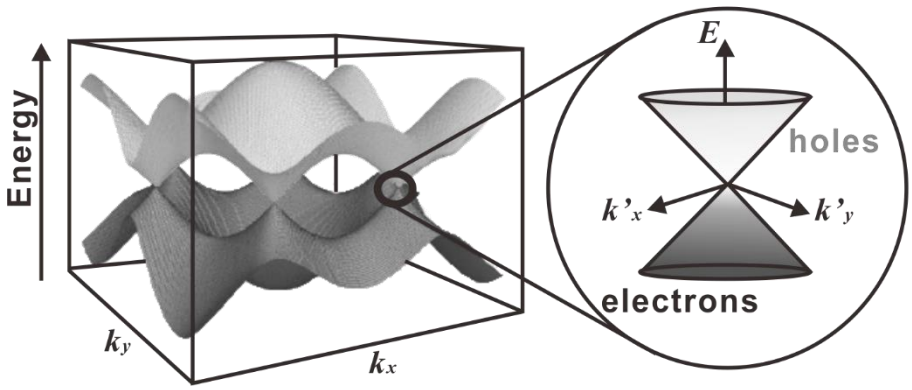

Figure 2.3: Electronic band structure in a unit cell of SLG and zoom near the K point: the linear electronic structure. (Adopted from Ref. [64])

The special structure of SLG gives rise to remarkably mechanical, electronic, and optical properties. Graphene is one of the thinnest materials with a thickness of ~ 0.34 nm, almost the same as one carbon atom. But it was reported that Young's modulus and fracture strength of the free-standing SLG are up to 1 TPa and 130 GPa respectively,[25] which establish graphene as the strongest material. Moreover, the graphene sheet is of great flexibility and impermeability,[26, 27] which can even replicate the topography of the molecular adsorbates on a substrate surface.[15] The charge carriers in graphene exhibit ultrahigh mobilities and the density is sensitive to the external environment.[66, 67] As a result of the special structure and electronic properties, graphene shows amazing transparency (~ 97.7%) to the visible light.[68] Nevertheless, SLG is still detectable on an optically transparent substrate,[69] and the number of graphene layers can be nondestructively identified by Raman spectroscopy.[70] The unique mechanical and optical properties render graphene as a potential ultrathin coating to cover liquid molecules on various substrates, facilitating the studies on structures and properties of liquids at interfaces.

2.2.2 Muscovite Mica Structure and Properties

Muscovite mica is a non-swelling clay material, which belongs to the group of phyllosilicate minerals.[29] I will use the shortcut "mica" to denote "muscovite mica" in this thesis. Mica has a typical layered structure, comprising one octahedral complex aluminum layer sandwiched by two tetrahedral SiO-layers. These 2:1 aluminosilicate layers have negative charges, arising from a substitution of the Si^{4+} ions by Al^{3+} ions. And they are bridged together by interlayers of K^+ cations (**Figure 2.4**), resulting in the electrically neutral mica crystal with a formula unit $KSi_3Al_3O_{10}(OH)_2$.

Mica can be easily split into thin sheets as a result of the weak bonding between the aluminosilicate layers and K^+ cations. It provides an atomically flat, thermally stable, and chemically inert plane after cleavage.[71] Therefore, mica is a favorite substrate for use in SFM.[72] Moreover, mica is birefringent and highly transparent for visible light. It was reported that the 2D material such as graphene on mica exhibits a high contrast by taking advantage of the destructive interference of light reflected from the mica-graphene and graphene-air interface.[69] Mica is hydrophilic and it tends to adsorb water molecules to form a thin film at ambient conditions.[29] Considering all these advantages, mica is one of the substrates of choice for studying water adsorption on non-metal surfaces. Cleavage of mica provides an atomic-level flat and contamination-free surface. Graphene deposited onto cleaved mica creates a clean slit nanopore, which water molecules can intercalate into.

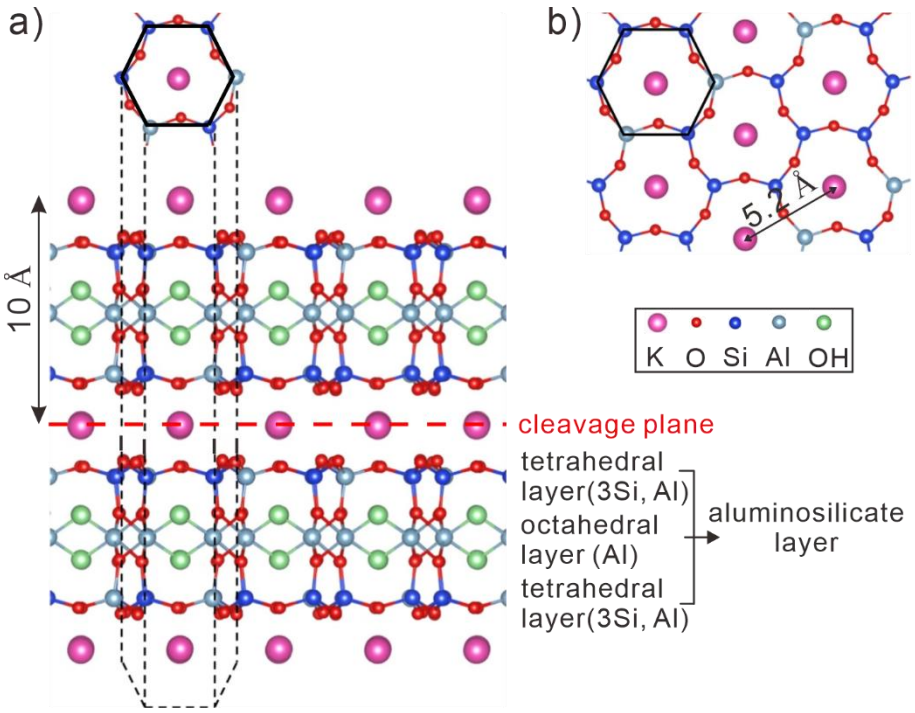

Figure 2.4: a) Side- and b) top-view schematic of mica crystal structure. (Adapted from Ref.[73])

2.2.3 Graphene-Mica Slit Pore Prepared by Mechanical Exfoliation

Graphene covering water on an atomically flat mica surface can replicate the topography of the water film.[15] This system has been considered therefore as a model for a soft slit pore, which enables high-resolution imaging of its content by SFM.[17] The slit pore has been extensively used to investigate the properties of liquids confined at the graphene-mica interface.[28, 30, 31, 74] However, it was reported that ambient O_2 and CO_2, airborne contaminations preadsorbed on substrates could influence the properties of the graphene and confined liquids. This will complicate the fundamental understanding of liquids in nanoconfinements.[3, 21, 29, 39] Therefore, it is essential to produce high-quality graphenes almost without defects, and contamination-free substrate surfaces. The tape-free mechanical exfoliation of graphite on mica in a dry glove box is a unique method that fulfills these requirements for research purposes.[75] The preparation process will be introduced in Section 5.1.2. This method provided me an initially dry and clean soft slit pore for studying structural and diffusional properties of confined liquid films as well as their effects at the graphene-mica interface.[17]

2.3 Raman Scattering

Since I used Raman spectroscopy as the primary characterization method to measure the graphene samples in this work, I will use this section to introduce some background about Raman scattering to facilitate understanding of my Raman results

later on. Raman scattering is used to investigate molecular properties through Raman-scattered light, discovered by *Raman* and *Krishnan* in 1928.[76] In recent decades, Raman spectroscopy has been developed and utilized as a powerful technique to characterize graphene and other 2D materials. It is a non-destructive, rapid, and versatile tool, which is widely used to study graphene's physical properties such as doping, strain, number of layers, and defects.[63, 77] In this section, I will explain the fundamentals of Raman scattering. Raman scattering results from inelastic photon-molecule interactions when a light wave meets a molecule. The "inelastic interaction" process is accompanied by an exchange of energy. Because the total quantity of energy must be conserved, the energy gained (lost) by the photon must equal the energy lost (gained) by the molecule. The energy change of the photon can be measured and calculated thereby as the change in molecular vibrational energy. These changes are in essence, transitions between different molecular vibrational energy levels. Thus, it is possible to probe the molecular vibrations by monitoring the inelastically scattered photons, and the Raman spectrum provides information on molecular vibrations.

When a light wave meets a molecule composed of electrons and nuclei, the electric field *E* of the light exerts a force on all electrons, and tends to displace them from their average positions around the positively charged nuclei. Such distortion results in an induced dipole moment μ in the molecule, and the molecule becomes polarized:[78]

$$\mu = \alpha E \tag{2.1}$$

where α is called the electric polarizability of the molecule, it signifies how easily a molecule can be distorted to create a dipole moment. In the following, I will take a diatomic molecule for example, the incident light causes the two nuclei to leave their initial positions. And this will vary the molecule's polarizability α. Let's suppose before interacting with light, the molecule is in its equilibrium geometry with polarizability α_0. At a certain displacement $\Delta\gamma$ away from the equilibrium, the instantaneous polarizability is:

$$\alpha = \alpha_0 + \frac{d\alpha}{d\gamma}\Delta\gamma \tag{2.2}$$

For molecular vibrations, $\Delta\gamma$ can be expressed as a sinusoidal function:

$$\Delta\gamma = \gamma_{max}\cos(2\pi\nu_{vib}t) \tag{2.3}$$

where γ_{max} is the vibrational amplitude, ν_{vib} is the vibrational frequency, and t is the time. The electric field in the light wave can be also written in a sinusoidal form:

$$E = E_{max}\cos(2\pi\nu_0 t) \tag{2.4}$$

where v_0 is the light frequency, E_{max} is the field amplitude. Now let's combine all these equations above and obtain:

$$\mu = \alpha_0 E_{max} \cos(2\pi\nu_0 t) + \tag{2.5}$$

$$\frac{1}{2}\frac{d\alpha}{d\gamma}\gamma_{max}E_{max}\cos 2\pi(\nu_0 + \nu_{vib})t + \frac{1}{2}\frac{d\alpha}{d\gamma}\gamma_{max}E_{max}\cos 2\pi(\nu_0 - \nu_{vib})t$$

Equation (2.5) demonstrates that when a light wave interacts with a vibrating molecule, the induced dipole moment has three frequency components. The oscillating dipole emits electromagnetic (EM) radiation itself with the three different frequencies. The first part of the equation describes vibration with the frequency v_0, which is the frequency of the incoming light. EM radiation by the molecule that has the same v_0 as the incoming light is known as Rayleigh scattering. The second part of the equation contains two cosines. The $(\nu_0 + \nu_{vib})$ relates to an outgoing, scattered photon that has a larger frequency. The difference v_{vib} is the frequency of the molecular vibration. The other cosine contains the variable $(\nu_0 - \nu_{vib})$, which stands for a scattered photon that decreases its frequency by the same amount v_{vib}. The above provides a simplified classical picture of Raman scattering. Noteworthy, if the derivative $\frac{d\alpha}{d\gamma}$ in **equation (2.5)** equals zero, there will be no Raman scattering, although the whole dipole moment μ might change. Thus, a molecular vibration will be Raman-active only if the vibration occurs with changing of polarizability α.[78] This is opposite to infrared (IR) spectroscopy, where those vibrations with a change of dipole moment μ are IR-active and visible. To easily understand this, let's check the symmetric and asymmetric stretch of a carbon dioxide molecule (**Figure 2.5**). For molecules with a center of symmetry like carbon dioxide, the symmetric stretch is only Raman-active, because it results in a change of the overall molecular polarizability α but no change in the net molecular dipole μ. While in the asymmetric stretch, the overall molecular polarizability does not change as the longer bond change is exactly offset by the shorter one. But the net molecular dipole changes and renders the asymmetric stretch IR-active. Of course, for complex molecules with different elements of symmetry, certain vibrations may be both Raman and IR active. In general, Raman spectroscopy and IR spectroscopy provide complementary information on molecular vibrations.

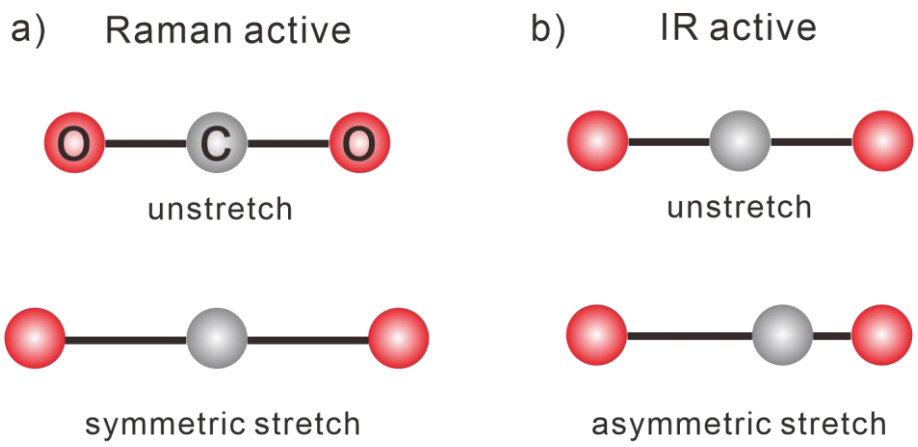

Figure 2.5: Representation of a) Raman-active symmetric stretch and b) IR-active asymmetric stretch of a carbon dioxide molecule. The symmetric stretch causes a change in polarizability α, while the asymmetric one induces a change in dipole moment μ.

From the quantum mechanical view, the basis of Raman spectroscopy is that incident photons excite molecules to gain energy and move to a virtual energy state (or level). The term "virtual energy state" refers to a short-lived intermediate state, which does not correspond to a quantized energy state of a molecule. If the molecule relaxes back to the ground state v_0 and emits a photon of energy equal to that of the incident photon. This is called elastic scattering with no exchange in energy, and the process is known as Rayleigh scattering. It is the dominant effect and does not change the frequency of the incident light. If the scattering is not elastic, firstly, the molecule can relax to a real vibrational state v_1 (higher than the ground state v_0) and emit a photon with less energy than the incident photon. This process is called Stokes shifted Raman scattering corresponding to the part $\cos 2\pi(\nu_0 - \nu_{\mathrm{vib}})$ in **equation (2.5)**. Secondly, if the molecule is already in a vibrational state v_1 before meeting with incident photons, it can be excited to a higher virtual state and then relaxes back to the ground state v_0 by emitting a photon with more energy than the incident one. This is called Anti-Stokes Raman scattering corresponding to the part $\cos 2\pi(\nu_0 + \nu_{\mathrm{vib}})$ in **equation (2.5)**. Raman scattering leads to a shift of the incident frequency by plus or minus the frequency of the molecular vibration v_{vib}. The energy diagram for Rayleigh and Raman scattering is shown in **Figure 2.6**.[78] Because most molecules stay at the ground state v_0 at room temperature, Stokes Raman scattering happens with higher probability, and most Raman measurements only consider the Stokes shifted effect. In all of the following sections, all mentions of Raman scattering refer to only Stokes Raman scattering as well.

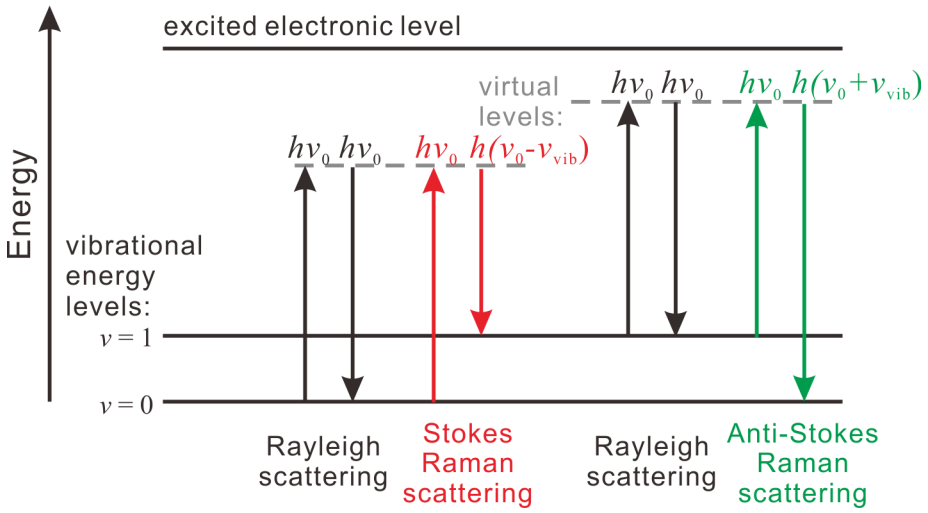

Figure 2.6: Energy diagram of Rayleigh and Raman scattering. v_0, photon frequency. v_{vib}, molecule vibrational frequency. h, Planck constant.

3. Literature Review

3.1 SFM Visualization of Water Confined in Graphene-Mica Slit Pores

SFM investigations of water confined in a graphene-mica slit pore were initiated in 2010.[15] Graphene was mechanically exfoliated onto a freshly cleaved mica at ambient conditions. The sample was imaged with SFM tapping mode, and the structure of water adlayers on mica was determined as a function of RH. Water islands with a uniform thickness of ~ 0.37 ± 0.02 nm were found across the sample (Figure 3.1d). The thickness coincides with the "puckered bilayer" height of the natural ice with an I_h–crystalline form (Figure 3.1b).[11] Besides, some water islands had multiple 120° corners, which was not observed in images of other organic liquid adlayers in a graphene-mica slit pore. Such polygonal shape and thickness suggest the ice-like property of the water layer on mica. And the "puckered bilayer" of I_h-ice was assumed as the structural model for water adsorption on mica.

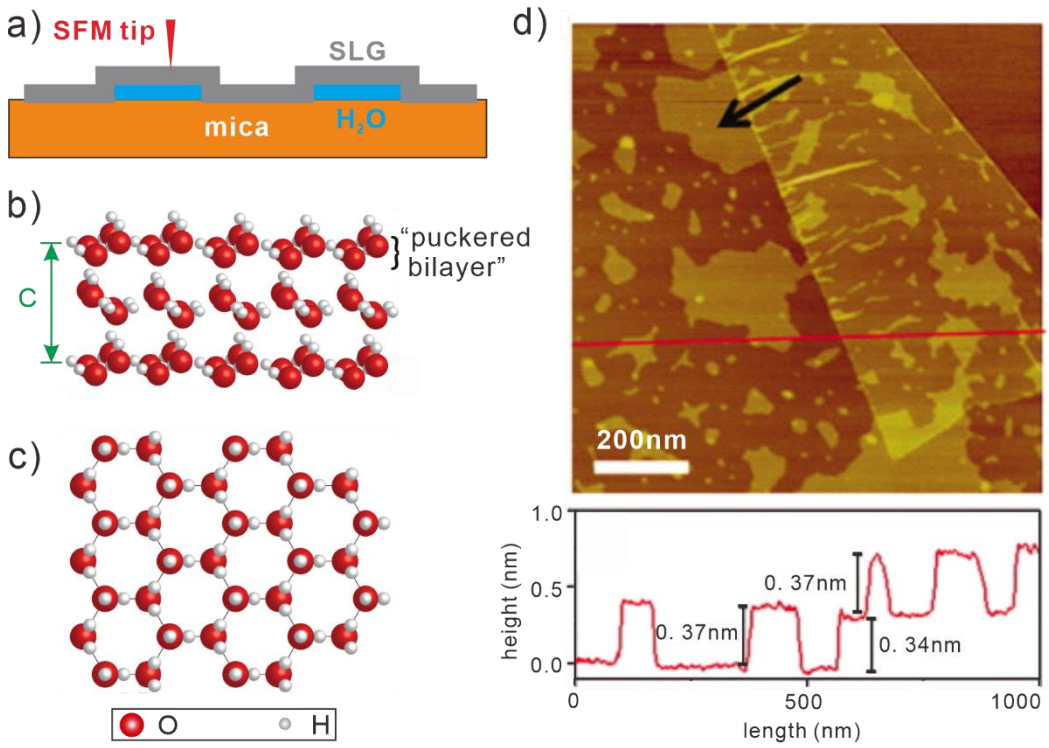

Figure 3.1: a) Schematic of SLG coating a water adlayer on mica visualized by SFM. b) Side and c) top view of the structure of I_h–ice: every water molecule (as a double H-bond donor and acceptor) is hydrogen-bonded to exactly 4 nearest neighbored molecules to form a tetrahedrally-bonded hexagonal structure. The I_h – ice consists of "puckered bilayers", and the interlayer distance is c/2 = 0.37 nm. d) SFM height image of a SLG with the upright edge folded. The black arrow points to a water island with multiple 120° corners. The height profile along the red line is shown below. The step height of the SLG is ~ 0.34 nm, which can

be used to calibrate the height of the water islands (~ 0.37nm) confined in the graphene-mica interface. (Adapted from Ref.[15, 79])

Numerous groups proceeded based on the seminal work.[17, 20, 22, 33, 60, 61, 75] *Severin et al.* posted a different argument on the structure of the water layer afterward.[17] They exfoliated graphite flakes onto a freshly cleaved mica surface in a glove box with less than 5 ppm of each H_2O and O_2. Then SLGs were localized using an optical microscope after exposure to ambient for about half an hour and then transferred to an SFM instrument for measurements. The SFM head was operated inside a home-built bell-jar chamber, purged with either dry nitrogen or dry nitrogen bubble through a water-filled washing bottle. By alternating the dry and humid nitrogen flow, the RH inside the chamber was controlled in the range from 60% to 4%. SLGs were imaged *in situ* in tapping mode, the imaging revealed fractal depressions growing within flat SLG pieces upon lowering of RH (**Figure 3.2**). The fractal depressions appearing upon decreasing RH have a depth of ~ 0.28 ± 0.05 nm, which is comparable to the size of a single water molecule rather than the interlayer distance of I_h-ice. This suggests the water layer to be monomolecularly thin. Furthermore, the fractals disappeared instantly as RH being raised to ~ 50% (**Figure 3.2d**). They attributed this to the fluidity of the water layer, which allows the evaporation and condensation of water from and into the graphene-mica interface respectively. The authors pointed out that the discrepancy in the thickness of the water adlayer might be caused by contaminations from either preparation or air. Later, *Rezania et al.* demonstrated that adhesive tapes often used in the exfoliation method of graphene have a significant influence on both graphene flatness and the fractal structure of the water layer at low RH.[75] She concluded that these were due to contaminations of graphene-mica interfaces by the adhesive tapes.

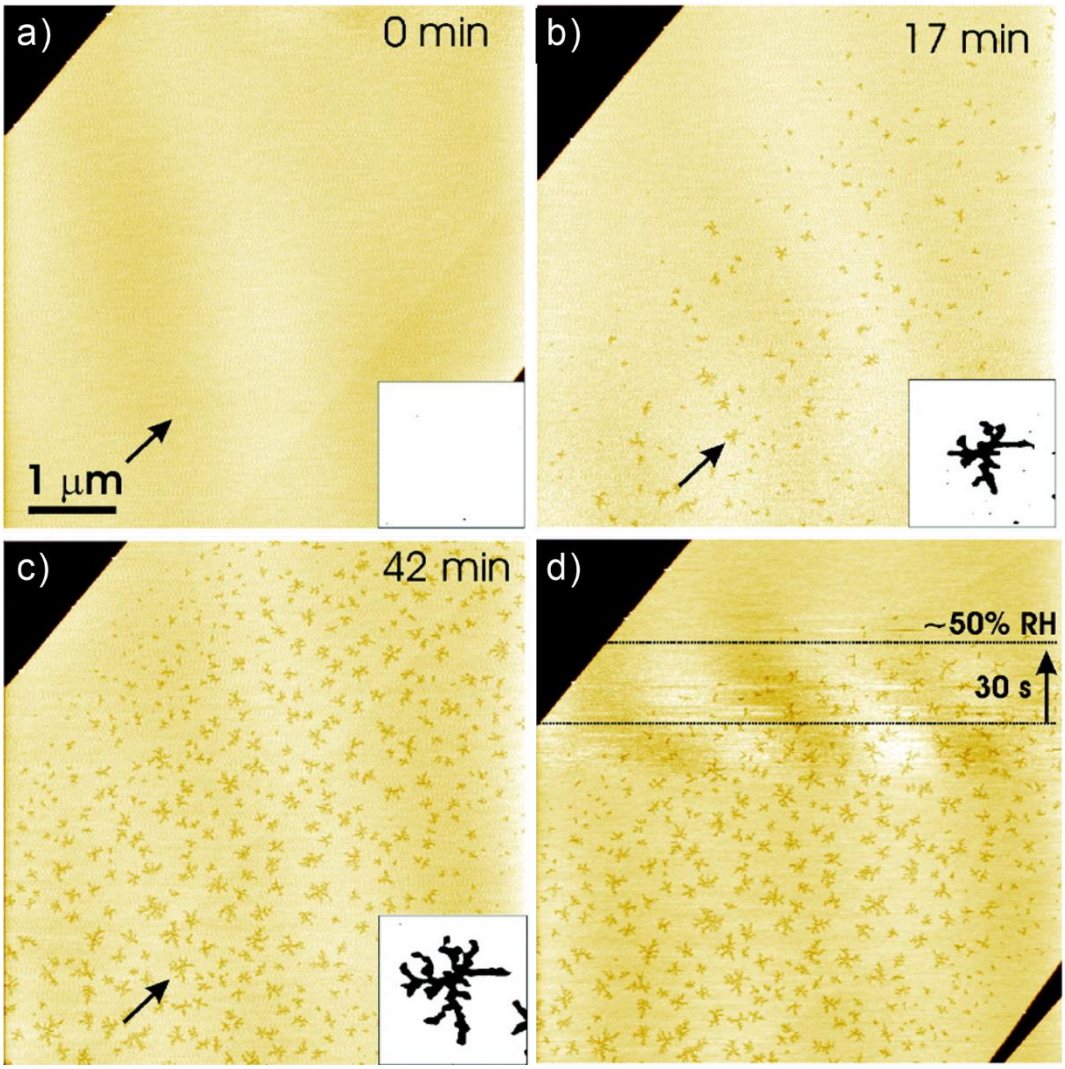

Figure 3.2: SFM height images of a SLG (brighter area) deposited on mica (darker area) under variable RHs. The time noted at the beginning of each scan is indicated directly on the images. Insets show close-ups (400 nm) of the area pointed by arrows, the contrast is strongly exaggerated to leave graphene white and fractals black. a) Initially, SLG was homogeneously flat at ~ 60% RH. b, c) Fractal depressions appeared at RH below 4% and grew over time. d) Upon increasing RH, the SLG became again atomically flat. The slow scan direction is indicated with the vertical arrow. The lines are guides to the eye, which indicate the erasure of fractals occurring in 30 s. A subsequently taken image reveals a flat graphene topography similar to a). (Adapted from Ref.[17])

The SFM provides us the topographic replica of the water adlayers under graphene coating, but insufficient understanding of the confined water structure at the molecular level. To clarify the structure of water film formed on a mica surface, theoretical calculations and computer simulations can be employed. The MD simulations performed by *Odeliu et al.* showed that at monolayer coverage, water molecules on mica condensed into a 2D-ice structure (**Figure 3.3**), which differs from the I_h structure of the natural ice (**Figure 3.1b**).[80] The 2D hydrogen bond network

was stable and was proposed to be ice-like. Based on this, further MD simulations done by *Li* and *Zheng* suggested that the first water adlayer behaved solid-like as it strongly bonds to mica, while the second adlayer was liquid-like under ambient conditions.[60] Graphene coating stabilized the second water adlayer and rendered it ice-like as well, and the first two layers were together about 0.74 nm thick, the same as two puckered bilayers of I_h -ice. However, their results were later experimentally challenged by *He et al*.[33] They characterized the thickness of two water layers trapped between graphene and mica using a carbon nanotube height reference by UHV-STM. They prepared graphene samples via chemical vapor deposition method. And the SLGs were transferred to mica by immersing them in deionized water. The sample was then heated to remove excess water and degassed to remove surface contaminations. Using such wet transfer method, they observed two water layers trapped between graphene and mica. They confirmed that the first adlayer was stable and solid-like due to the strong bonding with mica. In contrast, they argued that the second layer was liquid-like. Because they measured that the height of the second layer was 0.3 nm, smaller than the first layer of 0.4 nm. They attributed the second layer to be less ordered. *Bampoulis et al.* adapted this idea to explain why the fractal depressions observed by *Severin* have a depth of 0.28 ± 0.05 nm.[22] They argued at ambient conditions, two water adlayers were also confined in the graphene-mica slit pore. The first layer was ice-like while the second layer was liquid-like. The fractals were formed due to the incomplete evaporation of the less-ordered water molecules in the second adlayer. In other words, SFM imaging just showed the morphology changes of the top layer. However, this model needs further experimental support because the first layer is difficult to be visualized by SFM.

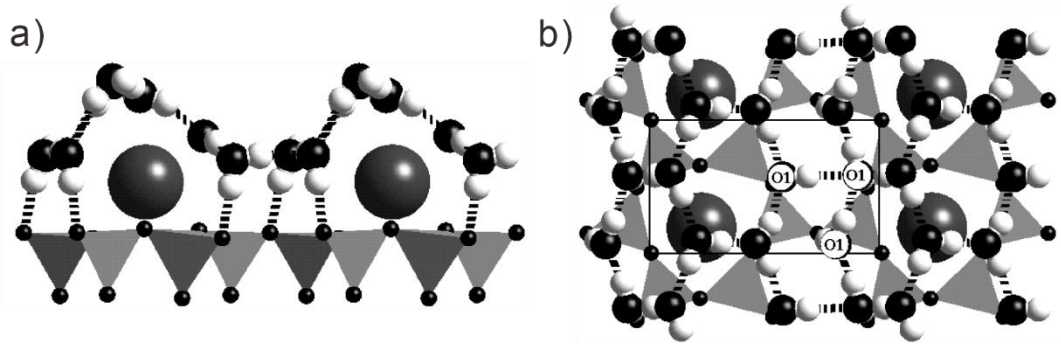

Figure 3.3: the optimized structure of monolayer water on mica shown from a) side and b) top view. Black, white and gray spheres depict oxygen, hydrogen, and potassium atoms, respectively. The polyhedral contains silicon and aluminum in the center. The drawn unit cell of the 2D-ice structure coincides with the unit cell of mica. There are 6 water molecules per unit cell; half of them (donated by O1) are closely bound to the surface by donating hydrogen bonds to basal oxygen atoms. The other water molecules solvate the potassium ions and form bonds to the underlying water molecules and to each other. (Adapted from Ref.[80])

The discrepancies in terms of water structural properties require further investigations. Moreover, since all experimental studies mainly focused on the water trapped between graphene and mica at ambient conditions, it is also interesting to investigate the wetting process of water molecules in an initially dry graphene-mica slit pore by SFM. Likewise, the influences of water adlayers on graphene properties during wetting are also practically important and worthy of investigation. My work, motivated by the previous SFM studies, mainly focuses on investigating how the confined liquid films influence the properties of graphene on mica by Raman spectroscopy. The spectroscopy can help to obtain deeper insight into how intercalating films impact the properties of graphene cover, which would complement the SFM results. To better understand my Raman results in the end, I introduce in the next two sections some fundamentals of Raman spectroscopy of SLG.

3.2 Raman Characterization of Graphene: Doping and Strain

3.2.1 Raman-Active Phonon Modes and Raman Fingerprint of SLG

Phonons describe the elementary vibrational motion of atoms or molecules in condensed matter. Their structures play an important role in many physical properties of crystals such as thermal conductivity. The two kinds of atoms A and B in graphene unit cells (**Figure 2.2b**) give rise to 6 phonon branches. The atoms can either swing in-phase or anti-phase, which are termed as acoustic (A) and optical (O) phonons respectively. The direction of vibrations can be in-plane (i) and out-of-plane (o). The vibrations can be along the direction of a carbon-carbon bond, called longitudinal (L), or perpendicularly to the bond, named transverse (T). Four out of 6 phonon types are in-plane, and the remaining two are out-of-plane. Thus, SLG contains 6 phonon branches, namely iLO, iTO, oTO, iLA, iTA, and oTA (**Figure 3.4**).[63]

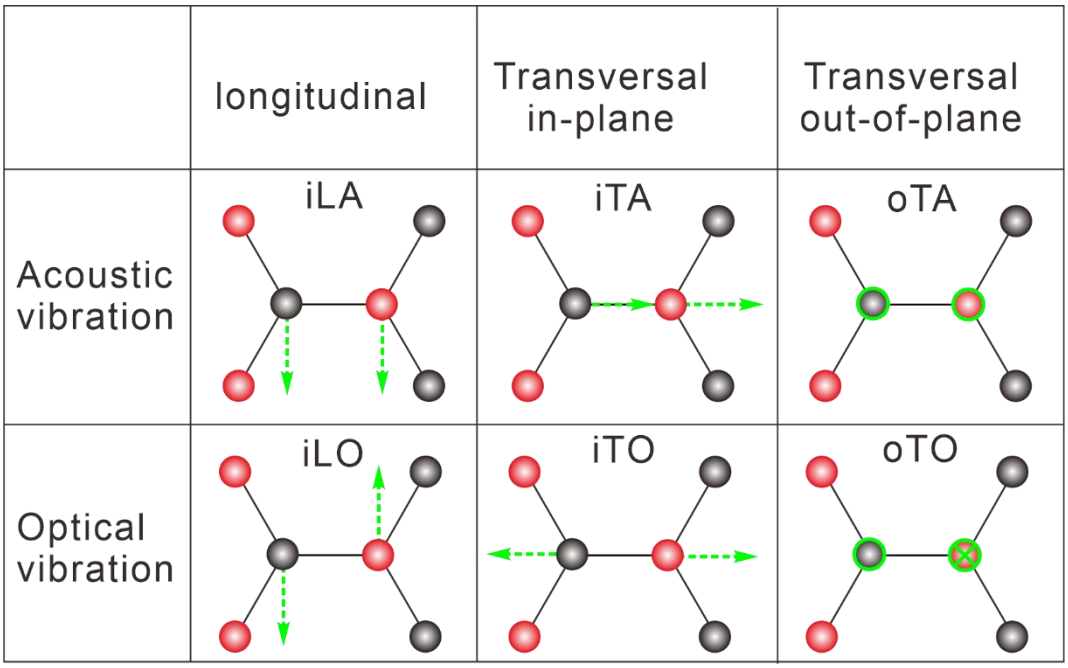

Figure 3.4: Representation of the 6 phonon branches in SLG. Only optical vibration modes cause polarizability changes and therefore being Raman active. The green arrows indicate the vibrational direction of carbon atoms.

The phonons define graphene Raman spectra. Here let's briefly recall the abovementioned Raman scattering process. The incident photon can excite an electron-hole pair, which can be then scattered by emitting a phonon through an electron-phonon interaction. In this process, the excited electron loses part of its energy. Electron and hole can subsequently recombine emitting a photon with smaller energy to compare with the incident one. So Raman scattering is associated with phonon emissions. I will describe in the following the 6 phonon branches in SLG. Not all the phonon branches are Raman-active. As it was introduced in **Section 2.3**, only if a vibration changes the overall polarizability of a molecule, the phonon branch is Raman-active. As shown in **Figure 3.4**, only optical phonon branches vary molecular polarizability, therefore being Raman-active. The following sketch shows the Raman scattering process of different optical phonons of SLG associated with its electronic band structure (**Figure 3.5**).

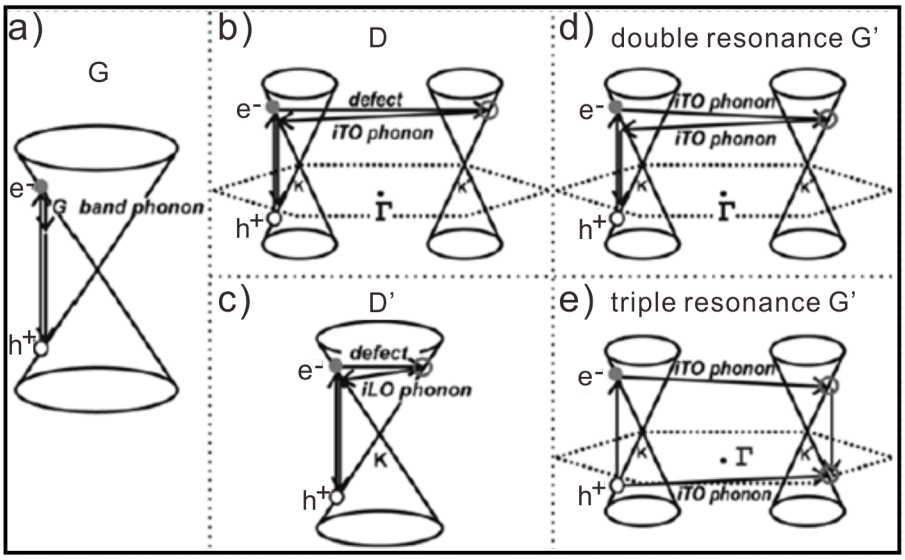

Figure 3.5: Sketch of the phonon modes and electronic scattering mechanisms in SLG: a) G peak: first-order process. b) D peak (intervalley process) and c) D' peak (intravalley process): one-phonon second-order double resonance (DR) process, the scattering by defects is an elastic scattering process. 2D (or G') peak: two-phonon second-order resonance processes, include d) the DR process, and e) the triple resonance (TR) process. (Adopted from Ref.[63])

Such Raman scattering processes yield 4 prominent peaks on an SLG spectrum, named as G peak (~ 1582 cm^{-1}), 2D peak (also called as G', ~ 2700 cm^{-1}), and another two defect-related peaks, D (~ 1350 cm^{-1}) and D' peak (~ 1620 cm^{-1}) (**Figure 3.6**). The detailed explanation about the origin of these 4 peaks was documented by *Malard et al*,[63] and will be simply restated in the next few paragraphs.

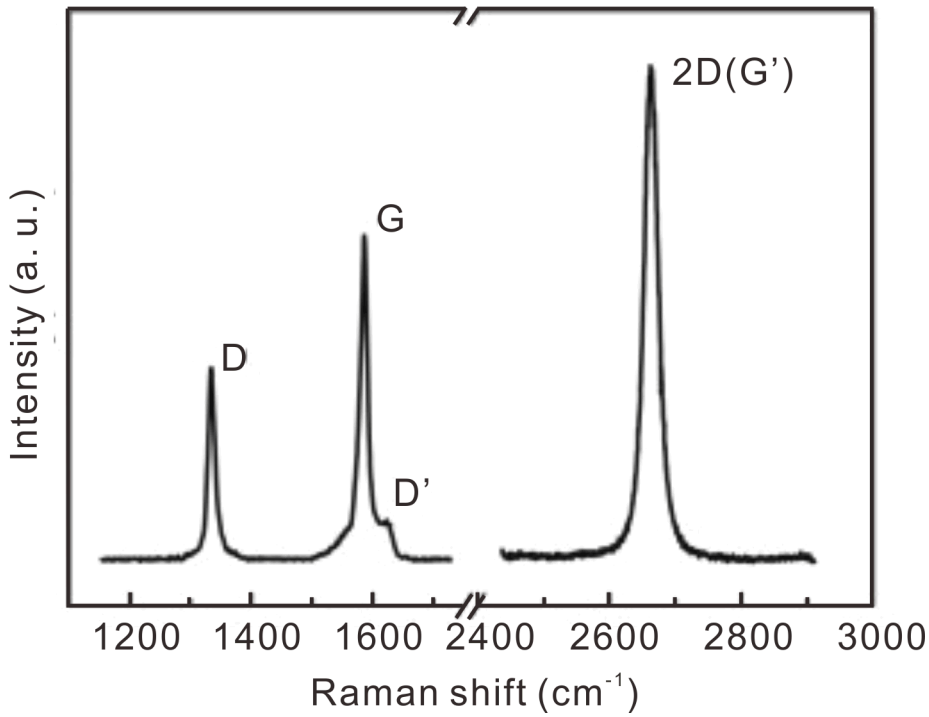

Figure 3.6: Raman spectrum of an SLG edge shows the main Raman features, the D, D', G, and 2D (G') peaks taken with a laser excitation energy of 2.41 eV. (Adopted from Ref.[63]) The graphene edges can be seen as defects, which enhance the D and D' peaks.[77]

The G peak originates from the stretching and bending of the carbon-carbon bonds in the plane (**Figure 3.7a**). It is a first-order Raman band excited directly by incident laser photons near the Γ point in the center of the first Brillouin zone. The iTO and iLO phonons are doubly degenerate at this point. The order of the Raman process is determined by the number of inelastic scattering events of a photo-excited electron. For example, the "first-order Raman" means that a photon-excited electron is scattered only one time by emitting one phonon through the electron-phonon interaction in the Raman process. The physical process is shown in **Figure 3.7b**. When a laser focuses on the SLG, the incident photon excites an electron from ground state s_0 to the first excited state s_1, generating an electron-hole pair in this process. Such a process is called the resonance Raman. Note that this is different from the introduction in **Section 2.3 (Figure 2.6)**, where I mentioned photons excite electrons to a virtual energy state in the Raman process. The laser photons of Raman instruments can induce the electron transition from the ground state s_0 to the first excited state s_1 in graphene due to its zero-band gap. Electrons in a real excited state live longer to compare with a virtual state, which increases the probability of being scattered on a phonon mode. Thus, resonance Raman can enhance the Raman signal giving better spectra quality. Back to the G peak Raman process, the electron in SLG absorbs photon energy and jumps directly to the excited state s_1. Then the phonon near the Γ point scatters the electron to a virtual state s'. After that, the electron recombines with the hole by emitting a photon with less energy than the incident one.

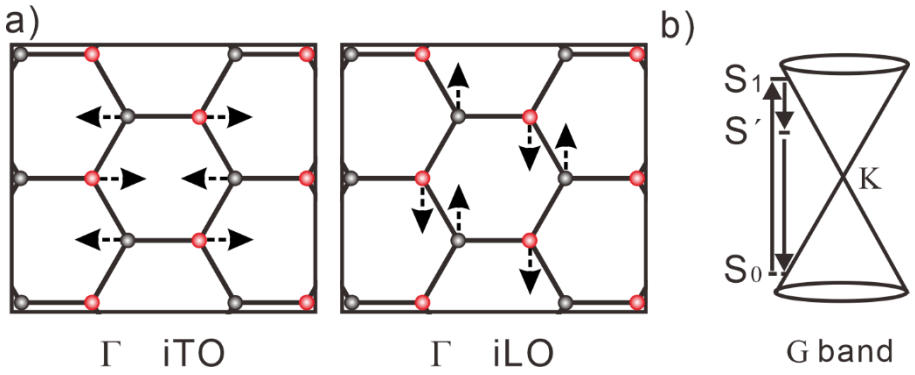

Figure 3.7: a) Two Raman-active phonon modes degenerated at Γ point corresponding to graphene G peak. b) The first-order resonant Raman process of G peak: an electron is excited from ground state s_0 to excited state s_1 by absorption of energy from the incident photon. The electron is scattered to a virtual energy state s' through the electron-phonon interaction, and then the electron further decays back to the ground state s_0. (Adapted from Ref.[81])

The D peak is induced by disorder or defects in SLG, and the 2D peak is the overtone of the D peak. Both peaks are a second-order resonance mode involving the phonon iTO. Here the term "second-order" indicates the photo-excited electron is scattered two times either elastically by a defect or inelastically by emitting a phonon during the Raman process. The electron in the D peak process is first elastically scattered by a crystal defect from K to K'. Then it is inelastically scattered back to the K by emitting an iTO phonon. The electron combines with a hole and emits a lower energy photon. This comes from the breathing modes of six-atom rings (**Figure 3.8a**). Due to the momentum conservation constrain in this process, the D peak requires a defect to activate the elastic scattering as the defect breaks the symmetry of the SLG lattice. The D peak involves both electronic states around the K and K' points. Therefore, this process is called an inter-valley mechanism. Because a high-energy incident photon can excite an electron to a high electronic state (**Figure 3.8b**), the electron will require larger momentum to travel from K to K' than the one excited by a low-energy one. As a consequence, the different energies of the incident photons change the frequency of the phonons involved in this process for momentum conservation. Thus, the D peak position is sensitive to the incident energy and shows a linear dispersion.[82] The same is true for the 2D peak. The 2D peak process is similar to the D peak, *e.g.,* it is also an inter-valley process. The only difference is that the electron in 2D is inelastically scattered from K to K' by emitting an iTO phonon rather than a defect. Since the energy and momentum must be conserved, the electron has to be again inelastically scattered back by emitting another iTO phonon before it recombines with the hole. As two iTO phonons are involved, the 2D peak Raman shift is double that of the D peak. On the other hand, the 2D process is also known as a double resonance (DR) one. Because in 2D process, a photon excites an electron to a real excited state near K point, and the electron is inelastically scattered to another real state near K' point in graphene. Both processes

are in resonance. Actually, a hole may be also scattered from K to K' in this process. In this case, the electron-hole recombination is in resonance states near K' as well, which is known as a triple resonance (TR) process. The 2D peak of SLG is more intense than its G peak, possibly due to the unique TR process in the 2D process.

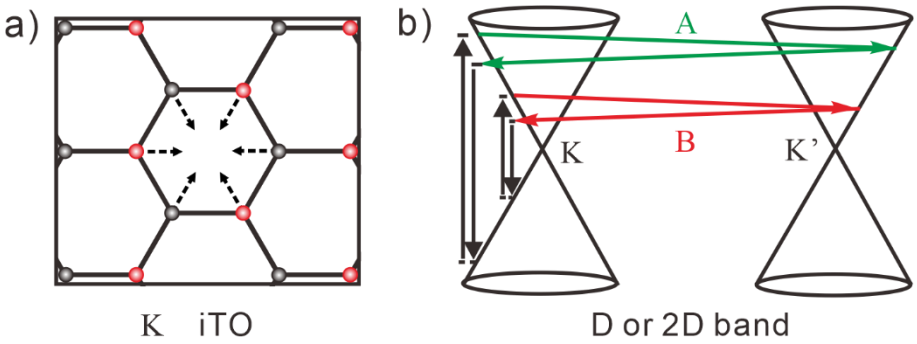

Figure 3.8: a) Breathing phonon modes at K point for D and 2D peaks in SLG. b) Raman scattering of a 2D peak for different incident energies (A > B). (Adapted from Ref.[81])

The D' peak at around 1620 cm^{-1} also requires a defect to be active, but the process is intra-valley with only one iLO phonon being involved.

Raman spectroscopy is extensively used to research graphene, *e.g.*, to determine the number of graphene layers, the density of defects, and more importantly, to detect the doping and strain in graphene.[77, 83] Both doping and strain effects are related to the tunability of graphene's electronic properties.[44-46] The unique phonon, electronic band structure, and their interactions determine the main peaks of graphene to be very sensitive to doping and strain variations. In the following, the doping and strain effects on graphene spectra will be discussed.

3.2.2 The Doping Effects on Graphene Raman Peaks

Doping is a practical approach to modify and control the electrical properties of semiconductors. The doping methods include heteroatom doping, chemical modification, electrostatic field tuning and interfacial charge transfer by contacting semiconductors with other materials, and so forth.[46] In the following, the term "doping" always means "charge-doping" induced by charge transfer between graphene and surroundings, unless specified. SLG is very sensitive to carrier concentration changes because of its linear electronic dispersion (**Figure 3.9**). The conduction band and valence band are in contact with each other at the K (or Dirac) point. The zero density of states at the Dirac point renders graphene high sensitivity to doping, as the Fermi level (E_F) of graphene extremely depends on the carrier concentrations. For undoped SLG, E_F locates at the K point. E_F can be tuned up or down by *n*- or *p*-doping respectively.

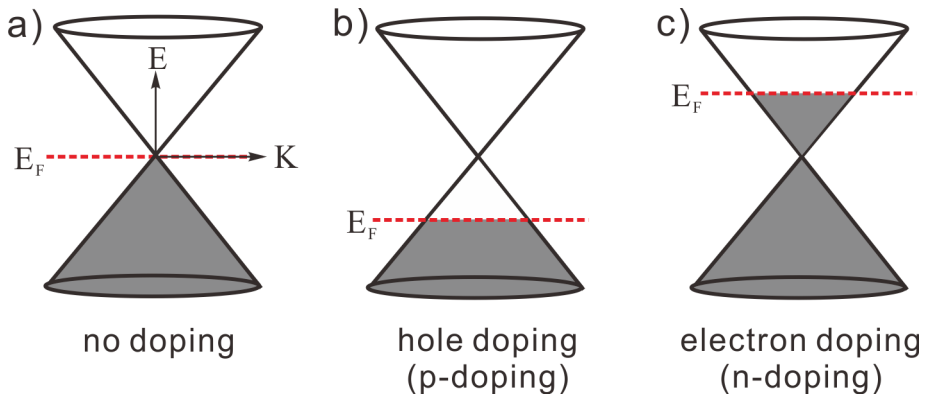

Figure 3.9: Sketch of the band structure of SLG with a) no doping, b) *p*-doping and c) *n*-doping. E_F is the Fermi level. (Adapted from Ref.[81])

Casiraghi et al. have studied more than 40 exfoliated SLGs by Raman spectroscopy.[84] They found that even the SLGs prepared in the same way exhibited large variations in their Raman peaks. For instance, the G and 2D peaks show significant changes in position from different samples and even from different spots of one sample (**Figure 3.10a, b**). Both the G peak full width at half maximum (FWHM) and the integrated intensity ratio (peak area) of 2D to G (I(2D)/I(G)) decrease with the G peak positions (ω(G)) (**Figure 3.10c, d**). All these changes were assigned to variable doping induced by charge inhomogeneity. The excess charges may be due to substrate, adsorbates.

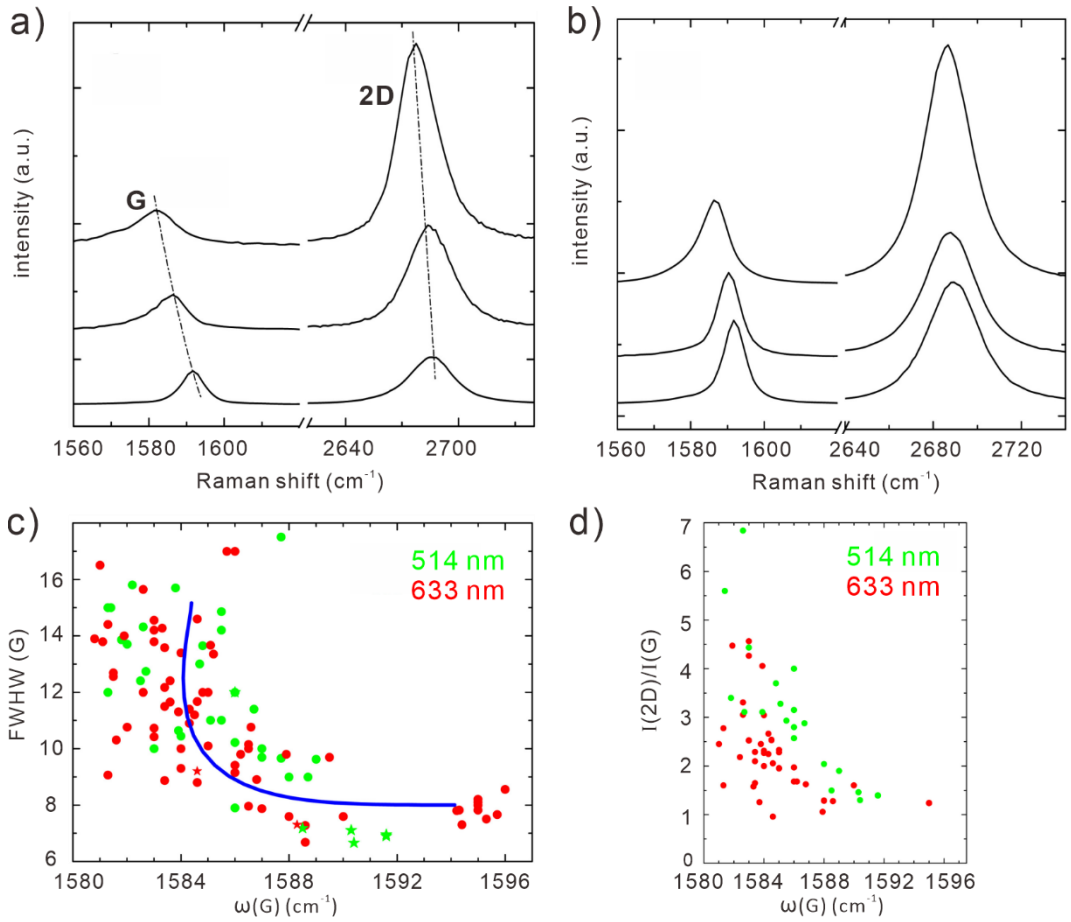

Figure 3.10: Raman spectra of variably doped SLGs. a) Raman spectra of three different SLGs. b) Spectra in three different points of one same SLG. c) G peak FWHM(G) and position ω(G) at 514 nm and 633 nm. The solid lines are the theoretical calculations for doped graphene at 300 K.[85] d) I(2D)/I(G) as a function of ω(G) (Adapted from Ref.[84]).

The doping influence on graphene Raman peaks was further comprehensively studied later by *Das et al.*[86] SLGs were deposited on Si covered with 300 nm of SiO_2 with the method of mechanical exfoliation. A top-gated voltage was applied to control the doping levels of SLG from 0 up to 5 x 10^{13} e^-/cm^2. The Raman spectra of pristine and gated samples were then measured with 514.5 nm (2.41 eV) excitation. They found that the G and 2D peaks exhibited a strong dependence on doping in terms of peak positions, FWHM, and integrated intensity. Both *p*- and *n*-doping upshift the G peak position (**Figure 3.11a**) and broaden its FWHM (**Figure 3.11b**). However, the 2D peak position shows different dependencies for *p*- and *n*-doping. The 2D peak always upshifts with increasing *p*-doping. While for *n*-doping, the 2D peak position shows initially a slight upshift for a relatively low electron concentration range (< 2 x 10^{13} e^-/cm^2), which is followed by a significant downshift for higher doping levels (**Figure 3.11c**). The different dependencies of 2D and G on doping lead to a specific correlation between them, which will be shown together with the strain effect in the next section. **Figure 3.11d** shows that the integrated intensity ratio I(2D)/I(G) decreases as the doping level increases. The

following paragraphs will explain why 2D and G Raman peaks behave differently with *p*- and *n*-doping.

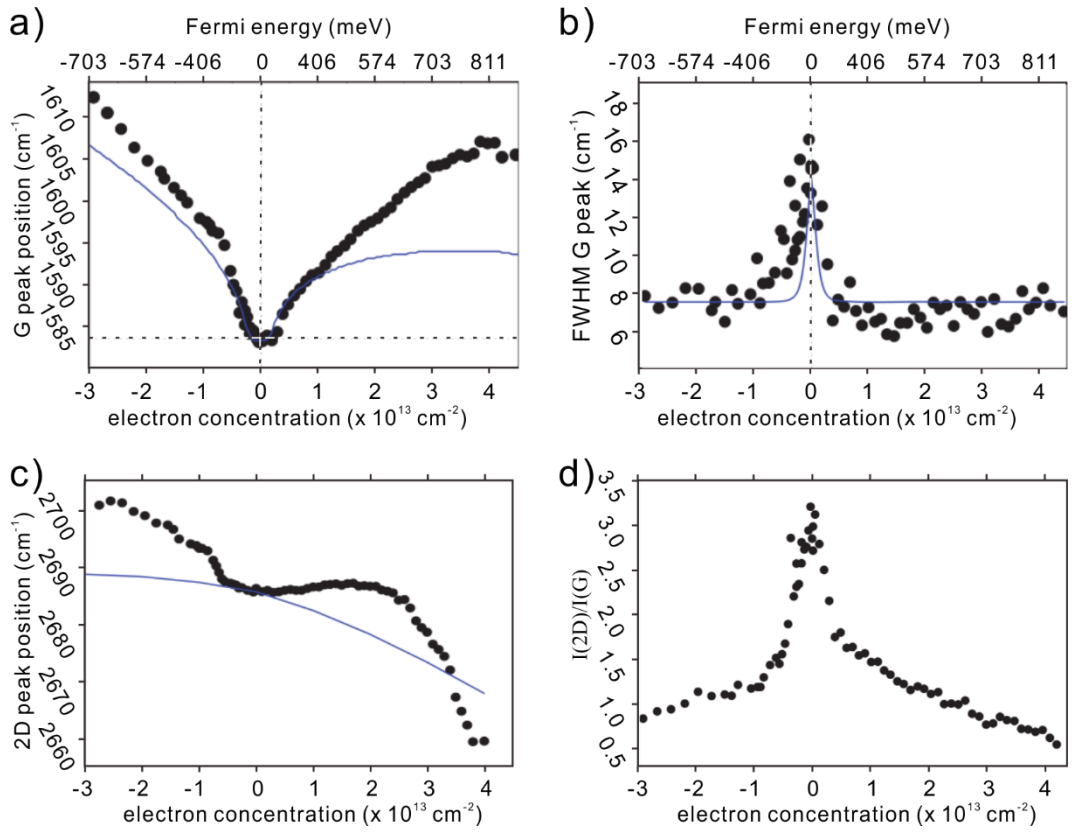

Figure 3.11: Raman SLG peak properties as a function of electron (*n*-) and hole (*p*-) doping: a) G peak positions. b) G peak FWHMs. c) 2D peak positions. d) Intensity ratios of I(2D)/I(G). The solid lines are the theoretical calculations. (Adapted from Ref.[86])

The phonons doubly degenerated at the Γ point of the first Brillouin zone give rise to the G peak (**Figure 3.7**). Theoretical calculations revealed that a Kohn anomaly exists near the Γ point.[87] The Kohn anomaly is the softening of a phonon due to electron-phonon coupling, where the phonon energy is reduced by decaying into electron-hole pairs. Both electron and hole doping in graphene shift the Fermi level out of the Dirac point (**Figure 3.9**) and suppress the interaction of electrons and phonons by restraining the generation of electron-hole pairs (**Figure 3.12**).[81] This causes the displacement of the Kohn anomaly thus stiffening of the G peak (increasing phonon energy). Besides, the electron (hole) doping increases (decreases) the lattice constant, giving rise to a softening (stiffening) of the G peak as well. These two effects together determine the G peak position resulting in the asymmetric dependence of the G peak position on the electron (hole) doping changes (**Figure 3.11a**). Another Kohn anomaly presents at the K point of the first Brillouin zone that is related to phonons of 2D peak.[87] However, the phonons involved in 2D peak are far from the K point where the Kohn anomaly dominates.[70] The contribution from the Kohn anomaly is negligible, only the lattice constant effect plays a role in the

determination of 2D peak position, similar to the case for G peak. As a consequence, 2D peak position decreases (increases) as the electron (hole) concentration increases (Figure 3.11c). On the other hand, the Fermi level shift blocks the decay pathway for phonons into electron-hole pairs due to the Pauli exclusion principle (Figure 3.12). And this results in suppressing the electron-phonon interaction and consequently prolonging the phonon lifetime. Thus, doping narrows G peak width according to the energy-time uncertainty principle. In terms of the intensity changes of both peaks (Figure 3.11d), it was reported 2D peak is more sensitive to the electron-phonon scattering rate than G peak. Because 2D process is a resonant model including two phonons.[88] G peak intensity is insensitive to doping thus can be used for the normalization for other peaks.

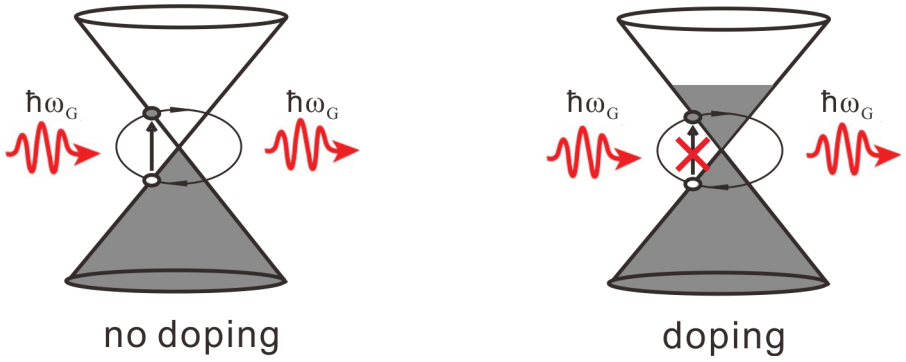

Figure 3.12: Sketch of Fermi level shift inhibiting the decay of G band phonons into electron-hole pairs due to doping. (Adapted from Ref.[81])

3.2.3 The Strain Effects on Graphene Raman Peaks

Mechanical strain is another effect that influences the Raman peaks of graphene. Applying strains on graphene changes the C-C bond lengths and distorts its unit cell, this consequently changes its phonon frequencies and the linear dispersion of the electronic band structure. Typically, two types of strain are discussed in the experimental literature, namely uniaxial strain and biaxial strain. Uniaxial strain changes the graphene unit cell along a specific direction, while biaxial strain uniformly stretches or contracts the unit cell. Both kinds of strain cause frequency changes of phonons thus Raman peak positions. However, G peak originates from two phonon modes degenerated at Γ point, and a large uniaxial strain breaks the symmetry between the two phonon modes. As a result, the G peak becomes split into two sub-peaks under large uniaxial strains. In contrast, the biaxial strain does not break the symmetry and the G peak does not split.[89, 90]

The uniaxial strain effect on graphene Raman spectra has been experimentally investigated with the method of bending a graphene-polymer substrate at ambient conditions by *Mohiuddin et al*.[89] The uniaxial tensile strain causes the downshifting of both G and 2D peak positions with the increasing amount

of tensile strain (Figure 3.13a). As just mentioned, the uniaxial strain breaks the symmetry of the honeycomb lattice of graphene, the G peak splits into G^+ and G^-, while the 2D peak displays no splitting for strain range less than ~ 1.2%.

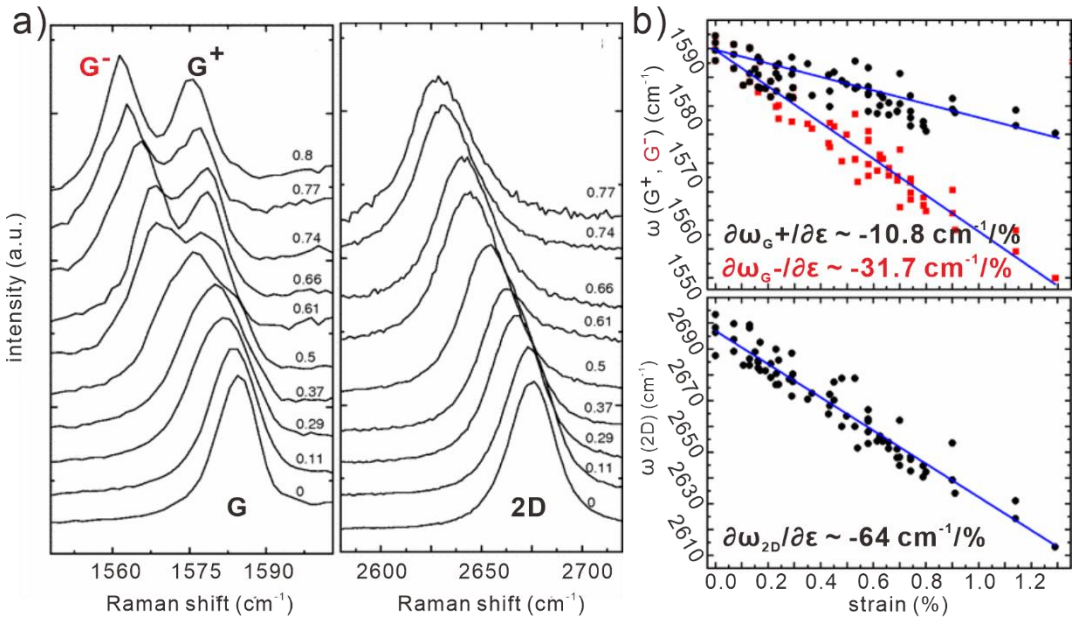

Figure 3.13: a) Raman spectra of G and 2D peaks as a function of uniaxial tensile strain. b) Positions of the G^+, G^-, and 2D peaks as a function of applied uniaxial strain. The lines are linear fits to the data. The slopes of the fitting lines are also indicated (Adapted from Ref.[89])

Similar studies of uniaxial strain on graphene Raman peaks were reported by others.[91, 92] Both G and 2D peak positions exhibit linear dependences on uniaxial strain variations albeit with different slopes. Hence, 2D peak positions depend linearly on G peak positions (ω(2D)/ ω(G)) with a slope depending on the strain direction. When the uniaxial strain is along the zigzag direction (Figure 3.14a), $\omega(2D)/\omega(G^+) = 2.00$, $\omega(2D)/\omega(G^-) = 2.05$. For strain along the arm-chair direction, the $\omega(2D)/\omega(G^+)$ is 3.00 and $\omega(2D)/\omega(G^-) = 1.89$.[92] However, when the overall stain is less than ~ 0.4 %, the splitting G peak is insufficient to resolve the G^+ and G^- modes. Thus, the ω(2D)/ω(G) for the zigzag and arm-chair direction can be calculated as an average of $\omega(2D)/\omega(G^+)$ and $\omega(2D)/\omega(G^-)$, approximately equals to 2.02 and 2.44 respectively. Since the native strain in SLGs on a substrate can be in any direction between the zigzag and arm-chair axes, the slope of ω(2D)/ω(G) in this case is expected to be averaged as 2.2 $\pm$ 0.2. This expectation was further experimentally verified by a Raman study on native strains in graphene by *Lee et al*.[93] Their results suggested the native strains in graphene induced by a rough substrate surface dominate the ω(2D)/ω(G) ratio exactly following the slope of 2.2 (Figure 3.14b). And the same slope of ω(2D)/ω(G) on biaxial strain was found using the method of graphene bubbles.[94]

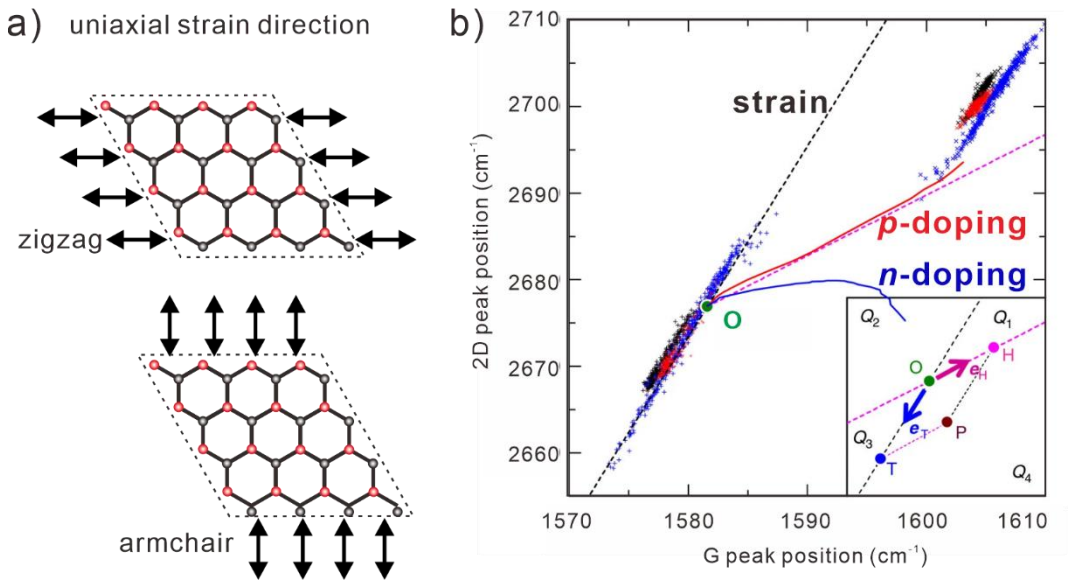

Figure 3.14: a) Sketch of the uniaxial strain direction along the zigzag (top) and the armchair (bottom) axes. b) The ω(2D)/ω(G) shifts induced by either doping or strain effect. The data were obtained from Raman mapping of three graphene samples (colored in red, blue, and black) before (+) and after (×) thermal annealing at 400 °C. After the thermal annealing, the data points shift to the domain of larger Raman shifts. The green dot (O) obtained from a freestanding graphene sample is expected to be undoped and unstrained. The red and blue solid lines represent ω(2D)/ω(G) shifts for *p*- and *n*-doped graphene, respectively.[86, 95] The magenta dashed line is an average of experimental (ω_G, ω_{2D}) for strain-free but p-doped graphene. The black dashed line with a slope of 2.2 shows the expected ω(2D)/ω(G) shifts for undoped but strained graphene. Inset: decomposition of the effects of *p*-doping and strain using a vector model. Any given (ω_G, ω_{2D}), OP, can be decomposed into OH along the "strain-free" unit vector e_H for *p*-doping, and OT along the "charge-neutral" unit vector e_T for tensile strain ($-e_T$ for compressive strain), respectively. e_H and e_T divide the ω_G-ω_{2D} space into the 4 quadrants (Q_1 –Q_4). (Adapted from Ref.[93])

To summarize this section, both strain and doping cause significant changes of graphene spectra, especially the peak position of G and 2D become significantly affected. Raman spectroscopy allows unraveling the strain and doping effects on peak position shifts. It has been revealed, that for a small magnitude of strain, *p*- and *n*-doping shift ω(2D)/ω(G) nearly linearly with a slope of ~ 2.2, 0.55, and 0.2, respectively.[93, 96] In other words, through analyzing the G and 2D peak position changes, one can calculate the carrier concentrations and strains in graphene to monitor the charge carrier transfer and strain variations. Using this, the influences of substrates and confined liquids on graphene properties have been widely studied. The following section will present an overview of the related studies.

3.3 Interplays between Confined Water and Graphene/Substrate

3.3.1 Graphene Doping Changes by Adsorbed Water Molecules

As introduced in Section 3.1 (Figure 3.3), the computer simulations suggested that water molecules adsorb onto mica with their dipole moments pointing down forming a densely packed monolayer. The monolayer structure is defined by the hydrogen bonding between mica O- and water H- atoms. Therefore, one might expect that water molecules form a similarly high-ordered monolayer at an interface between mica and graphene. The effects of the high-ordered water layers adsorbed on graphene onto its electronic properties have been explored both theoretically and experimentally.[18, 21, 22, 40, 42, 97] *Shim et al*. showed that SLGs deposited on a freshly cleaved mica surface were strongly *p*-doped with hole densities of (9 ± 2) x 10^{12} cm^{-2} with the aid of both Raman spectroscopy and scanning Kelvin probe microscopy. And a thin water layer of ~ 4 Å confined within the graphene-mica slit pore at high RH removed the most hole doping (Figure 3.15).[18] The graphene doping mechanism was attributed to the charge transfer from mica to graphene due to a larger electron affinity of mica surface compared with that of graphene. However, the reason for why the confined water rendered graphene uncharged was not clear. The author proposed two possible mechanisms: either the electron tunneling blockade due to a larger separation between graphene and mica by the existence of the confined water layer, or blocking of charge transfer from graphene to mica by the high-ordered water layers because the dipole-oriented water layer on mica could vary the electrostatic potential at the mica surface.[98] Thus the charge transfer direction and degree may depend on the dipole moment of the adsorbed water layer.

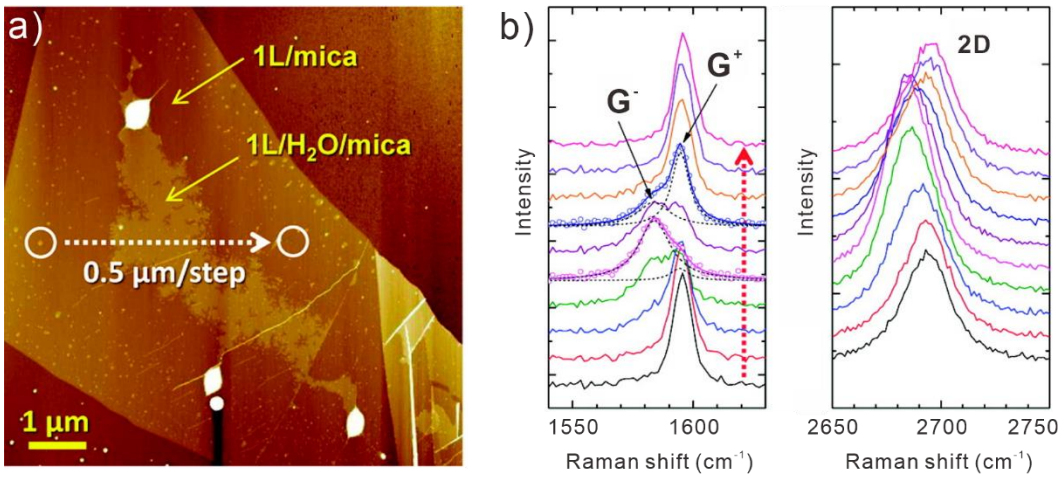

Figure 3.15: a) SFM height image of graphene on mica obtained under tapping mode. b) A series of Raman spectra of the graphene acquired along the dashed arrow in a) (from bottom to top as indicated by the red arrow). (Adapted from Ref.[18])

A similar effect of confined water layers on graphene has been also observed by other groups.[42, 97, 99] For example, *Lee et al.* showed thermal annealing of a graphene-silica sample in air-induced *p*-doping of graphene due to adsorption of hole-doping oxygen species from the ambient air. Water intercalated into the graphene-silica interface from graphene edges when the sample was submerged in water. And the intercalated water drove out the oxygen species and undoped graphene.[42] *Goncher et al.* studied SLGs exfoliated onto mica using UHV-STM for high-resolution images of graphene, and scanning tunneling spectroscopy for characterizations of variations in the electronic local density of states of graphene.[99] They observed that graphene areas on top of water islands were not doped, while graphene was *n*-doped above K^+ ions on mica. The different doping types in graphene were explained by direct contact with the local charge domains on the mica surface. *Ochedowski et al*. reported a transition from *p*-doping to *n*-doping of exfoliated graphene on mica upon annealing.[21] The *p*-doping of graphene in ambient was ascribed to the moist oxygen or airborne contaminations functioned as dopant species.[39, 100] Yet, the mechanism for the transition of doping type with water adlayer has several possible reasons, *e.g.*, removing the adsorbates during annealing; charge transfer from mica due to work function changes upon dehydration; increasing defect densities on graphene at high temperatures. In addition to these possible mechanisms, *Bampoulis et al*. argued that the doping type in graphene correlates to the number of water layers in the graphene-mica slit pore. As introduced in **Section 3.1**, *Bampoulis* believed two water adlayers existed in the graphene-mica slit pore at ambient conditions.[22] The dipole orientation of the first 2D-ice water layer *p*-dopes graphene, while the less-ordered second layer has almost zero effect on graphene electronic properties. However, he attributed the doping changes in graphene to the charge transfer directly from the confined water layers rather than the mica substrate.

The abovementioned studies discussed the effects of confined water layers on graphene doping albeit the mechanisms were disputed. Thus, further investigations on this topic are required. Moreover, the possible influence of water adsorbed on graphene top surface is also worthy of study. It was reported by *Schedin et al.* that graphene could be used as gas sensors with sensitivity high enough to detect individual gas molecules, including water.[101] They prepared a graphene Hall bar and measured it in different gas vapors. By monitoring the resistance changes, the doping variation in graphene could be detected when exposing the sample to small concentrations (ppm) of gas molecules. The *p*-doping of graphene upon exposure to water molecules was observed. The authors attributed this to chemical doping, where water molecules adsorbed on graphene top surface functioned as hole dopants. However, they could not exclude the possible influence of the substrate on doping. There has been reported that the substrates play a critical role in the absorbates-induced doping of graphene.[39] The substrates might influence the magnitude and direction of charge transfer at the graphene–substrate interface. Thus, it is also important to clarify whether water molecules adsorbed on graphene

top surface have the same influences on graphene doping compared with those intercalated at the graphene-substrate interface, and whether the former or the latter dominates the changes in graphene doping.

3.3.2 Graphene Strain Changes upon Interface Hydration

Graphene can be easily deformed by substrates due to its high flexibility. And graphenes deposited on different substrates are reported to be variously strained.[102, 103] Investigation of how strain changes in graphene upon water intercalation is of great importance, as the dynamics of strain changes in graphene reflect the interfacial frictions. The lubricating properties of water at interfaces require deeper insight, since the questions such as how interfaces influence the water lubricating properties are still disputed.[104-106] However, contrasting to the rich studies on how graphene doping changes with confined water layers, there are only a few studies on how the graphene strain changes upon hydration. Water layers at the graphene-substrate interface were reported to result in strain relaxation in graphene.[97] However, the dynamics of strain relaxation upon hydration were not properly followed. Other studies mostly focus on how the interfacial water alters the friction between graphene and SFM tip using contact mode.[35, 61] Thus, it is beneficial to study the time-evolution of strain in graphene upon hydration, to investigate the role of the intercalated water layer on interface lubrication.

The clean graphene-mica system provides the opportunity to study the water layer influence on doping and strain effects in graphene. In the next chapter, I will introduce the SFM and Raman techniques, and all the home-built setups employed to do experiments for this purpose.

4. Analytical Techniques and Experimental Setups

4.1 Raman Microscope

For the acquisition of a Raman spectrum, a sample is mounted in the sample chamber, and a single wavelength laser light is shone on it. The light is then scattered. Most of the scattered light is Rayleigh, and only a small portion of the scattered light is the Raman one. One needs a monochromator or a special filter to block the Rayleigh scattered light. The Raman scattered light leaving the slit of the monochromator is collected and focused on the surface of a photodetector. In conventional Raman spectroscopies, a photomultiplier tube (PMT) is usually used. The PMT has many 'Dynodes' which multiply the number of photons to record a signal. The PMT amplifies the signal. It can detect single photons and multiply those manifolds depending on the number of Dynodes. **Figure 4.1a** shows the basic components and structure of a conventional Raman spectrometer.[107] In the conventional approach, the laser beam direction and the axis of the collection lens are usually at 90 degrees to each other. The 90-degree geometry is commonly suitable for studies at the macro-level of samples. The obtained spectrum provides average information over a large sample area. This is so even in cases where a sample is heterogeneous at the micro-level. To obtain spectra from micrometer regions of a sample, the 180-degree geometry (also called backscattering mode) is employed, in which the laser beam and the axis of the collection lens are coincident. Nowadays, a modern confocal Raman spectroscopy is widely used with the development of lasers and microscope objectives.[108] The laser is reflected by a dichroic mirror and focused on the sample using an objective. The Rayleigh scattering from the sample is blocked by the dichroic mirror. The remaining Raman signals pass through another objective while only in-focus reflected light can finally reach the detector through a pinhole aperture. The pin-hole is used to cut off the light stemming not from the focal volume (**Figure 4.1b**). In modern equipment, a charge-coupled device (CCD) detector is used, which has less integration time as it can detect multiple wavelengths simultaneously with many photosensitive elements.

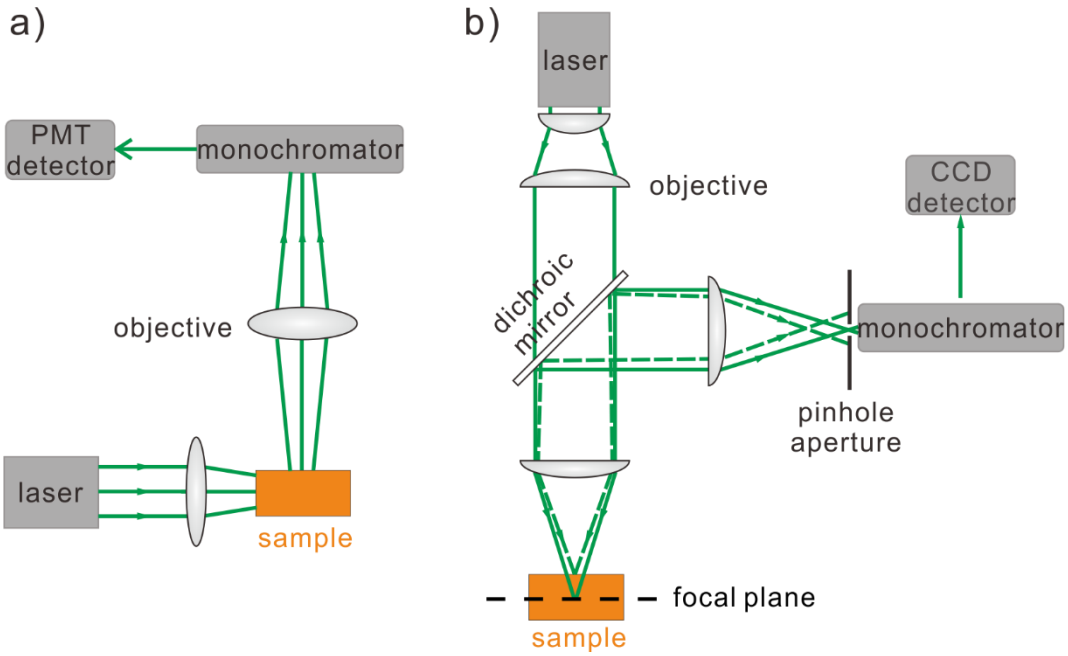

Figure 4.1: Schematic diagram of the principal setup of a) a conventional and b) a confocal Raman spectroscope.

The Raman instrument in our lab is a confocal Raman microscope (XploRa) purchased from Horiba Ltd. It is equipped with 532 nm, 638 nm, and 785 nm high brightness lasers. I used the 532 nm (green) laser in all experiments. The specified software Lab Spec 6 (Horiba Ltd.) is designed for the Raman spectrometer.

4.2 Scanning Force Microscopy

SFM, one of the SPM techniques, utilizes the physical interaction between a tip and a sample to detect the surface morphology and other physical properties of samples. It mainly consists of 4 core components, namely a laser beam, cantilever with a nanoscale sharp tip fixed to its open end, piezo-scanner, and photodiode (**Figure 4.2a**). When a sample is scanned, the tip-sample interaction causes deflection of the cantilever depending on the tip-sample distance. In other words, the deflection of the cantilever is a direct reflection of the tip-sample interaction.[109] The laser beams onto the cantilever backside and reflects the deflection onto a position-sensitive photodiode. In general cases, the *xyz*-scanner (piezo elements) control and coordinate the movement of the sample stage. The *z*-piezo keeps the cantilever deflection constant through a feedback circuit. The movement in the *z*-direction is consistent with the sample surface topography and converted to form the surface topography image. The tip-sample interaction force can be obtained from the spring constant of the cantilever according to Hooke's law.[110] The force includes the attractive van der Waals (vdW) and the Pauli repulsion force due to overlapping electron orbitals. The interaction *versus* distance of the tip-sample can

be described by the Lennard-Jones-potential (Figure 4.2b).[110]

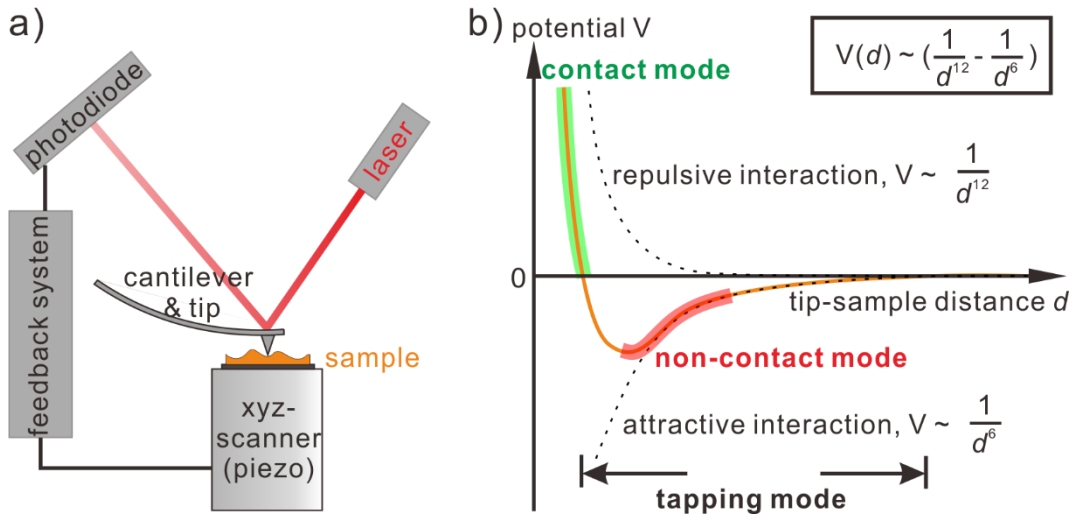

Figure 4.2: a) Schematic diagram of the core components of an SFM. b) The orange solid curve shows the Lennard-Jones-potential, the repulsive and attractive terms are shown as black dashed curves. The portions of the potential dominating the respective SFM modes are highlighted and indicated.

There are usually three typical imaging modes according to the tip-sample interaction (Figure 4.2b): contact mode, non-contact mode, and tapping mode.[111] In contact mode, as its name implies, the tip always "touches" the sample. The tip-sample distance is usually less than 2 Å within the repulsive force. When tip scans along the sample surface, the rough surface tends to change the tip-sample distance thus the cantilever deflection. The feedback circuit keeps the deflection constant to form a topographic image. This mode usually produces stable, high-resolution images but the tip may scratch and damage the sample surface as it is directly in contact with the sample. While in non-contact mode, the cantilever vibrates above the sample surface without any direct contact. The cantilever is oscillated at about its resonant frequency with an amplitude less than 10 nm. When the cantilever moves close to the sample surface, the tip mainly detects vdW attractive forces. The difference in tip-sample surface distance alters the tip-sample forces and thus vibrating the resonance frequency of the tip. The non-contact mode keeps the tip frequency shift (or phase shift) constant by adjusting the tip-surface distance. This mode allows non-destructive collection of the surface image but usually with a lower resolution compared to the contact mode. In terms of the tapping mode, it combines the advantages of both contact and non-contact mode. During scanning, the cantilever is driven with a larger amplitude (normally larger than 10 nm) near the resonance frequency, so that the tip vibrates and intermittently contacts the sample. The amplitude will decrease when the tip approaches the surface until it gently touches it. And it will return to the original value when the tip moves away from the surface. The feedback system continuously adjusts the tip-sample distance to keep

the cantilever amplitude constant, so that the force acting on the sample remains constant. Because the tip is in intermittent contact with the sample, the resolution is almost as good as the contact mode. And the contact time is very short so that the sample damage caused by the shear force almost completely disappears. Tapping mode is suitable for analyzing soft, sticky, brittle samples and samples in liquids. All SFM images presented in this thesis were obtained in the tapping mode.

4.3 Experimental Setups

This section describes setups designed for 4.3.1) Raman measurements on SLGs in controlled gas environments, *i.e.*, in dry nitrogen, humid nitrogen, and organic solvent vapors; and 4.3.2) investigations of strain evolution in SLG and MoS_2 pieces.

4.3.1 Environmental Control Setup

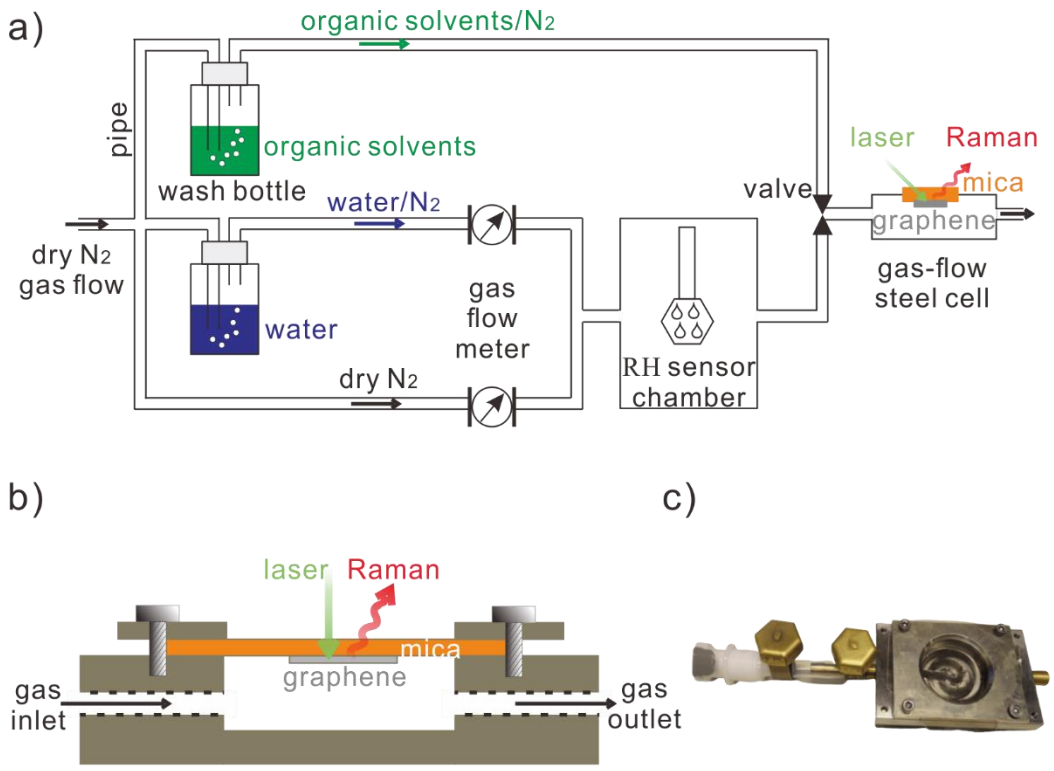

Figure 4.3: Schematic diagram of a) the experimental setup for switching gas flows (dry and humid nitrogen, organic solvents/nitrogen) to graphene samples, and b) the gas-flow steel cell (not to scale) used to seal graphene. c) The photograph of the steel cell.

To achieve sample measurements in well-controlled humidity and gas environments, the environmental control setup was designed (**Figure 4.3a**). Dry nitrogen (Linde group, 99.999%) flowed into the setup and was routed into three

polytetrafluoroethylene pipes (Carl Roth GmbH): one for dry nitrogen, the other two for nitrogen bubbling through deionized water (Protegra CS Systems CEDI Technology >10 M cm) and organic solvents (ethanol (99.99%, (Berkel AHK, 1511U)), acetone (99.9%, ROTISOLV, HPLC) or 2-propanol (99.9%, ROTISOLV, HPLC)) filled gas washing bottles, respectively. Through adjusting the valve, one can control either dry/humid nitrogen or organic solvent vapors flowing out of the outlet. The RH of the nitrogen flowing through the cell was measured with Testo 625 thermo-hygrometer (Testo Inc.). The sensor was placed in a chamber connected to the sample cell. The RH inside the cell was adjusted by controlling the mixing rates of dry and humid nitrogen flows. The Testo instrument calibration fidelity is ± 2.5% as specified by the manufacturer. Provided RH values are the displayed ones. In addition, to prepare initial dry graphene samples, graphenes were exfoliated onto mica in a glove box (LABmaster, M. Braun Inertgas-Systeme GmbH) filled with dry nitrogen. The water concentration inside it is less than 10 ppm. To keep the graphenes dry, a home-built gas-flow steel cell (**Figure 4.3c**) was employed to seal the dry graphenes. Mica with graphenes thereon was fixed onto the steel cell with graphenes facing the inner cell chamber acting as a semi-transparent lid (see the sketch in **Figure 4.3b**). The steel cell was first sealed after sample preparation in the glove box, then connected to the outlet of the gas-controlled setup shown in **Figure 4.3a**. This allowed exposing the dry samples sealed inside the cell to different vapors during Raman measurements.

4.3.2 Four-Point Bending Setup

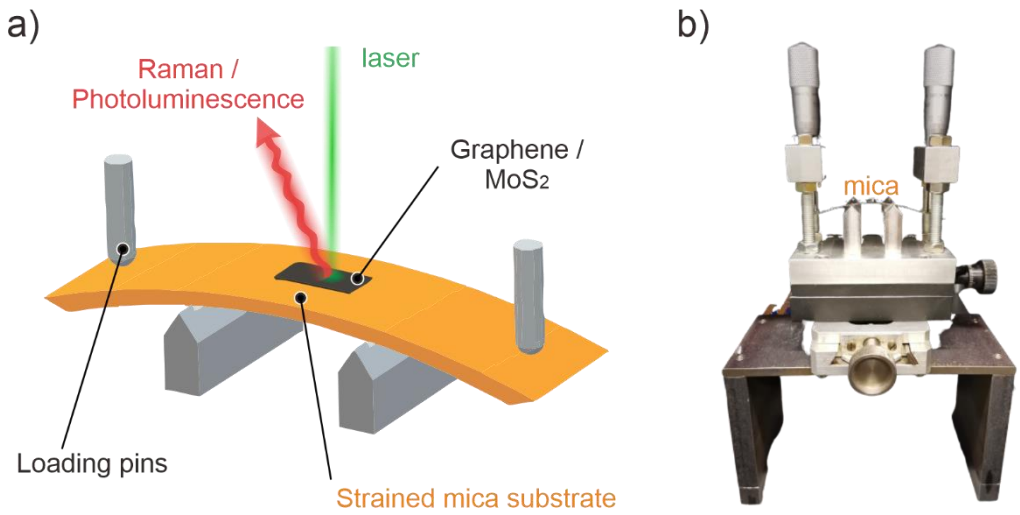

Figure 4.4: a) Scheme (not to scale, adopted from Ref.[112]) and b) photograph of the four-point bending setup.

For investigation of strain relaxation in graphene and MoS_2, mica slabs were cleaved in a glove box with less than 10 ppm water. And graphene and MoS_2 flakes were exfoliated onto the central area of the slabs. Then the samples were sealed in a

plastic box and transferred to another glove box containing the Raman microscope. This glove box was connected to the gas-mixing setup (**Figure 4.3a**) for Raman or PL measurements on the samples at variable gas environments. Mica slabs were mounted to the four-point bending setup with its central part facing the objective of the Raman microscope (see the sketch in **Figure 4.4a**). Single-layer graphene and MoS_2 pieces were optically detected with the microscope of the Raman instrument. The surface of the mica substrate was strained by bending the mica slab in steps through screwing down the loading pins (controlled by micrometer screws in the photograph of **Figure 4.4b**). The loading pins have 0.5 mm precision, which allows the two ends of mica to be screwed down precisely up to 12 mm. The surface strain was estimated for the maximally bent substrates. For smaller bending radii, a linear dependency between the surface strain and extension of the loading pins was assumed. Strains in graphene and MoS_2 flakes were followed with Raman and PL peak position measurements, respectively.

5. Research Design and Major Findings

5.1 Insight into the Wetting of a Graphene-Mica Slit Pore with a Monolayer of Water

5.1.1 Introduction

The properties of nanoconfined liquids are of great interest and importance for both fundamental research and practical technological applications, *e.g.*, understanding of transportations of water through nanoscopic pores is vital for the fabrication of filtration membranes.[9]

Graphene-mica slit pore, as it has been introduced in **Section 1.1**, is a versatile tool for studying liquids confined in it, and especially of water films.[8, 15, 17, 18, 21] Hitherto, SFM studies on water films in the slit pore are productive, yet some disputes remain, *e.g.*, on the number of molecular water layers confined in the slit pore, and on the fluidity of the confined films at ambient conditions.[15, 17, 113] Furthermore, the related SFM studies focused on the structure of the confined water layer. The process of wetting an initially dry slit pore by water molecules remains largely unexplored, and therefore requires further research. On the other hand, to better understand the water layer properties and how it influences the graphene-mica system, other than SFM characterization techniques should be used.

Graphene exhibits strong Raman signals in a spectral range where water and mica do not, and its strain and doping can be quantified *via* Raman spectroscopy (**Section 3.2**). Raman spectroscopy can be done *in situ* on graphene to trace its doping and strain changes with water wetting the slit pore. Hence this part of the work endeavors to gain insight into the wetting process of water in the slit pore by *in situ* SFM and Raman investigations on graphene coatings. I will show that the wetting of the dry graphene-mica slit pores with water was achieved under well-controlled RHs, and characterized by SFM and Raman spectroscopy. The SFM results show that the thickness of the wetting layer is comparable to the size of a single water molecule, which is smaller than the one expected for I_h-ice bilayer of water.[15] And, the Raman results suggest that graphene is in direct contact with the ionic mica surface in dry nitrogen, while a thin water layer wetting the slit pore decouples the graphene from the mica substrate both mechanically and electronically.

5.1.2 Experimental

To keep the mica surface as clean as possible after cleavage, in my work, all

mica sheets (Ratan Mica Exports, grade V1 (optical quality)) were freshly cleaved by an electrically grounded pair of tweezers in a glove box (LABmaster, M. Braun Inertgas-Systeme GmbH) filled with dry nitrogen (Linde group, 99.999%). The tweezers were grounded to remove extra charges potentially induced on graphene flakes during their exfoliation. Thin graphite flakes were then peeled off a piece of freshly cleaved highly oriented pyrolytic graphite (HOPG, grade ZYA, Momentive Performance Inc.) and put onto the mica surface with the same tweezers. The flakes were removed after a few minutes. SLGs which remained occasionally on the mica surface were detected with an optical microscope located inside the glove box.[69] For SFM imaging, the dry samples were sealed in a sample cell of the Cypher-ES SFM instrument (Asylum Research/Oxford Instruments) in the glove box. Then the sample cell was transferred to the instrument and connected to dry nitrogen flow. In this process, the sample was sealed and always kept in dry condition without exposure to ambient. The RH in the cell was controlled by mixing dry nitrogen with the dry nitrogen bubbling through a water-filled gas washing bottle. For Raman measurements, mica was fixed onto the homebuilt gas cell with graphene facing the inner cell chamber such that mica sealed the cell and worked as a semi-transparent lid (**Figure 4.3b**). The gas cell was additionally sealed in a plastic box and transferred to connect with the home-built gas mixing setup (**Figure 4.3a**) for Raman investigations at variable RHs.

The SFM imaging was operated in tapping mode. Silicon cantilevers with typical resonance frequencies of 300 kHz and spring constants of 42 N/m (OMCL-AC160TSG, Olympus Corporation) were used. The SFM images were processed and analyzed with SPIP (Image Metrology A/S) image-processing software.

Raman measurements were performed with 2400 lines/mm grating. The excitation laser was 532 nm with 1.4 mW illumination intensity on the sample surface. The Raman spectroscope was calibrated before and after each day of experiments, using benzonitrile (Sigma-Aldrich, Chromasolv 99.9%) and cyclohexane (Sigma-Aldrich, Chromasolv Plus >99.9%) according to ASTM E1840 standard. Standard peak positions of benzonitrile (1598.9 ± 0.7 cm^{-1}) and cyclohexene (2664.4 ± 0.4 cm^{-1}) were used to correct graphene G and 2D peak positions, respectively. The error of the peak position was calculated as the sum of the ASTM E1840 errors specified above and half of the calibration drift over the day. Fourteen SLG pieces detected in two samples were measured under ~ 2% and ~ 50% RHs. The delay between the onset of humid nitrogen flow and Raman measurements was at least 1 h. For the test of the D' peak reactivation, another 4 SLGs were measured upon repeating drying and humidifying cycles of the slit pore two times. The spectra were processed with the LAB SPEC 6 software. Peaks in the spectra were fitted with Lorentz functions. The peak areas, positions, and FWHM values provided are the values of the fits.

5.1.3 Results

Figure 5.1.1 shows the SFM height images of SLGs under variable RHs. The SLG both exfoliated and imaged in dry nitrogen is atomically flat (Figure 5.1.1a). Water islands penetrate graphene edges upon raising RH to ~ 15% (Figure 5.1.1d). They grow inwards with further increasing RH and form labyrinthine patterns (Figure 5.1.1b). The water islands propagate laterally with time and RH, and grow to a layer of uniform thickness, leading to a flat graphene topography at ~ 40% RH (Figure 5.1.1c). The step height of the islands is about 2.8 Å. Redrying the fully hydrated slit pore upon decreasing RH from 40% to 5% leads to fractal depressions (Figure 5.1.1e). The depth of the fractals is also 2.8 ± 0.3 Å, with the error being the standard deviation. The height information is consistent with the previous results.[17, 23, 24] Phase images were simultaneously acquired with topography images, exhibiting a strong contrast between the graphene area and bare mica surface, but almost no contrast on the graphene area (Figure 5.1.1d, e insets).

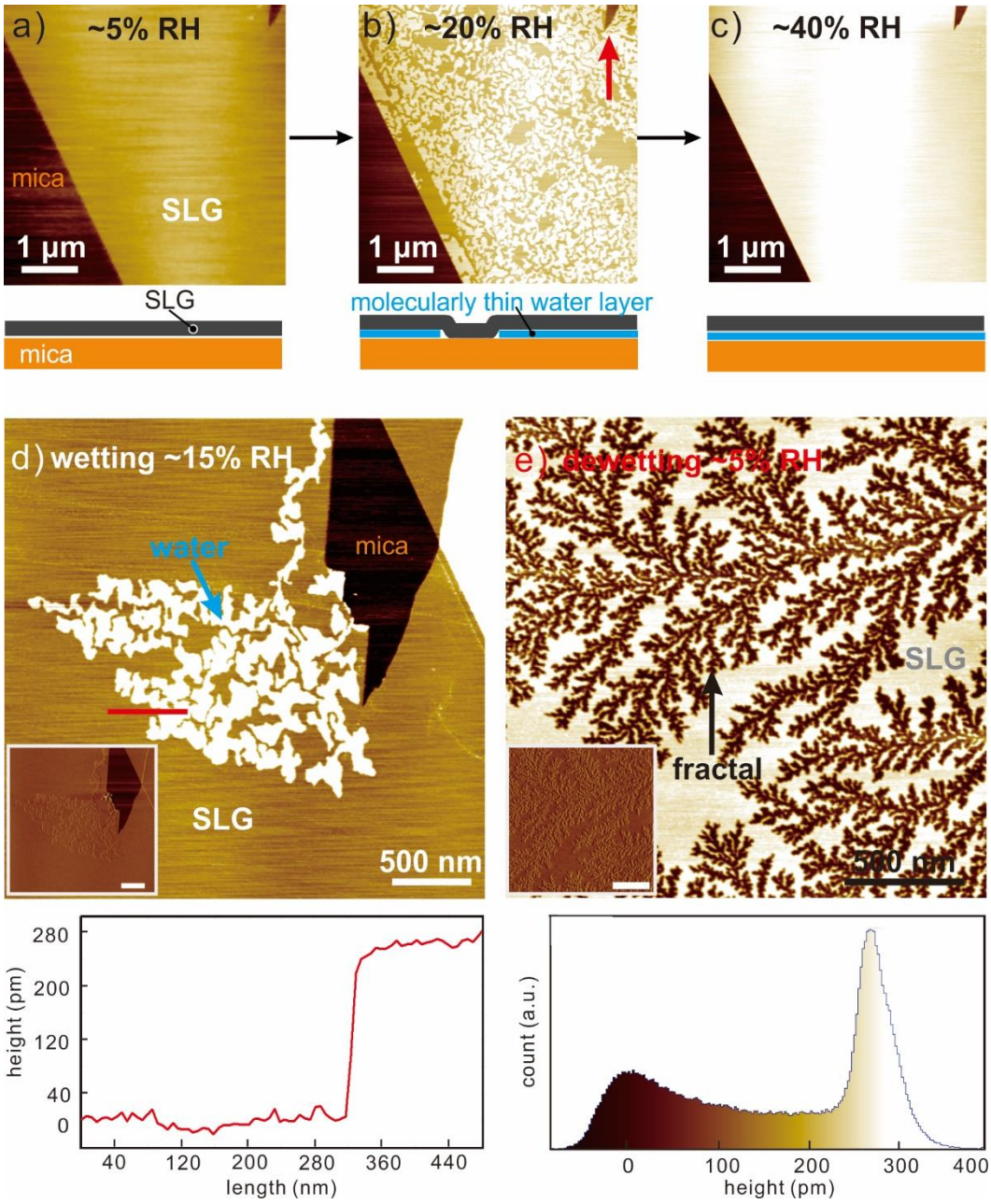

Figure 5.1.1: SFM height images of a graphene-mica sample acquired sequentially at a) ~ 5%, b) 20%, and c) 40% RH. The sketches below show the wetting process. The water molecules started intercalating into the dry graphene-mica slit pore from the graphene edge as indicated with a red arrow in b) at ~ 15% RH. d) The beginning of the wetting process is shown in a zoom into the edge in b). The height profile over the red line is shown below. It reveals that the height of water islands is comparable to the size of a water molecule (2.8 Å). e) Dewetting the hydrated graphene upon decreasing RH caused growth of fractal depressions. The histogram of height distribution on the graphene surface indicates that the fractal depth is also 2.8 ± 0.3 Å. The insets in d) and e) show the phase images taken simultaneously with the height ones.

Figure 5.1.2a displays typical Raman spectra of a SLG acquired on the same

area at ~ 2% and ~ 50% RH. From dry to humid environment, the Raman spectra reveal significant changes in G, 2D, D, and D' peaks, which I will explain in detail in the following.

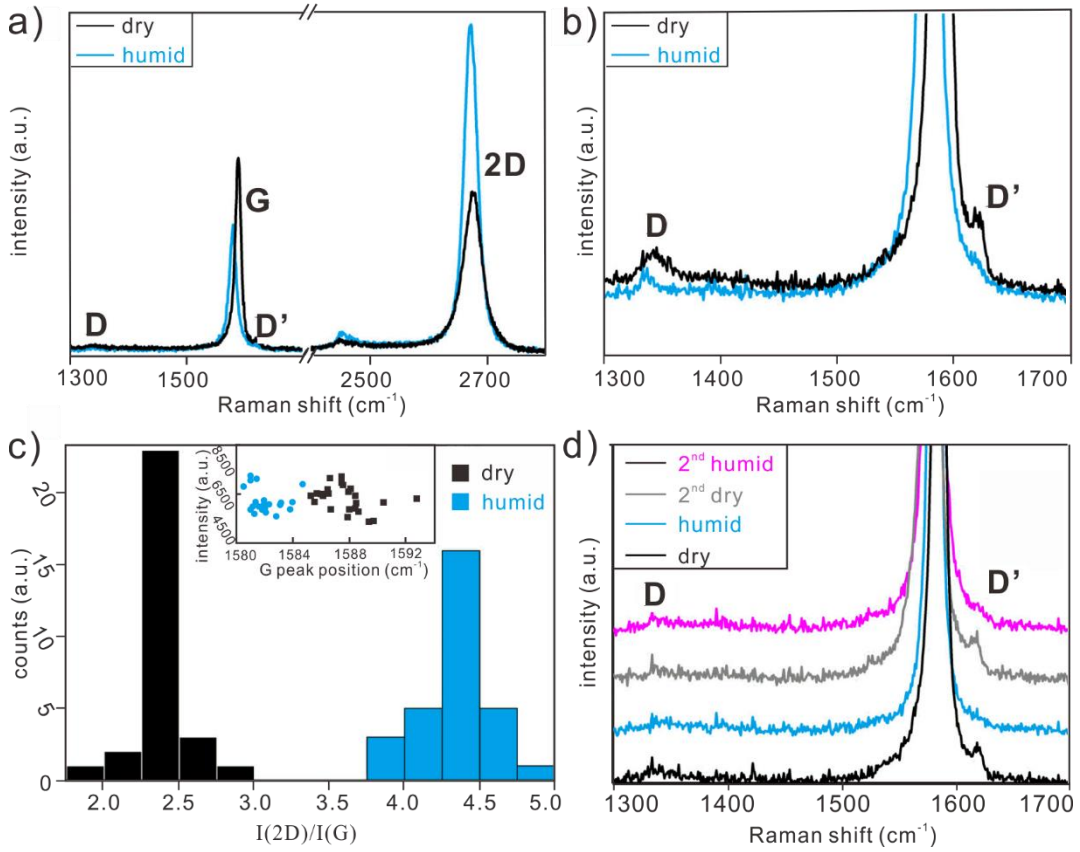

Figure 5.1.2: a) Raman spectra obtained on a SLG in dry (black line) and humid (RH 50%, cyan line) nitrogen environment. The G, 2D, D, and D' peaks are labeled. b) Magnified D and D' spectral and intensity ranges. c) Histograms of peak intensity ratios for 2D to G (I(2D)/I(G)) for dry (black) and humidified (cyan) SLGs. The inset shows the G peak intensity of all spectra for dry (black) and humid (cyan) cases. d) Raman spectra acquired on another SLG used to test a D' reactivation prediction in dry (black line), humidified (RH 50%, cyan line), dried again (RH 2.5%, gray line), and rehumidified (RH 50%, magenta line) nitrogen environments. (Adapted from Ref. [23])

The G peak intensity from my samples does not vary significantly for both dry and humid cases, with a standard deviation 8% of the mean value (**Figure 5.1.2c inset**). The intensity here and in the following means the integrated peak intensity (peak area), not the peak height. G peak intensity is argued to be insensitive to the properties of SLG and its surroundings (see explanation in **Section 3.2.2**). Thus, other peaks are typically normalized to the G intensity in order to compare different experiments. The minor difference can be induced by differences in the mica thickness and drifts of the focal plane. The 2D intensities increase from dry to humid (**Figure 5.1.2c**) by analyzing $\langle I(2D)|I(G)\rangle$: 2.4 $\pm$ 0.2 (dry) to 4.3 $\pm$ 0.2 (humid). The

errors here and in the following are the standard error unless specified.

Raman spectra of dry SLGs show D' peaks centered at 1621 ± 1.2 cm^{-1} (Figure 5.1.2b). The D' peak nearly disappears after exposing samples to humid nitrogen (Figure 5.1.2b, d), with peak intensities normalized to G peak $\langle I(D')|I(G)\rangle$ decreasing from (1.3 ± 0.4) × 10^{-2} (dry) to (0.2 ± 0.1) × 10^{-2} (humid) and peak heights normalized to 2D $\langle H(D')|H(2D)\rangle$ changing from 2.9 ± 0.6 × 10^{-2} (dry) to 0.4 ± 0.3 × 10^{-2} (humid). The intensity of D' peaks reproducibly decreases and increases upon subsequent drying and rehumidifying of a SLG sample, while the D intensity does not noticeably vary regardless of the RH changes (Figure 5.1.2d).

Figure 5.1.3a shows the 2D *versus* G peak position dependence (ω(2D)/ω(G)), which is commonly used to differentiate between doping and strain (see introduction in Section 3.2.3). The ω(2D)/ω(G) scatter significantly for dry samples. The scattering can be fitted with a line of slope 2.2 ± 0.1. Exposure to 50% RH shifts both peak positions to a more limited area. Along with the position changes, both peak widths also change from dry to humid (Figure 5.1.3b): The G peak FWHM (Γ(G)) increases from 9.1 ± 1.2 cm^{-1} to 14.1 ± 1.5 cm^{-1}, while the 2D peak FWHM (Γ(2D)) decreases from 31.2 ± 2.4cm^{-1} to 23.8 ± 1.1 cm^{-1}. Γ(2D)/Γ(G) for dry samples scatter, and the scattering can be well fitted with a line of 1.7 ± 0.2 slope.

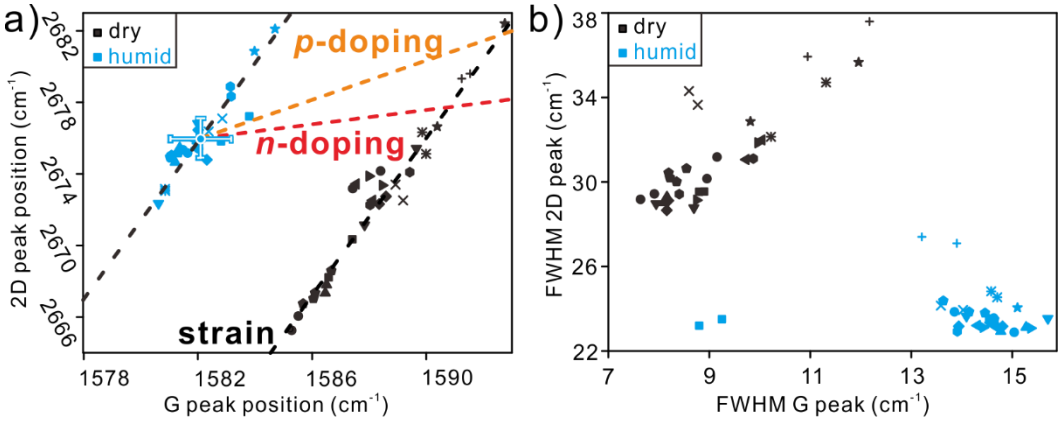

Figure 5.1.3: a) 2D *versus* G peak positions (ω(2D)/ω(G)) and b) FWHMs for dry (black symbols) and humid (cyan symbols) SLGs. Different symbols show results from different SLG pieces. The cyan circle in a) shows the averaged ω(2D)/ω(G) for the humid SLGs with error bars being the sum of standard errors and the instrument error. Orange and red dashed lines have slopes of 0.55 and 0.2 for expected shifts of both peaks for *p*- and *n*-doping effects, respectively;[86, 95] black dashed lines have the slope of 2.2 for strain effect.[93] (Adapted from Ref. [23])

5.1.4 Discussion

The contrasts in SFM phase images can be interpreted as the differences in

the tip-surface interactions.[114] Thus no phase contrast between water islands and the dry graphene areas (**Figure 5.1.1d**) implies that water islands are confined in the slit pore between graphene and mica rather than residing on top of graphene at 15% RH. Since graphene is impermeable to small molecules, the islands can be attributed to water molecules intercalating into the slit pore from graphene edges. And this was indeed observed in **Figure 5.1.1c**, where water islands were found initially on the edge of the graphene. The labyrinthine nanostructure of the wetting layer was explained with a competition of long-range electrostatic dipole-dipole repulsion and short-range line tension. The former probably stems from the repulsion between neighboring water dipoles due to their similar orientation at the interface, while the latter may be caused by the deformation of graphene at the boundaries of the wetted domains.[24] The height of the islands implies the water layer to be monomolecularly thick (~ 2.8 Å),[115] which is smaller than the expected height of an I_h-ice bilayer (~ 3.7 Å, **Figure 3.1**). Moreover, the subsequent dewetting of the slit pore leads to the growth of fractals. These indicate the fluidity characteristics of this molecularly thick water layer. As mentioned in **Section 3.1**, however, some previous studies argued that at ambient conditions, there might be two layers of water molecules wetting the graphene-mica interface. And the two layers might exhibit different phases, *i.e.*, the bottom layer is ice-like thus more stable, while the second layer is fluid and easy to evaporate. And SFM imaging could just characterize the morphology changes in the second fluid-like layer.[22] Thus, the SFM data alone cannot exclude the existence of the first layer. Especially, some theoretical studies argued that the freshly cleaved mica surface can be immediately covered with a water layer prior to exfoliating graphenes, *i.e.*, graphenes already resided on a layer of water under "dry" conditions even with a few percent RH of water.[116] The Raman data imply that it is not the case, *i.e.*, SLGs lied directly on the mica surface, or more precisely to say, SLGs were in direct contact with K^+ ions on the mica surface after exfoliation under dry nitrogen, as I will discuss in the following.

The structural defects in graphene activate both D and D' peaks around 1350 and 1621 cm^{-1}, respectively, with the intensity of the D peak typically exceeding the D' peak (**Figure 3.6**).[63] The intensity ratio of D to D' is sensitive to the type of defect.[117] The decrease in the D' peak intensity while the D peak remaining unchanged indicates that the D' peak in my samples does not originate from structural defects in graphene. Charge impurities in the vicinity of the graphene plane were theoretically predicted to selectively activate the D' peak.[117] The calculations based on 10^{12} e^-/cm^2 charge impurity density predicted a quite small D' peak, with the height normalized to 2D peak $\langle H(D')|H(2D)\rangle = 1.7 \times 10^{-4}$ (as extracted from Ref.[117], Figure 18). The mica structure is shown in **Figure 2.4**. Half of the K^+ ions are assumed to remain on either surface after cleavage of mica, yet the exact K^+ distribution is unknown.[29] The hexagonal unit cell of mica with the cell side of ~ 5.2 Å has one K^+ within the center. Thus, assuming half of K^+ ions remained after cleavage should give rise to a K^+ surface density of ~ 2×10^{14} cm^{-2}, *i.e.*, ~ 200 times larger than the value taken in the calculations. The $\langle H(D')|H(2D)\rangle$ for my dry

graphenes is (2.9 ± 0.6) × 10^{-2}, which is also 200 times larger than the calculated results. Therefore, it is reasonable to attribute the small D' peak in my samples to a direct contact of SLG with the K^+ ions, and its disappearance at high RH can be attributed to a monomolecular water layer decoupling graphene from the ionic mica surface. Dewetting the hydrated slit pore caused by exposure of sample to dry nitrogen results in depressions in the water monolayer (**Figure 5.1.1e**), where graphene is expected to get again in direct contract with the K^+ layer. Therefore, one can expect such dewetting to partially reactivate the D' peak. Indeed, the data in **Figure 5.1.2d** support the prediction. Thus, the D' peak observed in dry sample spectra evidences that SLGs are in a direct contact with K^+ ions on dry mica surface.

Doping and Strain in graphene shift 2D/G peak position dependences (ω(2D)/ω(G)) with different ratios (see introduction in **Section 3.2.3**).[93] Tensile/compressive strains downshift/upshift ω(2D)/ω(G) along a line of ~ 2.2 slope, respectively. While *p*- and *n*-doping upshift ω(2D)/ω(G) linearly with slopes of 0.55 and 0.2, for low doping levels (< 10^{13} e^-/cm^2 as in my samples). The strain and doping effects on ω(2D)/ω(G) are additive, *i.e.*, expected 2D and G peak positions for strained and doped graphene are composed of the shifts expected for strain and doping, respectively (**Section, 3.2.3, Figure 3.14**). To quantitatively discuss the position shifts, it is essential to find out the peak positions for undoped and unstrained graphene. According to Ref.[86] (see also **Figure 3.11**), the G peak position for undoped SLG is expected to be ~1583.1 cm^{-1}. This value is in good agreement with the data acquired from free-standing SLGs, which were assumed to be nearly undoped and unstrained.[93] The averaged G peak position of humidified SLGs in my case is ~ 1582.1 ± 1.4 cm^{-1} (**Figure 5.1.3a**), which conforms to the literature values, and the data scatter somewhat along the line of 2.2 slope for strain. Therefore, I conclude that the SLGs with a water layer underneath are undoped and slightly strained. Yet It has been argued that screening by a dielectric substrate reduces the electron-phonon coupling at the high-symmetry point K. And this results in an upshift of the 2D peak.[118] Furthermore, 2D peak positions are linearly dependent on the energy of excitation lasers albeit with slopes in the range of 80 – 100 cm^{-1}/eV.[82] All these factors make discussions on the 2D peak of absolutely unstrained graphene on mica very difficult. However, the averaged 2D/G peak positions from my hydrated samples agree with the previously reported ones that were argued to be undoped and unstrained.[18] Thus, I assume the 2D/G peak position for unstrained and undoped graphene resting on mica to be ω(G) = 1582.1 ± 1.4 cm^{-1} and ω(2D) = 2676.0 ± 1.3 cm^{-1} (cyan circle in **Figure 5.1.3a**). The assumption of undoped SLGs by water layer is further supported by the large I(2D)/I(G), and the large G peak FWHM expected for the undoped graphene (**Figure 3.11**).[86]

The ω(2D)/ω(G) scattering for dry samples along the line of 2.2 slope is attributed to different strains in SLGs (**Figure 5.1.3a**). The dry SLGs must be uniformly doped but variably strained with tensile strain dominating over compressive strain. The data so far do not allow distinguishing *p*- or *n*-doping in my

samples. The question remains still debated as it has been explained in the review of literature in Section 3.3.1. It is tempting to assign the tensile strain to graphene deformation on the K^+ ions (Figure 5.1.4a). The average distance between the remained K^+ ions is ~ 0.7 nm after cleavage. Yet the SFM resolution in tapping mode is not sufficient to resolve the individual K^+. The 2D and G peak FWHMs (Γ(2D), Γ(G)) from dry samples both exceed the ones for doped and unstrained SLGs shown in Section 3.2.2. The Γ(2D)/Γ(G) for dry SLGs shows a linear dependence with a slope close to 2.2 (Figure 5.1.3b). Furthermore, the FWHMs and peak positions are rather reproducible within a given SLG piece but vary from piece to piece (Figure 5.1.3a, b). The reproducible broadening of the peaks may be due to local strains in graphene, resulting from the misalignment between graphene and K^+ lattices, similarly to the case of graphene on h-BN.[119] This is expected to cause inhomogeneous broadening of both peaks with the Γ(2D)/Γ(G) scattering along the slope of 2.2 ± 0.2 for strain (Figure 5.1.3b). The G peak width is more sensitive to doping as a consequence of the electron-phonon interaction (as introduced in Section 3.2.2). The doping results in significant G peak narrowing, which is not accompanied by a strong 2D peak narrowing (Figure 5.1.3b).

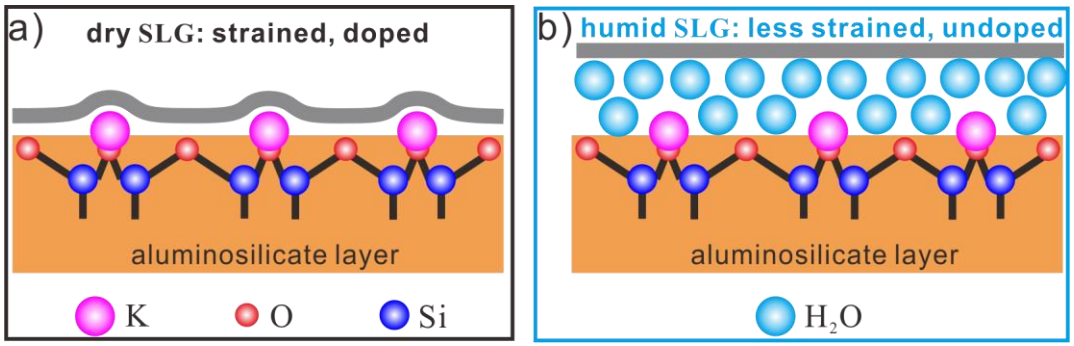

Figure 5.1.4: a) Cleavage of mica presumably removes half of K^+ ions. SLGs become reasonably strained when exfoliated onto such a surface. b) A monolayer of water molecules filling into the slit pore between graphene and mica, possibly fills also the gaps between the K^+ ions removing thereby tensile strain in graphene. (Adapted from Ref. [23])

The gaps between the K^+ ions are ~ 7 Å after cleavage, assuming half of them remained on the mica surface. The size of the K^+ ion roughly equals the one for a water molecule.[120] Thus, water molecules are expected to fill the gaps between the K^+ ions, effectively flattening the mica surface and thus removing the tensile strain in graphene (Figure 5.1.4a, b). The rest of random strains are possibly inherited from preparation and persistent throughout the whole measurements. The water islands observed by SFM are molecularly thick (~ 2.8 Å), implying a monolayer of water molecules growing on top of the first mixed layer of K^+ ions and water molecules (Figure 5.1.3b).

5.1.5 Conclusion

Graphene on dry mica is doped and strained, while a molecularly thin water layer at 50% RH wets the graphene-mica slit pore, decoupling graphene from mica both mechanically and electrostatically. The disappearance of D' peak upon wetting and reappearance upon dewetting the slit pore implies a direct contact of the graphene with the K^+ ions on mica surface in dry condition, yet I cannot exclude that the gaps between K^+ ions are initially filled with water molecules even in a few ppm of water. The water molecules wetting the slit pore may mix with the K^+ ions that remained on the cleaved mica surface. The reversible dewetting of the thin water layer indicates this molecular layer is fluid, yet the state of water molecules filled in the gaps between K^+ ions remains unclear. They might exhibit ice-like properties, as previous MD simulations predict that these water molecules are bound to mica via hydrogen bondings. They are confined between K^+ ions, potentially forming more ordered and stable structures.

This part of my work demonstrates that Raman spectroscopy allows unraveling strain and doping in graphene upon wetting and dewetting of a graphene-mica slit pore with a monomolecularly thin water layer. The graphene-mica slit pore is an attractive experimental tool for a better understanding of strain and charge-transfer influences on the sorption of liquids by porous materials and transport of liquids in nanoconfinement.

5.2 Reversible Switching of Interfacial Charge Transfer with Intercalating Molecular Layers

5.2.1 Introduction

The work in **Section 5.1** suggests that a water molecular layer wetting the graphene-mica slit pore, decouples graphene from mica both mechanically and electronically, thus removing doping and reducing strain of graphene.[23] However, the charge source causing doping of graphene as well as the effect of charge transfer at the interface was not well discussed. For example, it needs to clarify whether the intercalated water layer can *p*- or *n*-dope graphene. And it is also essential to differentiate the influences between water intercalated in the slit pore and water adsorbed on the graphene surface. In this section, the influence of intercalated water layer and organic layers (ethanol, acetone and 2-propanol) as comparisons on graphene doping was further investigated by Raman spectroscopy.

The electronic properties of interfaces dominate the performance of electronic devices. Smaller molecules intercalated into interfaces can influence their properties such as modifying the energy level alignment at the interfaces.[121, 122] The role of water molecules adsorbed at interfaces is being recognized. For example, the dipole moment of the water layer between an electrode/organic-semiconductor interface affects the transport characteristics of the electronic device.[123] Water molecules confined in graphene-mica slit pore were shown to orientate normally to the interface and result in a net dipole moment, which influences graphene doping.[22] The confinement, on one hand, determines the orientation of water molecules; on the other hand, the orientated water dipole exhibits significant influences on electronic behavior at the interface. What if other small molecules with comparable or larger molecular dipole than that of water (1.9 D) intercalate into the interface? *e.g.*, ethanol and acetone (1.7 D and 2.9 D).[124] Will ethanol behave similarly to water at the interface, while the larger acetone dipoles have a stronger effect on the interface properties? Raman spectroscopy probing graphene doping affected by the intercalated liquid layers might allow understanding the charge transfer mechanism through molecular layers at interfaces, which is of use to further comprehend the interplay between liquid molecular layers and the graphene-mica confinement. Furthermore, understanding of interfacial charge transfer is advantageous for not only design of organic electronic devices, but also for contact electrification or in bio-electronics.[122, 125]

Thus, I investigated the effects of intercalated layers (water and organic solvents) on charge transfer in the well-defined graphene-mica slit pore, which can be regarded as a model between an insulator (mica) and a conductor (graphene). An initially dry graphene-mica interface was exposed to vapors of the aforementioned

liquids. I will show that the molecules can diffuse into the interface to form molecular layers, and water and organic molecular layers can reversibly replace one another. Raman results revealed that the charge transfer between SLG and mica was blocked with molecular water layer intercalation, but allowed by the layers of organic solvents. Furthermore, exchanging of the intercalated water and ethanol layer results in switching of the interfacial charge transfer off and on. I infer from the Raman results that the molecular dipole layers produce different quantities of electrostatic potential, which dominate the charge transfer between occupied mica trap states and graphene electronic states. And this is supported by MD simulations.

5.2.2 Experimental

Dry Graphene-mica slit pores were prepared and sealed in the steel cell with the same method described in **Section 5.1**. Then the sample cell was connected to the gas-control setup (**Section 4.3.1**) for different Raman measurements:

I) To investigate the influence of confined liquid layers on graphene doping and strain, sixteen SLG pieces were optically detected and measured by Raman spectroscopy in dry nitrogen first and then in different liquid vapors. The details are described in the following: i) three dry SLG pieces were directly exposed to water vapor (50% RH); ii) one was directly exposed to acetone, and iii) another one was exposed to 2-propanol vapor; iv) the other 11 dry SLGs were sequentially exposed to the vapors of ethanol, then water, and then ethanol again. In addition, I repeated 4 times the ethanol/water-exposure cycles on one of the SLGs.

II) To clarify if liquid molecules adsorbed on graphene top surface also contribute to graphene doping, another three dry SLGs were exposed to humidified nitrogen. RH was first increased and then decreased in small steps of ~ 5%. Raman spectra were then acquired on different positions of every SLG about 20 minutes after stabling RH at a desired value. After the measurements in humid nitrogen, the humid SLGs were exposed to ambient air. And Raman spectra were acquired on the SLGs over time to investigate the influence of ambient air on graphene doping.

Raman measurements were conducted with instrumental settings different from those used in **Section 5.1**. For example, an 1800 lines/mm grating was employed. The spectra used for calculations of peak FWHM and peak intensity calculations were acquired with 50 µm and 300 µm slit and hole sizes respectively. The spectra for peak position analyses were obtained with 100 µm and 300 µm slit and hole sizes. Raman peaks were fitted with Pseudo-Voigt functions. These settings were intended to facilitate the faster acquisition of the Raman spectra or improve the spectra quality. But the difference in these settings also causes slight changes on the position and width of graphene Raman peaks, and this will be specified later in the results.

I will introduce in the following another Raman instrument calibration method employed in the work of this section, as I found that the previous calibration method using benzonitrile and cyclohexane (**Section 5.1**) has a few disadvantages. The potential calibration drifts include the linear drift caused by mechanical displacement in the Raman spectrometer such as the mechanical motion of gratings, and the nonlinear one possibly stemmed from ambient temperature variations. The linear drifts can be corrected by using benzonitrile and cyclohexane peaks as references before and after each day of Raman measurements. But this does not account for the nonlinear drifts during the *in situ* Raman measurements over a day. I later found that such drifts could amount up to 3 cm^{-1} over a day. For this, I placed a neon lamp (NE-1, Ocean optics) in front of the samples. This allows to simultaneously record the Raman spectra of graphenes and emission spectra of the neon. The neon spectral lines have constant energy differences with the Raman laser, therefore can be used as references to correct the calibration drifts in each Raman spectrum. And the drifts are expected to be uniform along the spectral field.[126] I used one intense neon line at 585.25nm as the reference,[127] which closes to graphene G peak. This aids to minimize the random error of my Raman data.

5.2.3 Results

Figure 5.2.1a shows typical Raman spectra acquired on an SLG exfoliated onto a freshly cleaved mica surface under initially dry nitrogen and then subsequently being exposed to ethanol vapor and water vapor. Similar to the previous section, the G and 2D peak position, FWHM, and intensity changes will be analyzed in the following in more detail. Notably, the small D' peak erecting in the spectrum of dry graphene, which is attributed to the SLG being in direct contact with K^+ ions on the mica surface (**Section 5.1.4**), disappears in both ethanol and water vapor (**Figure 5.2.1b**).

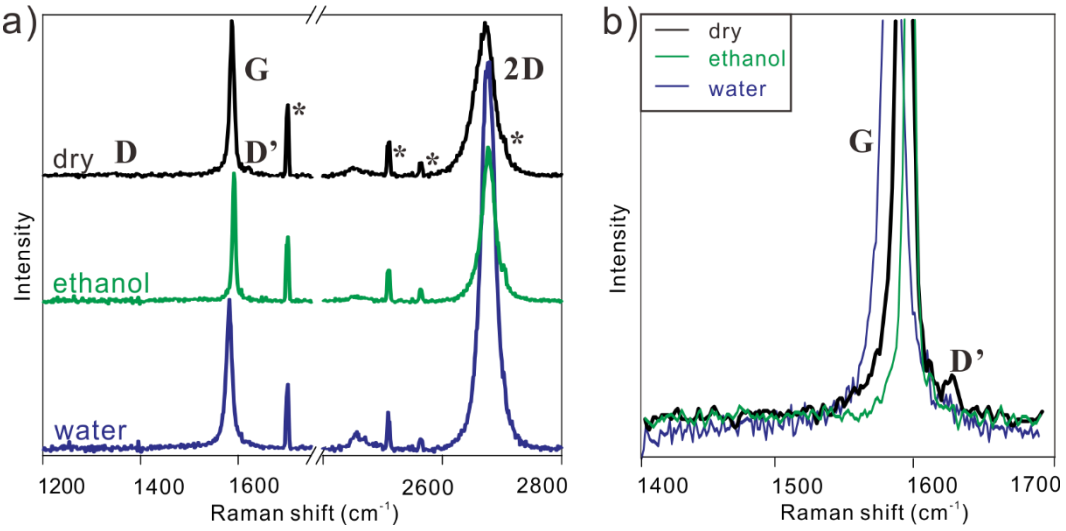

Figure 5.2.1: a) Raman spectra of SLG kept in i) dry nitrogen (black line), then ii) dry

nitrogen bubbling through ethanol (green line) and iii) water (~50% RH, blue line) sequentially. The neon peaks labeled with asterisks (*) are used as calibration standards. b) Close-up of D' peak spectral and intensity ranges. The D' peak was deactivated when the dry SLG (black line) was exposed to ethanol vapor (green line) and humid nitrogen (blue line). (Adapted from Ref. [36])

2D on G peak position dependence (ω(2D)/ω(G)) is again plotted to unravel the strain and doping effects (**Figure 5.2.2a**). The graph reveals that the dry SLGs were both variously strained and diversely charge doped (**Figure 5.2.2a**). Strain variations match the results for dry SLGs reported in **Section 5.1**, while the doping scatters more. To verify that intercalation of the water layer renders graphene to be undoped and unstrained, three dry SLGs were exposed directly to ~ 50% RH. Their 2D/G positions are shown in **Figure 5.2.2d**, and the 2D/G position average is shown with a cyan circle including error bars in **Figure 5.2.2a**. With the improved calibration method using neon lines, the averaged G (1583.0 ± 0.8 cm^{-1}) and 2D (2677.2 ± 0.7 cm^{-1}) peak position are consistent with the previous result. Therefore, the peak positions are assumed in the following as for the undoped and unstrained SLG. For other 11 dry SLGs, exposure to ethanol compacts the ω(2D)/ω(G) to a spot around 1592.5 ± 0.8 cm^{-1} and 2678.5 ± 0.7 cm^{-1} (green circle with error bars in **Figure 5.2.2a**). Subsequent exposure to humid nitrogen shifts the peak positions towards the undoped, unstrained point**.** The peak positions scatter around the red line (for *n*-doping) and close to the spot for highly *n*-doped and unstrained SLG (the solid green circle) when these SLGs were exposed to ethanol again after water. Another two initially dry SLGs were separately exposed to acetone and 2-propanol, their 2D/G positions are shown in **Figure 5.2.2e**. Their averaged ω(2D)/ω(G) are shown with purple and pink circles in **Figure 5.2.2a**. They are almost at the same position as the one for the ethanol case within the error range.

Both 2D, G peak intensity ratios and FWHMs for the dry case and pure water case (**Figure 5.2.2b, c**) are similar to that reported in **Section 5.1**. The slight differences between them are due to the different fitting functions and scanning settings. Exposure of the samples to ethanol vapor narrows both peaks and reduces the ratios.

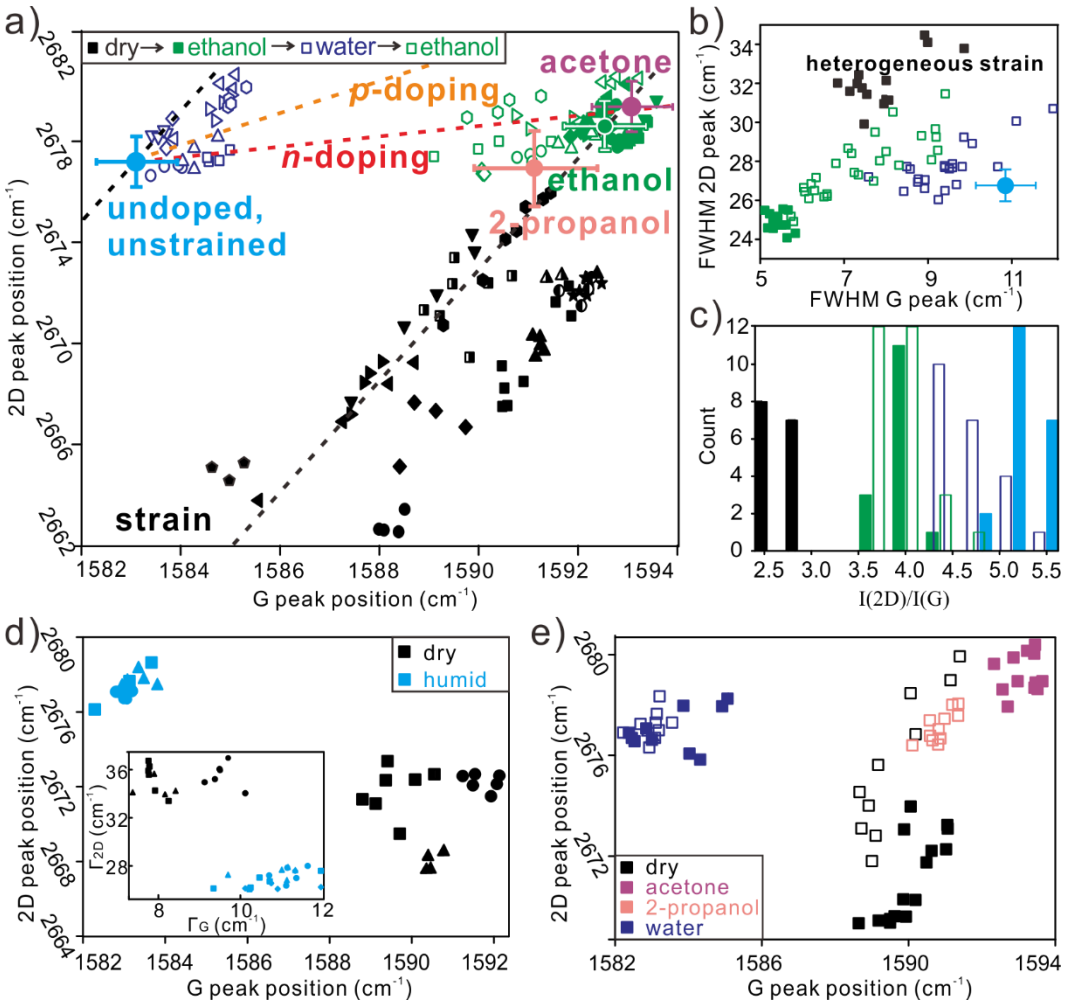

Figure 5.2.2: a) 2D *versus* G peak positions (ω(2D)/ω(G)) and b) FWHMs (Γ(2D)/ Γ(G)) recorded from 11 dry SLGs (filled black symbols) exposed to ethanol (filled green symbols), then water vapor (unfilled blue symbols) and re-exposed to ethanol vapor (unfilled green symbols). Results for different SLGs are noted with different symbols. c) Histograms of peak intensity ratios for 2D to G (I(2D)/I(G)) for SLGs in different vapors. d) ω(2D)/ω(G) and FWHMs (inset) for direct exposure of another three dry SLGs to humid nitrogen. The average of the peak positions and FWHM s are shown with cyan circles in a) and b). They are expected for the unstrained and undoped SLG. e) ω(2D)/ω(G) for direct exposure of one dry SLGs to acetone (filled purple symbols) and another one to 2-propanol (unfilled pink symbols). The averaged ω(2D)/ω(G) for acetone and 2-propanol cases are shown in a) with the purple and pink circles and the error bars. The averaged ω(2D)/ω(G) for the ethanol case is shown with a green circle and error bars. The dashed lines with different ratios in a) represent the expected ω(2D)/ω(G) shifts for strain, *p*- and *n*-doping (same as in Figure 5.1.3). (Adapted from Ref. [36])

The ω(2D)/ω(G) shifts in a nearly reversible way when exchanging exposure of the 11 SLGs in water and ethanol vapor, as shown in Figure 5.2.2a. To investigate the kinetics of the peak shifts, I continuously recorded G peak positions from the roughly same position of an SLG after switching of ethanol and water (Figure 5.2.3a).

G peak is more susceptible to doping (see explanation in Section 3.2.2). The G peak changes over time imply that doping in graphene increased with longer time in ethanol vapor while decreased in water. Repeated 4 times the ethanol/water-exposure cycles, the G peak positions show repeatedly reversible changes depending on vapors (Figure 5.2.3b).

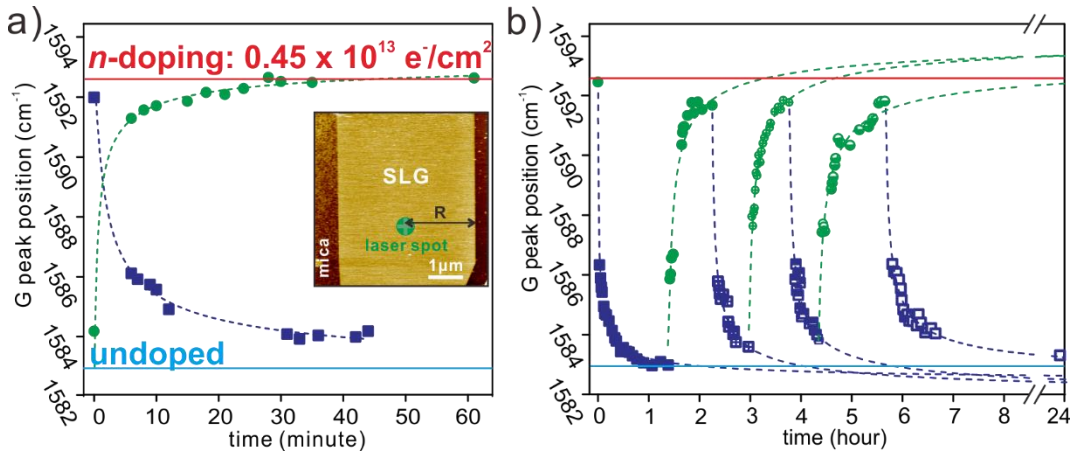

Figure 5.2.3: a) ω(G) dependences on time for water replacing ethanol (blue symbols) and ethanol replacing water (green symbols). The time at zero is when nitrogen flowed through the respective liquid. The inset shows the SFM height image of the SLG on mica. The green spot is the estimated Raman laser position. The distance from the laser spot to graphene edge *R* is estimated to be 2 μm. b) ω(G) dependences on time for another SLG being exposed alternately to ethanol (green symbols) and water (blue symbols) vapor. The dashed lines are fits with the diffusion equation solutions (equation 5.2). The solid cyan and red lines represent ω(G) for unstrained, undoped, and *n*-doped graphene calculated with equation 5.1. (Adapted from Ref. [36])

As introduced in Section 3.3.1, water molecules intercalated at the graphene-substrate interface change graphene doping. In addition, those adsorbed on graphene top surface might also influence the doping to some extent. Therefore, for the graphene-mica system I investigated, it's necessary to clarify the charge source causing the doping of graphene. Whether charge transfer from water adsorbed on the top surface of graphene or intercalated at the slit pore dominates the graphene doping. My previous SFM results showed that water started to wet the graphene – mica slit pore at ~ 15% RH (Figure 5.1.1d). No intercalation of water occurred at a lower RH. For this, I performed *in situ* Raman measurements on three initially dry SLG pieces upon increasing RH from 2% to 50% in steps. Figure 5.2.4 a) and b) shows the 2D *versus* G peak position (ω(2D)/ω(G)) changes for the three pieces and the typical Raman spectra at different RHs during wetting. No peak shift and intensity change are observed up to 10% RH. Water wetting the slit pore caused Raman spectra changes starting from 15% RH, and the ω(2D)/ω(G) shifted to the point for undoped and unstrained SLG at 50% RH. After that, one humid SLG piece was exposed directly to ambient air, and I recorded its 2D/G peaks after exposure in

ambient for about 1 hour and 24 hours. The ambient humidity was about 38%. This is high enough to maintain the integrity of the water molecular layer in the slit pore. Because the dewetting of the slit pore only starts from the RH lower than ~10%.[17] Thus, the 2D/G peak changes reveal the influence of ambient air on graphene doping without strain interference. The 2D/G peaks upshifted over time in ambient, and the fit of the data gives a slope of 0.56 ± 0.06 (Figure 5.2.4c). This agrees well with the expected shift for *p*-doping.

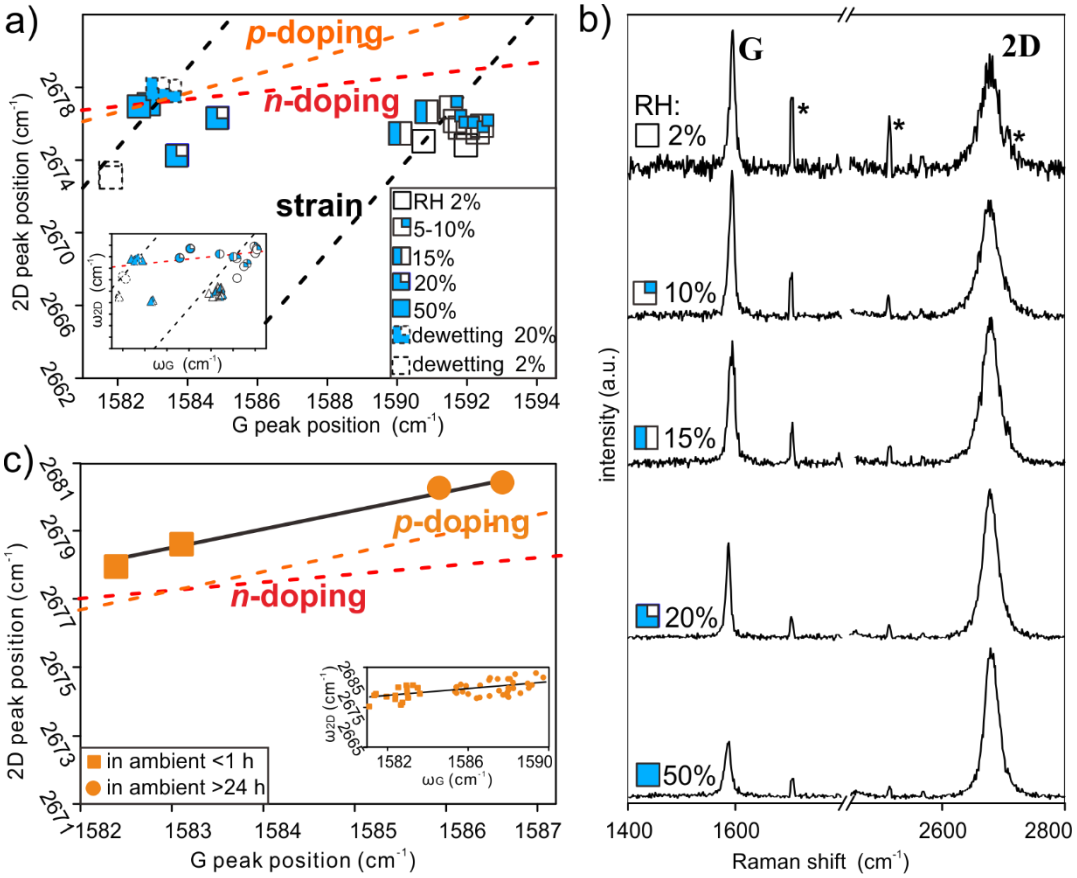

Figure 5.2.4 a) Typical ω(2D)/ω(G) and b) Raman spectra for an SLG piece in initial dry (open black symbols), then at variable RHs (partially-filled light blue symbols). RH was first increased from 2% to 50% then decreased to 2% again in steps, each step is indicated with different symbols. The inset in a) shows the data from another two pieces measured in the same way, showing similar changes at variable RHs. c) ω(2D)/ω(G) for exposure of the humid SLG to ambient air. The data were acquired over time from the roughly same spot on the SLG. The inset shows the statistics of data acquired from more graphene pieces exposed in ambient. The solid lines are the linear fits of the respective data. The black, red, and orange dashed lines have slopes of 2.2 and 0.2 and 0.55, respectively. They are the expected shifts of 2D/G for strain, *n*- and *p*-doping.[86, 93, 95] (Adapted from Ref. [36])

5.2.4 Discussion

The D' peak has already been discussed in Section 5.1. It can originate from

the charge impurities in the vicinity of the graphene plane. Direct contact of SLG with the K^+ ions on the mica surface activated a discernable D' peak, whereas a molecularly thin water layer intercalating the graphene-mica slit pore decoupled SLG from the ionic surface, and thus deactivated the D' peak (**Figure 5.1.2b**). Exposure of dry SLG to ethanol vapor suppressed the D' peak as well (**Figure 5.2.1b**). This implies ethanol molecules diffused into the graphene-mica slit pore, and decoupled SLG from mica in a way akin to water. Indeed, the previous SFM study already showed that a thin ethanol layer could intercalate into the slit pore.[128, 129]

As shown in **Figure 5.2.2a**, the ω(2D)/ω(G) from ethanol intercalated SLGs (the solid green symbols) become compacted to around the intersection point of the lines for *n*-doping and strain effect. This suggests (0.45 ± 0.02) x 10^{13} e^-/cm^2 *n*-doping and zero strain induced by ethanol intercalation. The charge is calculated with the following equation:[85, 86]

$$\Delta\omega = \alpha' |\nu_F| \sqrt{\pi n} \qquad (5.1)$$

where, Δω is the angular frequency shift of G peak between undoped SLG by water and doped SLG by ethanol, $\alpha' = 4.39 \times 10^{-3}$, Fermi velocity $|\nu_F| = 1.1 \times 10^6\ ms^{-1}$, n is the charge concentration in units of e^-/cm^2. The nearly zero strain of SLGs in ethanol vapor further supports the assumption on the ethanol layer intercalating into the slit pore, since ethanol molecules adsorbed on the top surface of SLGs are not expected to reduce strain. The ethanol layer lubricates the interface, reducing strain thus influencing 2D and G peak FWHMs (**Figure 5.2.2b**). The heterogeneous strain in dry SLGs induced by direct contact with mica broadened both 2D and G peaks, as already shown in **Section 5.1 (Figure 5.1.3b)**. Intercalation of the ethanol layer mechanically decoupling SLG from mica relaxed most strain and consequently narrowed both peaks. Besides, the G peak FWHMs of SLGs exposed to ethanol are consistent with that of reported doped SLGs (**Figure 3.10b**).[86] Moreover, the ethanol layer increases the 2D/G peak intensity ratios compared to the dry case (**Figure 5.2.2c**), although the doping of SLGs in both dry and ethanol vapor are similar. Doping modifies graphene Fermi level, suppressing 2D peak due to reduced opportunity for electrons-phonon interactions (see explanation in **Section 3.2.2**). Therefore it is reasonable that the 2D peak of dry SLG is further suppressed by the electrostatic interaction of SLG with the K^+ ions on mica compared to that in ethanol case. Thus, the larger 2D peak intensity in ethanol cases also suggests that the intercalated ethanol layer separated graphene from the K^+ ions. This conclusion is supported by the suppression of D' peak in ethanol vapor (**Figure 5.2.1b**).

Figure 5.2.2a shows a large variation of both strain and doping of dry SLGs. Strain variation results from the deposition of SLGs on the rough mica surface with K^+ ions thereon. In the following, I will discuss the reason for the doping scattering in dry and its removal by ethanol intercalation. A mica surface cleaved under dry

nitrogen is known to exhibit charged domains.[29, 130] Water adsorbed on the mica surface is reported to remove such charged domains, which is attributed to the higher conductivity of the mica surface after hydration.[131-133] I propose that the most charge in dry SLGs stemmed from charge transfer from the mica substrate. And alongside this, the other small proportion of charge was inducted from the randomly charged domains on freshly cleaved mica surface. I assume that the ethanol layer can remove the charged domains similarly to water by enhancing the conductivity of the mica surface. This assumption implies that the charge in SLGs with ethanol intercalation was mainly transferred from the mica upon direct contact, and the ethanol intercalating layer did not disturb the charge transfer. From the results in **Section 5.1**, we know that water layer intercalating the slit pore renders graphene undoped. And the previous SFM study shows that the intercalated water and ethanol molecules can exchange with each other in the slit pore.[128] What will the graphene doping change if we expose the graphene from ethanol to water vapor? The ω(2D)/ω(G) results in **Figure 5.2.2a** imply that SLGs became from *n*-doped to undoped from ethanol to water case. This reveals that the SLGs became significantly less charged after exposure from ethanol to water vapor. The conclusion is also confirmed by broadened G peak and increased I(2D)/I((G) (**Figure 5.2.2b, c**).[23, 86]

Likewise, one might expect that the water layer replacing the ethanol layer should restore the charge in graphene. Indeed, the doping of SLGs was almost restored after exposure of the samples to ethanol vapor again, as one can infer it from the upshifts of G and 2D peaks along the line for *n*-doping (**Figure 5.2.2a**). Narrowed G peaks and decreased I(2D)/I(G) (**Figure 5.2.2b, c**) again support the conclusion that the ethanol intercalating layer increased doping in SLGs. The results support that water and ethanol molecules intercalating the graphene-mica interface blocked and did not affect the charge transfer, respectively.

In the following I will discuss the kinetics of the ω(2D)/ω(G) shift caused by the exchange between ethanol and water. Water and ethanol molecules can both intercalate into the slit pore and diffuse in the mixed phases.[128] To investigate the influence of the diffusion process on graphene doping, I plot the G peak positions as a function of time after swapping between ethanol and water (**Figure 5.2.3a**). Because the G peak position is more sensitive to doping than the 2D peak (see explanation in **Section 3.2.2**). The data fit well into the solution of a one-dimensional diffusional equation:[128]

$$G(t) = G_{Eth} - p(G_{Eth} - G_{H2O})erf\left(\frac{R}{\sqrt{4D(t-t_0)}}\right) \quad (5.2)$$

where, G_{Eth} and G_{H2O} are the G peak positions for ethanol and water-filled interface respectively, R is the distance from the laser spot to the graphene edge (~ 2 µm, **Figure 5.2.3a**), t is the time and D is the diffusional constant. p = 1 for ethanol

replacing water and -1 for water replacing ethanol. The results imply a linear relationship between the charge in SLGs and the number of ethanol molecules confined at the interface, namely, the charge in SLGs is determined by the configuration of the confined molecular liquid film. **Figure 5.2.3b** demonstrates charge transfer at the interface can be switched by exchanging the ethanol/water layer for a few cycles, albeit the kinetics of switching decreases from cycle to cycle. I ascribe this slowdown to contaminations possibly adsorbing at the graphene edges and thereby hindering the exchange between ethanol and water molecules. The contaminations may be a tiny amount of organic molecules not only from the nitrogen gas source, but also from the tubing and glove box parts. The contaminations are experimentally inevitable. Nevertheless, I used **equation (5.2)** to estimate the diffusion coefficients of water and ethanol molecules based on the assumptions proposed in Ref.[128] *e.g.*, the diffusion is the rate-limiting step; the ratio of concentrations of diffusing molecules at time t_0 becomes instantaneously C_{Eth}/C_{H2O} at a distance R, where R is the shortest distance estimated from the Raman laser spot to the nearest graphene edge; and t_0 is the time of dry nitrogen being rerouted through another liquid. According to the average of fits in **Figure 5.2.3b**, I calculated a lower limit of the diffusion coefficient to be 10^{-14} m^2/s, which is in the same order as the previous estimation.[128]

The results for acetone and 2-propanol case (**Figure 5.2.2a**, purple and pink circles) are similar to the ethanol case, *i.e.*, the results imply that both solvents can intercalate the initially dry graphene-mica interface as well, unaffecting the charge transfer and removing strain by lubricating the interface. In other words, the transparency of charge transfer at the interface is not specific to ethanol. Similarly, water replacing the acetone and 2-propanol molecules did suppress the charge transfer (**Figure 5.2.2e**).

Above I discussed the influence of confined molecular layers on graphene properties, one may ask if liquid molecules adsorbing on graphene top surface also influence its doping, just as I already mentioned in **Section 3.3.1**.[101] The results shown in **Figure 5.2.4** suggest no significant charge transfer between graphene and water molecules possibly adsorbing onto graphene top. I will explain this in the following. The water molecules start to intercalate into a graphene-mica slit pore at ~ 15% RH according to my results in **Section 5.1 (Figure 5.1.1d)** and the literature.[24] No water intercalates into the slit pore upon exposure of samples at lower RHs for 1 h. This is evidenced by my Raman results as well. The peak position and intensity did not change up to 10% RH, whereas the peak position shifted and 2D intensity increased upon raising RH to 15% (**Figure 5.2.4a, b**). This implies that the Raman spectra change with the onset of the water intercalation. And water molecules probably adsorbing onto the graphene top surface at lower RHs do not induce graphene doping, or at least the magnitude of doping could not be measured. The conclusion is further supported by the Raman spectra changes during dewetting process. Dewetting the slit pore was reported to start only when RH was roughly

below 10%.[17] And no peak shift down to 15% RH is found in my case. Further decreasing RH to 2% caused dewetting of the slit pore and growth of the fractal patterns (**Figure 5.1.1e**). And the 2D/G Raman peaks shifted towards the less doped and more strained direction. The adsorption energy of water molecules on graphene is comparable to *kT* at room temperature.[134] So the water layer thickness on graphene surface is expected to be in equilibrium with the water in the humid nitrogen flow at variable RHs. No Raman peak changed until the RH decreased to the threshold value (~ 10%) for dewetting the slit pore. This further supports that doping in graphene is dominated by the water layer intercalated in the slit pore, rather than that adsorbed on top of graphene.

In the following, I will propose a mechanism for charge transfer switching by the confined molecular layers. But before that, I will first discuss the direction of the charge transfer. My results suggest the *n*-doping of SLGs by charge transfer from the mica substrate, I will explain this more in the next paragraph. However, the doping of graphene by mica as well as the charge transfer direction at the interface has been disputed in the literature (as introduced in **Section 3.3.1**).[18, 21, 22, 99] My dry graphene SLGs were atomically flat (**Figure 5.1.1**), *i.e.*, I did not discern any formation of K^+ islands. Therefore, I exclude the K^+ islands as a reason for graphene doping.[99] Ambient oxygen and/or contaminations adsorbing on the SLG surface were proposed as one of the possible reasons for the doping.[21, 97] All the data abovementioned were from samples without exposure to ambient conditions. To test the influence of ambient conditions, I exposed undoped SLGs with the interface hydration by water to ambient. The ambient RH was high enough to retain the interface hydration.[17] However, the ω(2D)/ω(G) shifts along the line for *p*-doping on a time scale of an hour after exposure to ambient (**Figure 5.2.4c**). It is reported that the graphene surfaces get contaminated by airborne contaminations on the same time scale.[135, 136] Ambient oxygen is expected to adsorb onto a graphene surface much faster. Thus, in my view, the slow *p*-doping growth of my hydrated SLGs in air was caused by airborne contaminations rather than oxygen. Since most works from other groups were done with samples either prepared or measured in ambient, I assume that the reported *p*-doping of graphenes on mica were probably caused by contaminations in air.

The water layer intercalating the slit pore increases the distance between graphene and mica. Yet the confined molecularly thin layers are not expected to block the charge transfer.[137, 138] Moreover, the alcohol layers in the slit pore are thicker than that of water.[30, 129] The thicker layers of larger alcohol molecules intercalating the slit pore instead restored the charge in SLGs. Therefore, I exclude the electron tunneling blockade mechanism mentioned in Ref.[18] as a possible reason for water undoping graphene. I discard also covalent bond formation between intercalating molecules and graphene, since I do not observe any change of the D peak intensity (**Figure 5.2.1a**). The structural alterations of graphene will lead to variations in D peak intensity,[23] so chemical doping of graphene can be excepted.[63,

[77, 139] Even more, the reversible intercalation of water and ethanol molecules suggests no covalent bonding between the liquid molecules and mica as well.

In the following I will propose a mechanism for the interfacial charge transfer. With the arguments provided above, it must be mica that charge-doped graphene before the intercalation of liquids. Yet the large strain variations in dry SLGs on mica make it difficult to directly conclude whether the SLGs were *n*-doped or *p*-doped. But the ω(2D)/ω(G) results evidence that SLGs must be *n*-doped with the different intercalated organic layers. And the magnitude of *n*-doping is almost the same as the doping in dry SLGs. It's reasonable to assume that the SLGs were already *n*-doped by dry mica, and the doping was unaffected by the intercalation of the organic layers. Because if one assumes that the dry SLGs were *p*-doped on mica, I do not expect the different organic layers could reverse the sign of the doping (from *p*- to *n*-type), meanwhile inducing the same doping level in SLGs. Moreover, the *n*-doping of graphene by mica has been already predicted by the vdW-density functional calculations.[140] Thus, I conclude that dry mica *n*-dopes SLGs, and the intercalated organic layers keep the *n*-doping while the water layer removes it. Mica has a wide band gap of ~ 7.85 eV,[141] its conduction and valance band are too far away from the graphene Fermi level to contribute to the charge transfer. Yet the existence of trap states within the mica band gap has been proposed to explain the thermo-luminescence of mica powders.[142, 143] I presume that similar trap or surface states also exist within the bandgap of mica used in my experiments. And it is reasonable since the periodic crystalline structure of mica was destroyed at the surface after cleavage, this usually introduces surface states at the surface of materials. The spatial position of the trap states should be near the surface, which allows electron tunneling with SLGs. The mica layer thickness is less than nanometers (**Figure 2.4**), which is already within the range of electron tunneling distance. To explain the *n*-doping of SLGs by dry mica, I propose a narrow band of mica trap states filled with electrons lying above the graphene Fermi level (**Figure 5.2.5**). Mica is documented to be an electron-donator in the tribo-electrical series,[144] which can be due to the high energy-filled states located near its surface. Water molecules are proposed to form a self-assembled dipole layer with the "H-down" orientations (**Figure 2.1**).[13, 80, 145] To explain the removal of *n*-doping by intercalation of the water layer, I expect the ordered water molecules with the same orientations produce a large average dipole moment thereby generating a high electric potential. The electric potential offset is large enough to push the mica trap states below the graphene Fermi level, thus undoping graphene consequently (**Figure 5.2.5b**). To explain the restoration of *n*-doping by intercalation of the organic layers, take ethanol as an example, I expect the ethanol molecules take less ordered orientations compared to the water case. This results in a smaller electric potential offset. The small offset is insufficient to shift the mica trap states to a position lower than the graphene Femi level, thus keeping the same charge transfer from mica trap states to graphene as in dry case (**Figure 5.2.5a**).

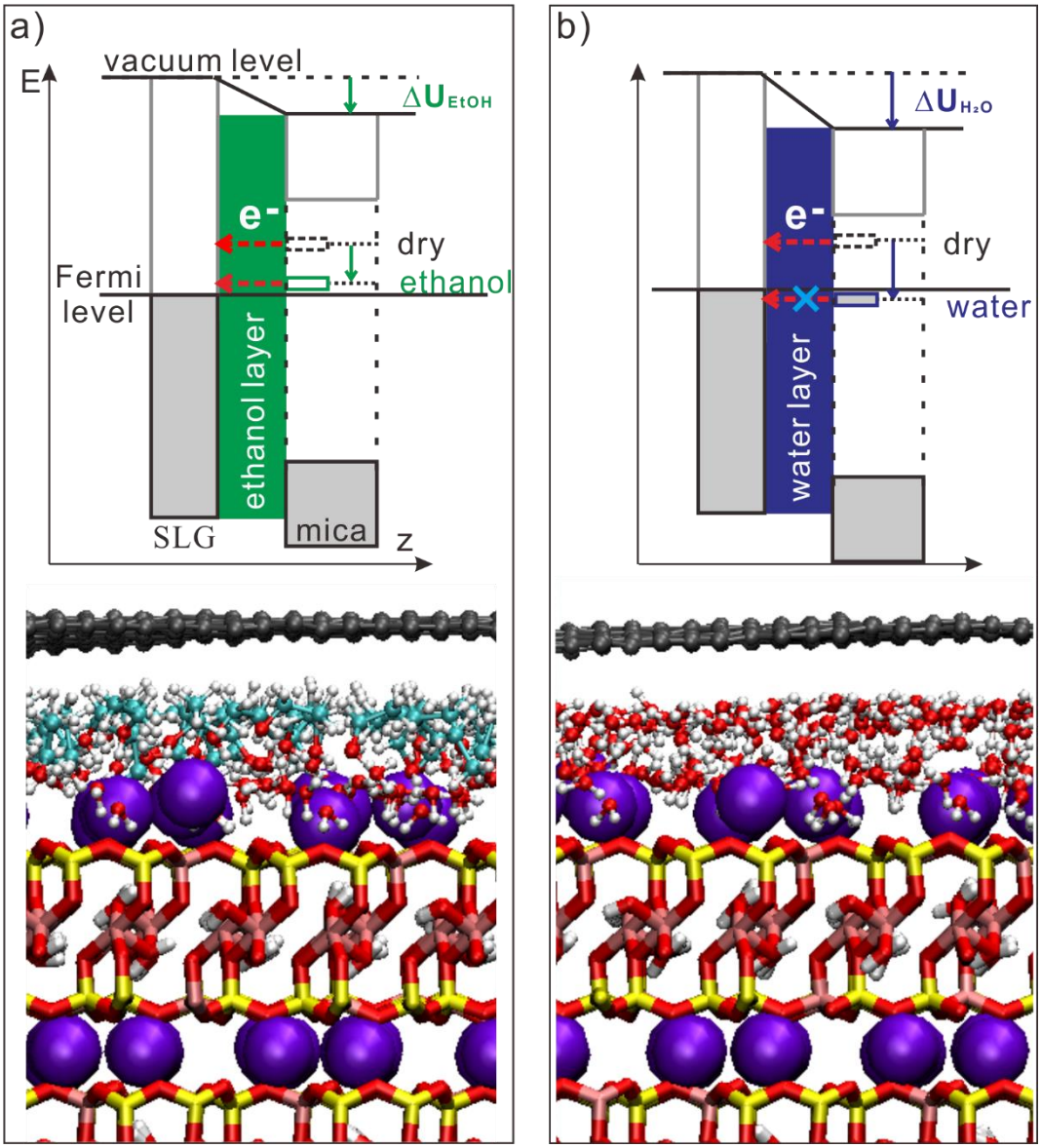

Figure 5.2.5: Tunneling diagrams illustrating my explanation for molecular layers switching charge transfer. Upon dry contact, electrons transfer from the filled mica trap states lying above the graphene Fermi level thus *n*-doping SLG. Electric potentials created by dipole layers of a) ethanol (as well as acetone, 2-proponal) molecules do not push the mica trap states below the graphene Fermi level, thus keeping the *n*-doping. b) The more ordered water layer results in a larger electric potential, pushing the trap states below the graphene Fermi level and removing doping. The structure of the water and ethanol layer is shown below with MD snapshots (adopted from Ref.[36]) after 50 ns of simulations of the graphene-mica interface filled with a) ethanol (mixed with traces of water, see discussion below) and b) water. (Adapted from Ref. [36])

My predictions on the orientation of the confined liquid molecules and the resulting potentials are supported by MD simulations performed by my college *José D. Cojal González* (Figure 5.2.5).[36] The previous computer simulations indicate that

even ppm amounts of water vapor in the glove box can result in a significant amount of water molecules adsorbed onto the freshly cleaved mica surface, thus being confined at the graphene-mica interface after exfoliation of graphene.[146] So the experimentally "dry graphene-mica samples", as I prepared in a glove box with less than 10 ppm water, might already confine traces of water molecules distributed with "H-down" orientations (**Figure 2.1**) in the gap of K^+ ions on the mica surface. Our MD results show that such ordered water molecules at the "dry" interface produce a maximum potential offset of -1.08 ± 0.07 V. Exposure of the "dry" samples to either water or organic vapors introduces another molecular layer residing on the mixture of K^+ ions and native water molecules. The electric potential produced by the intercalated ethanol molecular layers (ΔU_{EtOH}) is calculated to be -0.62 ± 0.11 V, which is even smaller than the one for the "dry" interface. Therefore, the band of mica trap states is still above the graphene Fermi level with intercalation of ethanol layer (**Figure 5.2.5a**). This implies that the intercalating ethanol molecules are substantially less ordered normally to interface compared with the water ones. Less ordering results in smaller electric potential offsets. In contrast, the simulations show that water molecules intercalating into the interface take similar "H-down" orientations to assemble into a highly ordered layer at high RH. This produces a larger potential drop pushing the possibly empty band of mica trap states below the graphene Fermi level. The calculations, based on the height information of the confined water layer (~ 2.8 Å) from SFM imaging, provide a larger potential (ΔU_{H2O} = -1.3 ± 0.1 V) than both "dry" and ethanol cases (**Figure 5.2.5b**). Thus, MD simulations support my model predictions on the charge transfer direction and the magnitude of electronic potentials created by the molecularly liquid layers.

5.2.5 Conclusion

In conclusion, the structural properties of water and ethanol layers confined in graphene-mica slit pore are finally depicted grounded on Raman results and MD simulations. Water molecules fill the slit pore with dipoles pointing down to the mica surface, while ethanol molecules take a less-ordered arrangement. This produces different electric potentials. Given that, I propose a model to interpret the charge transfer at the graphene-mica interface affected by confined molecular layers. I attribute the charge transfer to the relative shift between the band of mica trap states and the graphene Fermi level, which is dominated by structural properties of the confined molecular layers.

The graphene doping induced by the interfacial charge transfer can be used as a remarkable sensor, to detect the structural changes of the nano-confined liquid films. Furthermore, tuning the charge transfer by adsorbed liquid layers at electrode interfaces provides an easy-operated and potential approach to adjust electronic device performances.

5.3 Influence of Molecular Layers on Sliding of Graphene and MoS_2 Single-Layers

5.3.1 Introduction

In addition to doping, strain can also influence the electronic structure of graphene by distorting its crystal structure. It can open the graphene bandgap.[44] Studies on graphene strain are also attractive and important to graphene applications in electronics and tribology.

My previous Raman results show that the confined water and ethanol layer have different influences on charge transfer between graphene and mica. However, both liquid layers drastically reduce the strain in graphene (**Section 5.2, Figure 5.2.2a**). The phenomenon per se is interesting and deserves further investigation. Moreover, there is a lack of kinetic studies on strain changes in graphene upon interface hydration. In this part, I mainly focus on the time evolution of graphene strain affected by the water intercalation. I used SLG sheets as strain sensors to measure strain transfer from mica to graphene through dry and wet interfaces (*i.e.*, the interfaces were intercalated with either water or ethanol layer) by bending of the mica substrate. Additionally, I investigated strain transfer between mica and MoS_2, and how the intercalation of water affects the strain transfer. Strain in SLG and MoS_2 can be identified by changes in Raman and PL spectra, respectively.[89, 147, 148]

I used MoS_2 as a comparison because both graphite and MoS_2 are typical layered materials consisting of 2D sheets. The materials are widely used as solid lubricants due to the slipperiness between the sheets. But their lubrication performances exhibit opposite dependencies on humidity.[149, 150] It is known that graphite fails to lubricate in vacuum.[149] Water vapor in air is necessary for graphite to lubricate efficiently. In contrast, MoS_2 lubricates better in vacuum but worse under ambient humidity. Hence, interfacial water improves lubrication by graphite while it worsens the one by MoS_2. Thus, it is interesting to compare the sliding frictions of graphene and MoS_2 sheets on mica upon hydration of the interface. Their sliding behaviors on mica were inferred from the strain transfer measurements. This might contribute to a better understanding of the mechanisms behind the interfacial friction.

My results imply that the strain relaxation in SLG undergoes a transition from *stick-slip* in dry contact to *viscous* when wetted by water. A faster relaxation is observed with the ethanol intercalation. In contrast, MoS_2 does not relax strain regardless of the interface hydration. This work demonstrates that the slit pore can be employed as a strain sensor for better understanding the impact of the

intercalated liquids on sliding friction in layered materials.

5.3.2 Experimental

Graphenes were exfoliated onto freshly cleaved mica slabs (~ 80-mm-long, ~ 20-mm-wide, and ~ 200-µm-thick) in the glove box with less than 10 ppm of water. The MoS_2-mica samples were prepared in the same way, I used both natural and synthetic MoS_2 purchased from 2D Semiconductor company. The samples were then sealed in a plastic box and transferred to another glove box containing the Raman microscope. This glove box was connected to the environmental control setup (**Figure 4.3a**). The strain transfer experiments were conducted on the samples in dry nitrogen first (~ 2% RH), then in either ethanol vapor or water vapor (RH ~ 24% for MoS_2 and ~ 50% for SLG).

Mica slabs were mounted onto the home-built four-point bending setup (**Figure 4.4**) for strain transfer experiments. The mica slabs were bent in steps to strain their top surfaces to a maximum of ~ 0.2% and then they were unbent subsequently. After each bending/unbending step, the strains in SLGs and single layers of MoS_2 were followed with Raman and PL spectra respectively. There was a delay of a few minutes between bending mica and recording of spectra, since the laser spot had to be manually repositioned again onto the same spot of the samples after each bending step. To determine the peak position scattering caused by displacements of the laser spot on the sample after manual repositioning, the laser was repositioned onto the same spot of the SLG a few times before bending the sample, and spectra were acquired after each time of repositioning. The surface strain of mica ε was estimated according to $\varepsilon = \frac{h}{2R}$ (see **Figure 5.3.0**), where *h* and *R* are the thickness and bending radius of the mica slab respectively.

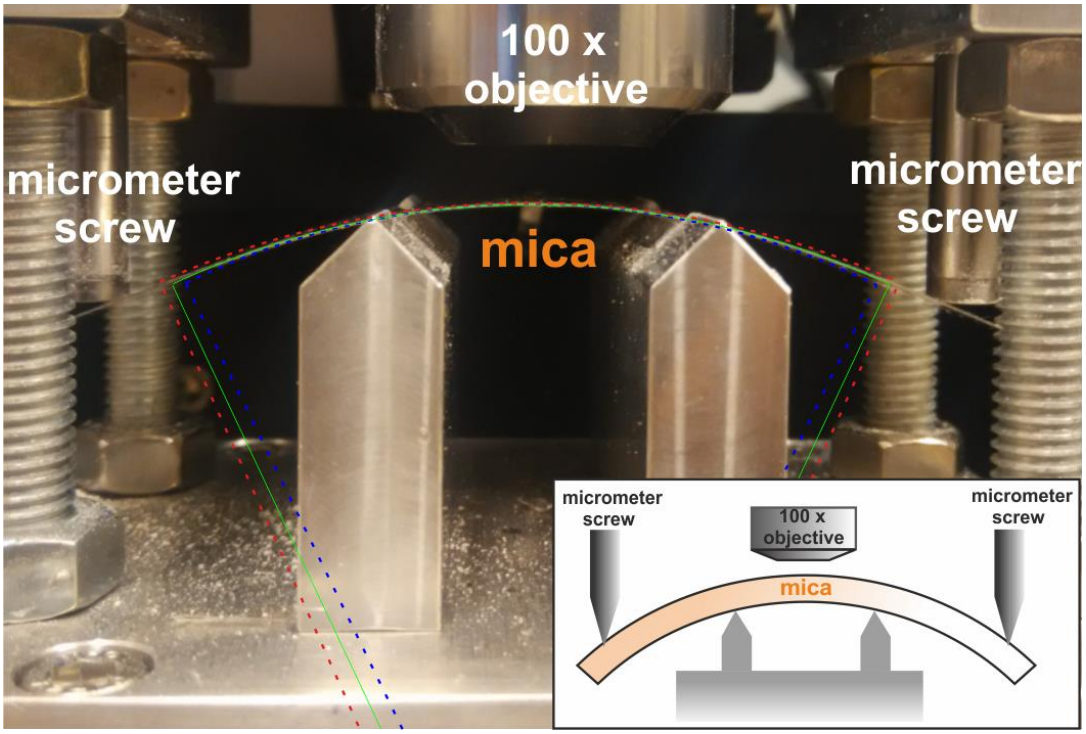

Figure 5.3.0: Photograph of a bent mica slab on the four-point bending setup, inset shows its not-to-scale sketch. The mica slab was bent/unbent in small steps controlled by extension of the two loading pins (micrometer screws). Red, blue dashed and green solid circular segments drawn over the photograph show the upper, lower estimates, and the visually optimal curvatures respectively. The radius *R* of the circles and the thickness of the mica slab *h* are used for strain estimation of its top surface. The upper and lower estimates were used to calculate the surface strain error. (Adapted from Ref. [112])

Raman and PL measurements were performed on SLGs and MoS_2 with 2400 lines/mm and 600 lines/mm gratings respectively. The selected single layers were isolated from multilayer flakes unless stated otherwise. Both Raman and PL spectra were acquired under the 532 nm laser with 1.4 mW and 0.14 mW illumination intensities on the sample surface respectively. The Raman spectrometer was auto-calibrated using a silicon wafer by the Lab Spec 6 software for graphene and MoS_2 samples measured in water vapor. Later, the neon calibration method (as introduced in **Section 5.2**) was employed for graphene samples measured in ethanol vapor. The Raman and PL spectra were fitted with Pseudo-Voigt and Lorentz functions built into the Lab Spec 6 software, respectively.

SFM Imaging of the SLGs and MoS_2 after the strain transfer experiments was performed in tapping mode (Multimode 8, Nanoscope, Bruker).

5.3.3 Results

SFM imaging of water and ethanol intercalating into the graphene-mica slit

pore has been already discussed in **Section 5.1** and **5.2**. Thus, here I skip it and directly show the Raman data. **Figure 5.3.1a** shows typical Raman spectra acquired from an SLG exposed to dry nitrogen then water vapor. As introduced in **Section 3.2.3**, graphene G and 2D are both sensitive to strain, especially 2D peak. The strain transfer experiments were performed before and after hydration of the graphene–mica interface. The peak positions shift along a line with the slope of 2.2 on the ω(2D)/ω(G) graph for both dry and hydrated cases (**Figure 5.3.1d**). This evidences that the peak position changes are governed by strain variations. Similar strain transfer experiments were done on another graphene sample in dry nitrogen and then in ethanol vapor. Its typical Raman spectra are shown in **Figure 5.3.1b**. **Figure 5.3.1e** shows ω(2D)/ω(G) of the SLG during the experiments in both dry and ethanol cases. The 2D and G peak positions, for dry case, spread along the line with the 2.2 slope implying strain to dominate the shift. The 2D and G peak positions for the ethanol case show almost no changes on the same graph. **Figure 5.3.1c** shows PL spectra obtained from a MoS_2 monolayer residing on mica in dry nitrogen and in water vapor. Wetting of the MoS_2-mica interface with a molecular layer of water has been already shown in Ref.[24]. Similar to the graphene case, SFM imaging reveals that water molecules intercalate into the MoS_2-mica slit pore from the MoS_2 edges upon increasing RH to ~ 9%. And a homogeneous monolayer of water is formed in the slit pore at about 15 – 20% RH. The PL spectra of MoS_2 are dominated by two peaks (“A” and “B”), which are related to relaxation behaviors of “A” and “B” excitons due to the energy split from valence band spin-orbital coupling. Both peaks become red-shifted with increasing strain. I used the intense A peak position to follow strain in MoS_2.[147]

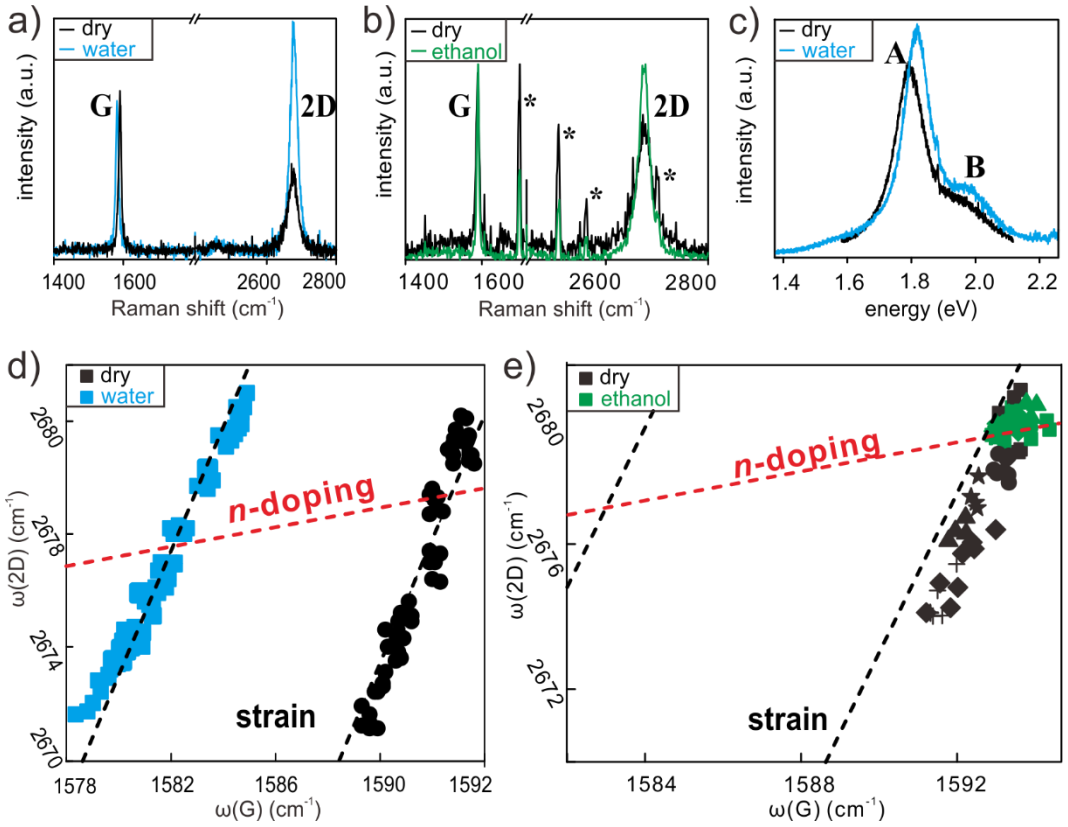

Figure 5.3.1: Raman spectra acquired from: a) an SLG in dry nitrogen (black curve) and water vapor (cyan curve); b) another SLG in dry nitrogen (black curve) and ethanol vapor (green curve). c) PL spectra of MoS_2 acquired in dry nitrogen (black curve) and water vapor (cyan curve). All 2D *versus* G peak positions of the two SLGs recorded during the strain transfer experiments are shown in d) and e). The data acquired in dry are indicated with black symbols. While the data for the water and ethanol case are shown with cyan and green symbols, respectively. The black dashed lines with the slope of 2.2 are expected for strain dominating the peak shifts. The red dashed line of 0.2 slope is for *n*-doping. The offset between black and cyan data points in the water case is attributed to the doping of graphene by mica, and strain dominates the data scattering. Whereas there is no significant doping difference between dry and ethanol cases akin to the previous results (Section 5.2.3). The neon peaks marked with asterisks (*) are used as calibration standards (see detail in Section 5.2.2). (Adapted from Ref. [112])

The 2D peak position downshifts and upshifts with increasing tensile strain and compressive strains respectively (as introduced in Section 3.2.3). Bending increased the tensile strain of the mica slab top surface, while unbending decreased it. Thus one can expect the 2D peak downshifts with bending of mica and upshifts with unbending, provided that the SLG follows the mica surface strain variations. Figure 5.3.2 shows the 2D peak position shifts caused by strain variations in graphene on bent/unbent mica before and after the interface hydration. The mica slab was bent then unbent in steps. Each bending/unbending step increased/decreased tensile strain of the mica top surface with the amount of ~

0.036% (± 0.003%). The vertical arrows in **Figure 5.3.2** indicate the calculated 2D peak shifts expected for the case of graphene following the mica surface strain for each bending/unbending step. Experimentally, at the dry interface, the 2D peak position downshifted as expected in the first two steps of bending (**Figure 5.3.2a**). This indicates that graphene followed the increasing tensile strain of the mica surface at the beginning. However, instead of further downshifting with increasing mica surface strain in the third bending step, the 2D peak upshifted. This implies the strain in the SLG reduced unexpectedly. And in the next three bending steps, the 2D peak downshifted substantially smaller than expected. In steps of unbending, the mica tensile strain decreased, and 2D peak upshifted as expected in the first three steps. But it downshifted slightly upon further releasing mica surface strain. It is noteworthy that the 2D peak positions remained constant in time for a fixed mica surface strain. No 2D change with time is found within each bending/unbending step.

For the water-wetted interface, an increase of mica surface tensile strain caused a downshift of the 2D peak. Then, the 2D peak upshifted slowly over time (**Figure 5.3.2b**), while the mica surface strain was kept constant. The 2D peak *versus* time dependencies could be well fitted with an exponential decay function. The exponential decay function is commonly used in analyzing viscous relaxations. The data imply that the SLG was first strained along with the strained mica, then gradually relaxed its strain in the presence of the confined water layer. Similar behavior also showed up when releasing mica surface strain. After the strain transfer experiments, the SFM imaging showed a flat SLG flake (**Figure 5.3.2b, inset**).

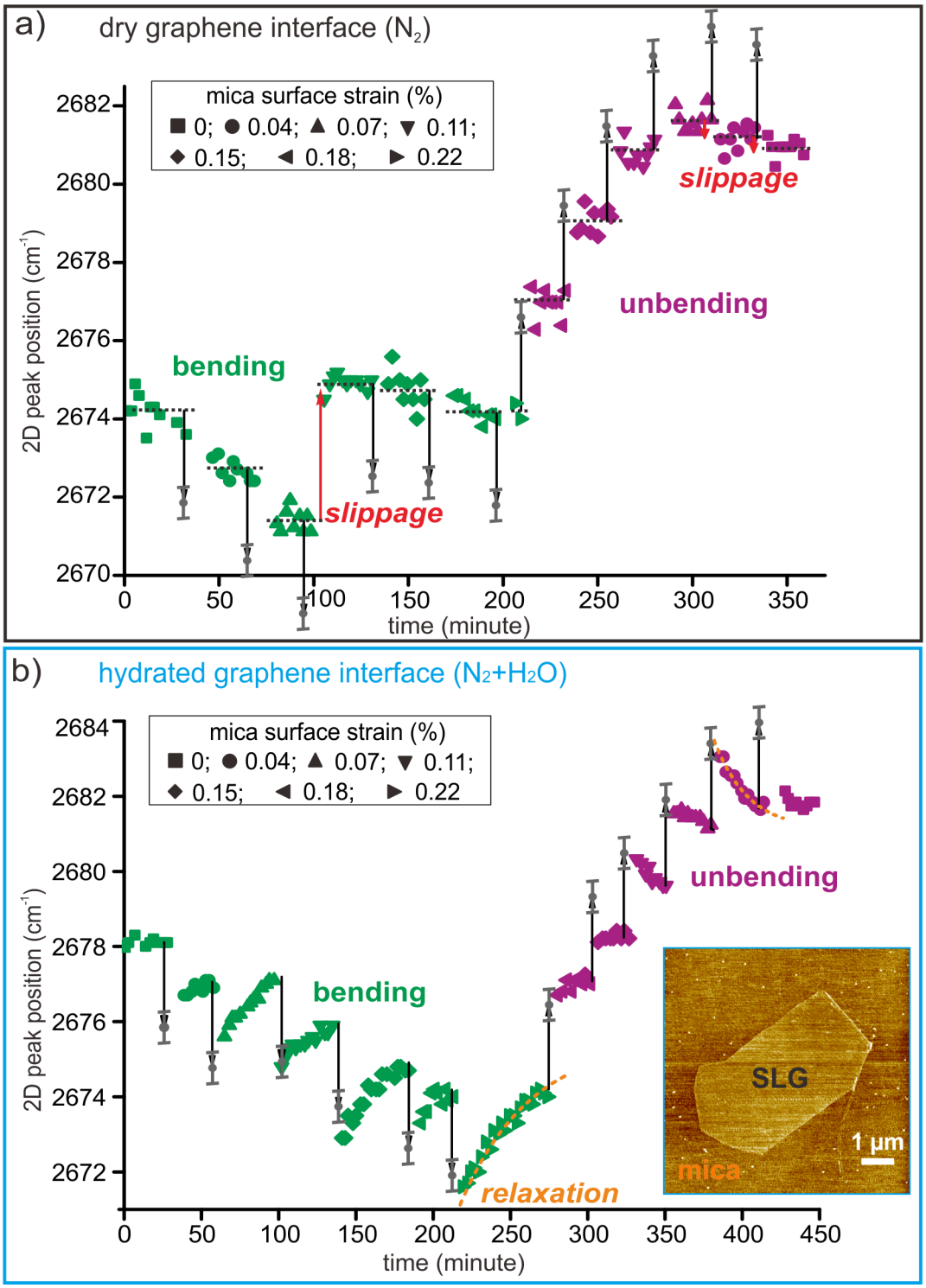

Figure 5.3.2: 2D peak position dependencies on time for an SLG with a) dry and b) hydrated interfaces. The 2D peak positions recorded for different steps of mica bending and unbending are noted with different shapes of green and purple symbols. The expected shifts for graphene strain matching the surface strain steps of mica are indicated with vertical arrows, assuming $\Delta\omega(2D)/\Delta\varepsilon = 64$ cm^{-1}/%.[89] The error bars show the errors of mica surface strain estimation. The dashed orange lines in b) exemplify exponential fits of the data with relaxation times on the order of 10 minutes. The inset shows the SFM height image of the

SLG after the Raman measurements. The SLG was strained roughly along the horizontal direction. (Adapted from Ref. [112])

The similar strain experiments were performed on another graphene sample in dry nitrogen first and then in ethanol vapor. Figure 5.3.3 shows how the 2D peak position shifted with the bending/unbending of mica in both cases. The 2D peak in dry case shifted in a way similar to the previous sample, *i.e.*, 2D peak downshifted as expected in the first three steps of bending mica and kept constant over time, but upshifts unexpectedly in the 4th bending step. At the ethanol-wetted interface, no significant changes of the 2D peak could be detected in each strain step. The SLG was also flat after Raman measurements (Figure 5.3.3, inset).

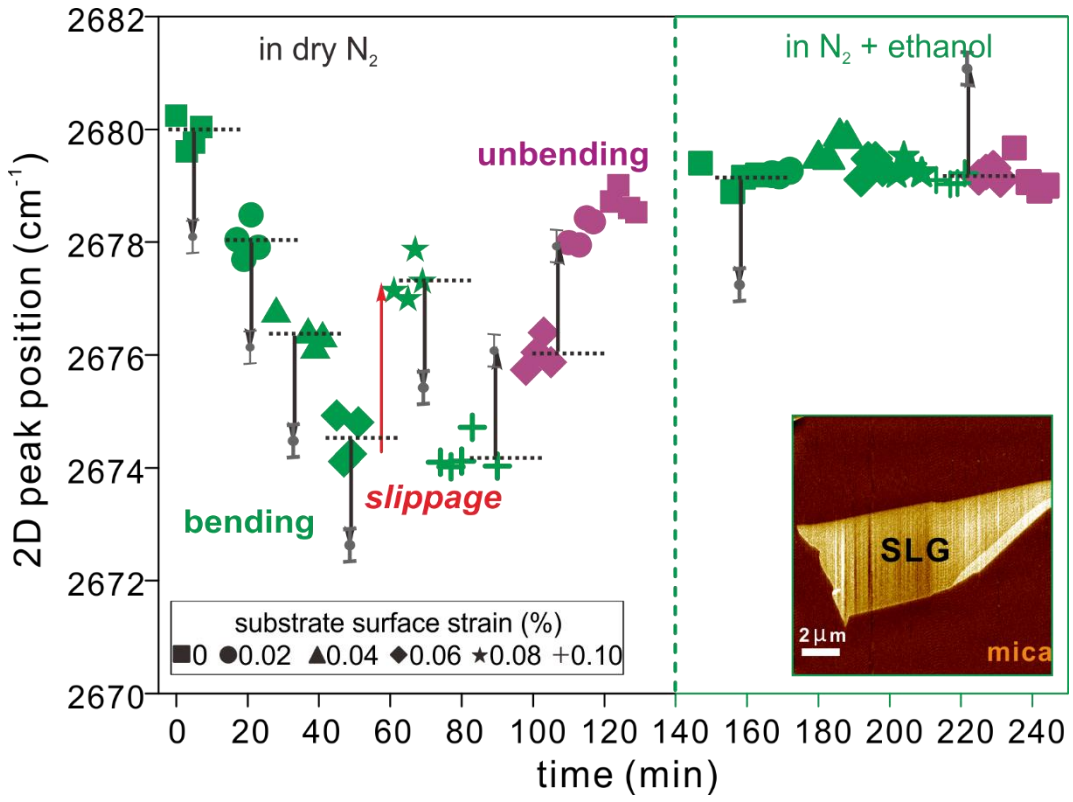

Figure 5.3.3: 2D peak position dependencies on time for an SLG with dry and ethanol-wetted interfaces. The color coding and symbol styles are similar to those used in Figure 5.3.2. The inset shows the SFM height image of the SLG after Raman measurements. The sample was strained roughly along the horizontal direction.

MoS_2 PL A peak position recorded on bent/unbent mica substrate is shown in Figure 5.3.4. The MoS_2 sample was bent/unbent in just one step for a few cycles. At the dry interface, the PL A peak red-shifted with bending, while returned back after releasing bending. And its position remained constant in time after bending. Interface hydration blue-shifted the PL A peak significantly. The PL A peak further blue-shifted with the mica strain cycles, *i.e.*, bending of mica did not shift the peak while unbending blue-shifted it. After a few mica strain cycles, the peak position

blue-shifted to the expected peak position for unstrained MoS_2.[147] Then the peak position started to oscillate with surface strain cycles similarly to the dry case. The SFM height image of the MoS_2 after the strain transfer experiments shows that the MoS_2 flake exhibits fractures and wrinkles.

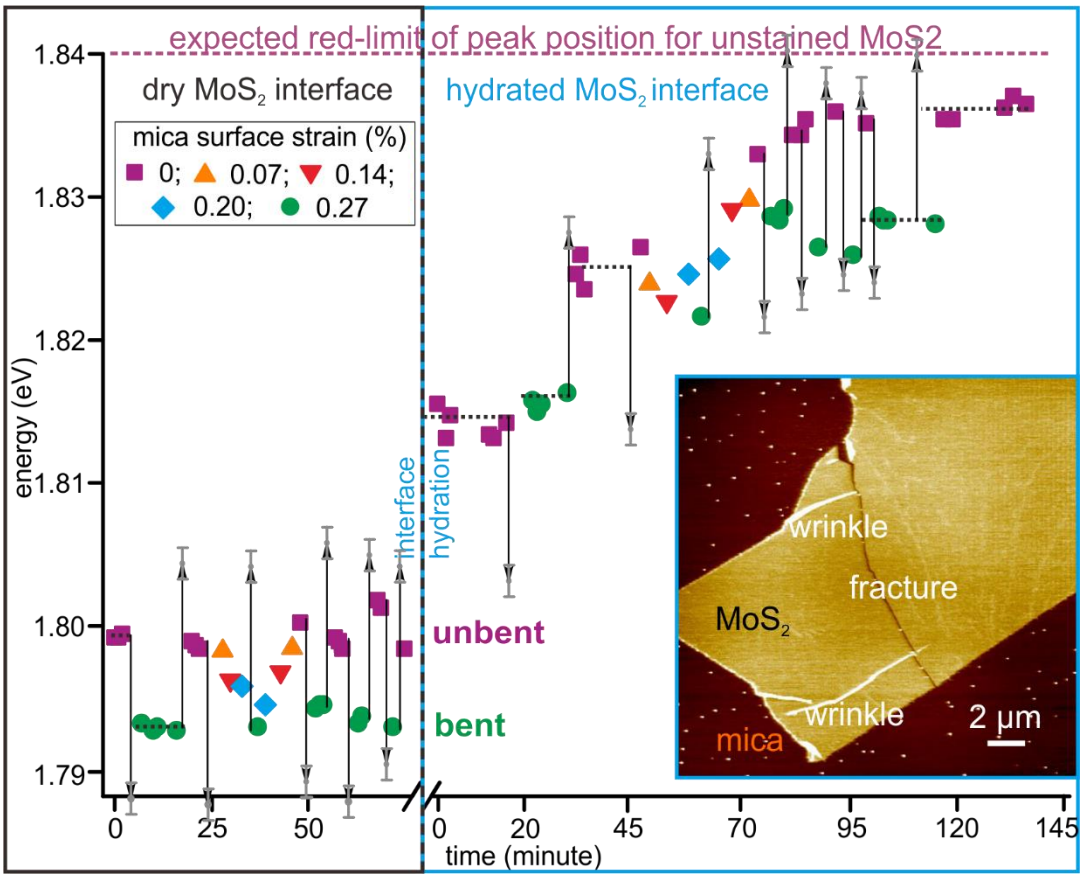

Figure 5.3.4: PL A peak position dependencies on time for a MoS_2 flake with dry and hydrated interfaces. Repeated bending/unbending of the mica cycled its surface strain with $\Delta\varepsilon$ = 0.27 ± 0.03%. The expected PL A peak position shifts for MoS_2 following the mica surface strain are shown with the arrows, assuming $\Delta E_A/\Delta\varepsilon$ = 45 meV/%.[151, 152] The error bars show the errors of mica surface strain estimation. The inset is the SFM height image of the MoS_2 flake. The sample was strained roughly along the horizontal direction. (Adopted from Ref. [112])

5.3.4 Discussion

The data acquired from the dry SLGs imply that the SLG flake first was stuck to the mica, thus its strain followed the mica surface strain when starting the bending process. However, the elastic restoration force increased with the stepwise increase of strain in the flake, and led to a slippage of the flake on the mica surface when the restoration force exceeded the frictional force at the interface. After the slippage, the frictional force at the interface reduced as the 2D peak position shifted much less in the following strain steps (**Figure 5.3.2a**). Such behavior is reminiscent

of a "stick-slip" macroscopic dry friction. In contrast, water layer intercalation modified the strain relaxation behavior. The SLG flake became strained after each bending/unbending step of mica, following the strained mica. On the other hand, the strain in the flake then relaxed viscously due to the lubricating effect of the water layer (**Figure 5.3.2b**). The flake remaining flat after strain tests also supports the conclusion of strain relaxation. SFM studies have shown that ethanol molecules can also intercalate into the graphene-mica interface.[128, 129] And my Raman results in **Section 5.2** also prove this indirectly. The strain in SLG on a dry mica was almost completely removed after the formation of an ethanol layer at the interface. This is similar to the water case, where strain in SLG on the flat mica mostly disappeared after water intercalation (**Figure 5.1.3**). However, I do not observe any 2D shift with mica being strained in ethanol vapor. This implies that the strain in the SLG relaxed too fast to be experimentally measured. The SFM images show that the two graphene samples have comparable size along their strain directions, and remained flat and clean after the strain transfer experiments in both water and ethanol vapor. This qualitatively supports the faster strain relaxation of graphene on top of the ethanol layer than that on top of the water layer.

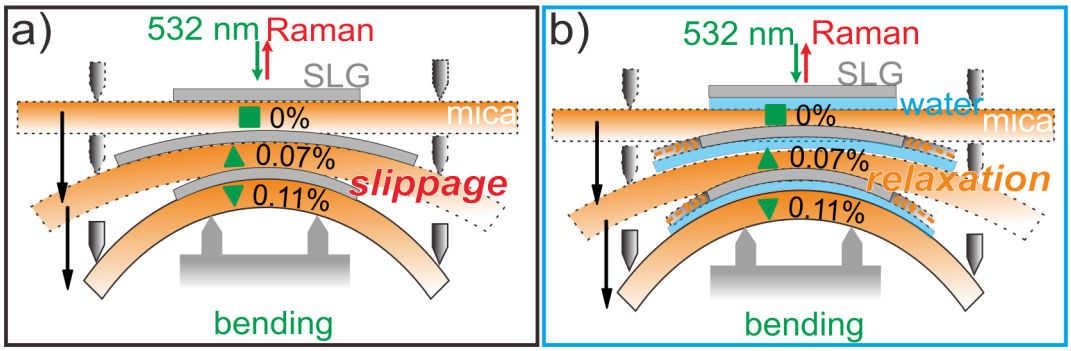

Figure 5.3.5: Sketches of a) "stick-slip" event at the dry and b) viscous relaxation at the hydrated graphene-mica interface (not-to-scale). In dry, the SLG was strained together with mica surface strain (up to ~ 0.07%). This caused downshifts of 2D peak and increasements of elastic restoration force in the SLG with bending steps of mica. Further increasing the elastic restoration force exceeded the frictional force at the interface, resulting in slippage of the SLG flake and upshifts of the 2D peak. After hydration, a water layer lubricated the interface. The SLG was first strained with bending mica, and then relaxed its strain over time. As a consequence, the 2D peak first downshifted with bending then upshifted with time. (Adapted from Ref. [112])

Strain is expected to red-shift the PL A peak, while dielectric screening by substrates or environments blue-shifts it.[147, 153, 154] Doping influences significantly the shape and intensity of the PL A peak, and position shifts of the A peak by doping are mainly caused by its shape changes.[155, 156] The red-limit position for unstrained MoS_2 is reported to be ~ 1.84 eV.[147] Thus my MoS_2 flake was possibly strained by the dry mica surface. Bending of mica increased the strain in the MoS_2 flake while unbending

reduced it. Yet the poor strain resolution for MoS_2 made it difficult to distinguish the *stick-slip* behavior like it was done for the graphene samples. Moreover, the $\Delta E_A/\Delta\varepsilon$ = 45 meV/% is not consistent among literature,[147, 151, 152, 157] thereby not allowing a precise estimation for the expected shift for MoS_2 matching the mica surface strain. Nevertheless, I reiterate that there was no strain relaxation over time for both dry and hydrated MoS_2 as the PL A peak position always remained constant in time for every strain step. This suggests that the frictional force at the MoS_2-mica interface is also solid-like. After hydration, a water layer intercalated into the interface. The large PL A peak blue-shift prior to strain tests was induced possibly by doping change or dielectric screening of the water intercalation. The further blue-shift with mica strain cycles, implying the stepwise reduction of strain, may be attributed to the progressive formation of fractures and wrinkles found in the hydrated MoS_2 flake (**Figure 5.3.4, inset**).[158] In contrast, similar fractures and wrinkles were not observed in MoS_2 samples strained in dry nitrogen.[112] After the reduction of strain with mica strain cycles, the hydrated flake started following the mica surface strain variations just like the dry case. This implies the intercalated water layer pinned the MoS_2 flake to the mica surface, which also supports the conclusion of solid-like friction at the hydrated interface.

In general, the influences of the intercalated water layer on strain relaxation in the SLG and MoS_2 flake match the effects of the adsorbed water layer on bulk graphite and MoS_2 material frictions as introduced in **Section 5.3.1**, *i.e.*, the presence of water allows sliding of graphene but pinning of MoS_2. Moreover, it suggests that the sliding or pinning of the 2D materials is determined by the property of the hydrated interfaces, rather than by the properties of the water layer itself.

In the following, I will estimate the dry frictional force at the dry graphene-mica interface and the viscous friction coefficient for the water case. The original theoretical calculations were conducted by Prof. *Igor M. Sokolov* and the details were published in Ref.[112]. The dry frictional force is estimated based on its balance with the elastic restoration force in SLG:[158, 159]

$$f = \frac{E\Delta\varepsilon h}{L} \tag{5.3}$$

where, $E \approx 1Tpa$ is the elastic modulus of graphene,[160] $\Delta\varepsilon = 0.17\%$ is the maximum strain difference, calculated from $(\omega(2D)_{max}\text{-}\omega(2D)_{min})/(64\ cm^{-1}/\%)$,[89] $h = 0.34\ nm$ is the thickness[161] and $L \approx 5\ \mu m$ is the length of the SLG, estimated from its SFM image (**Figure 5.3.2, inset**). Hence, the dry frictional force per area $f \approx 100\ kPa$. This result is an upper limit for the interfacial friction. Because the estimation was based on a few assumptions to facilitate the calculations, *e.g.*, the geometry of the SLG flake was assumed to be rectangular, and the flake was strained along one side. In addition, graphene edges might also contribute to friction,

but they were hardly taken into account. Thus such possible contributions were neglected. All these assumptions render the final result to be overestimated. For the hydrated interface, exponential decay of strain relaxation in the SLG is expected based on the assumption of viscous friction at the hydrated interface. From this, The viscous strain relaxation is calculated using the equation:[112]

$$\varepsilon(t) \propto \exp\left(-\frac{Eh\pi^2}{\alpha L^2}t\right) = e^{-\frac{t}{\tau}}$$

where, α is the viscous friction coefficient in units of force per unit area and per unit velocity, τ is the relaxation time. The τ is on the order of ~ 10 minutes, which is averaged from the exponential decay fits of the 2D peak shifts in bending/unbending steps (see examples in **Figure 5.3.2**). Taking the height of the water layer (~ 2.8 Å) into account, the efficient shear viscosity of the water layer is calculated to be 10^{10} m*Pa*s. This is 10 orders of magnitude higher than the bulk water viscosity. In terms of the ethanol-wetted interface, the strain relaxation occurred too fast to be detected. This indicates that the molecularly thin ethanol layer possesses a better lubricity than the water one, *i.e.*, over one order of magnitude more lubricant, since the strain fully relaxed within less than one minute.

To the best of my knowledge, there are a few possible mechanisms for the interfacial friction differences caused by the intercalation of liquid molecules. For instance, the water layer was proposed to increase the density of flexural phonons in graphene, facilitating the energy transfer between graphene and mica substrate.[35] This might cause higher interfacial friction compared to the dry interface. In addition, the resonance among flexural phonons of graphene, mica, and the intercalations is also in favor of energy dissipation, thus contributing to the friction differences as well. A better understanding of the mechanisms requires more experimental investigations. The 2D material-mica system and the bending method used in this work provide a way to achieve it.

5.3.5 Conclusion

The Raman spectroscopy allows investigating the impacts of the confined molecular layers on interfacial frictional forces by probing strain relaxations in SLG and MoS_2 flakes resting on the mica surface. The intercalated water layer changes *stick-slip* dry friction to *viscous* friction at the graphene-mica interface. The intercalated ethanol layer possesses a better lubricity than water. In contrast, a water layer pins MoS_2 to the mica surface, leading to structural failures in MoS_2 during the strain transfer experiments. The graphene-mica slit pore is proved to be an extremely sensitive tool to probe the strain evolutions in graphene with the intercalated molecules. This system can be used as a strain sensor to study the influence of adsorbed liquids on interfacial friction.

6. Summary and Outlook

This work mainly investigated the influences of the confined water layers, as well as organic solvent layers on the electronic (doping) and mechanical properties (strain) of SLG with mica as a substrate. The tape-free mechanical exfoliation method was used to prepare clean and flat graphene-mica samples. The samples were measured in a well-controlled nitrogen-based gas atmosphere to avoid airborne absorbates on the sample surface. *In situ* SFM and Raman spectroscopy were employed to get insight into the wetting process of liquid molecules in the slit pore, and their influences on the interfacial charge transfer and friction.

SFM imaging revealed that water molecules intercalated into the dry graphene-mica slit pore upon exposing samples to humid nitrogen, and finally formed a molecularly thin layer. The Raman results unraveled the doping and strain changes of graphene with the intercalation of a water layer and an ethanol layer. I find that graphene exfoliated on dry mica surface is *n*-doped with an averaged charge concentration of $(0.45 \pm 0.02) \times 10^{13}$ e^-/cm^2. The water molecular layer blocks the charge transfer from dry mica to graphene, while the ethanol layer allows it. Furthermore, a dry frictional force per area of 100 kPa between graphene and mica is found through the strain transfer measurement. Both water and ethanol liquids confined in the slit pore cause strain relaxation in graphene. The water layer changes the solid friction at the dry interface to viscous friction. A better lubricity of ethanol is found compared to water. In contrast, no lubricating effect of water was observed at the interface between mica and another 2D material MoS_2. This suggests that the lubricating properties are determined by the interfaces, rather than the confined liquid layers. MD simulations and theoretical calculations together with the experimental results allowed obtaining a deeper insight into the structural properties of the molecular layers in the slit pore. Water molecules intercalate into the slit pore with the dipole direction pointing down to the mica surface. Some of them possibly fill into the gaps between K^+ ions and are bound to mica surface via hydrogen bonding, while others form a molecularly thin layer on top and exhibit fluid-like properties. Ethanol molecules are less ordered. The different dipole moment of the water and the ethanol layer produces different electrostatic potential offsets, which dominate the charge transfer at the graphene-mica interface.

This work demonstrates that the graphene-mica system is a versatile tool, which can be used to not only study the interfacial charge transfer but also to investigate the interfacial friction. As a prospect, this system can be used to study other 2D materials, not only graphene. For example, using PL spectroscopy to probe the electronic properties of MoS_2 and WS_2, to gain further understanding of dielectric screening effects of the interfacial molecular layers, charge transfer mechanism and contact electrification. It is also noteworthy to clarify which components in the ambient condition adsorbed on graphene surface and doped it,

this contributes to understanding the doping mechanism of graphene by surrounding. All these are practically important for graphene applications in electronics. Furthermore, it can also envision investigating the influence of local strains in 2D materials on their electronic properties with the slit pore system. For example, wetting and dewetting of the graphene-mica slit pore shows labyrinthine nanostructure and fractal depressions, thus deforming the graphene flake and introducing local strains around the boundaries of the wetting area and fractals. It is interesting to investigate how the electronic properties of graphene change with the local strains induced by the nanostructures using high-resolution Raman imaging techniques like tip-enhanced Raman spectroscopy. Furthermore, the strain transfer measurements with heavy water (D_2O) as intercalations in the graphene-mica interface are in progress. As an isotopic molecule of water, heavy water and water have very similar properties. Therefore, I expect the D_2O molecules can also intercalate into the interface and forms a molecular layer like water. However, since they have different isotopic compositions, *i.e.*, the atomic mass of deuterium is double that of hydrogen, this causes different vibrational frequencies of their molecular bonds. The different vibrational frequencies will result in different collision rates with the graphene, thus different frictions at the interface are expected. Using graphene as the sensitive strain sensor, the friction differences between water and heavy water cases can be quantitively determined. And this will contribute to better understanding of the friction mechanisms at the interface.

7. References

1. Novoselov, K. S.; Geim, A. K.; Morozov, S. V.; Jiang, D.; Zhang, Y.; Dubonos, S. V.; Grigorieva, I. V.; Firsov, A. A., Electric Field Effect in Atomically Thin Carbon Films. *Science* **2004,** *306*, 666-9.

2. Geim, A. K.; Novoselov, K. S., The Rise of Graphene. *Nat. Mater.* **2007,** *6*, 183-191.

3. Melios, C.; Giusca, C. E.; Panchal, V.; Kazakova, O., Water on Graphene: Review of Recent Progress. *2D Materials* **2018,** *5*, 022001.

4. Granick, S., Motions and Relaxations of Confined Liquids. *Science* **1991,** *253*, 1374-9.

5. Finney, J. L., Overview Lecture. Hydration Processes in Biological and Macromolecular Systems. *Faraday Discuss.* **1996,** *103*, 1-18.

6. Holt, J. K.; Park, H. G.; Wang, Y.; Stadermann, M.; Artyukhin, A. B.; Grigoropoulos, C. P.; Noy, A.; Bakajin, O., Fast Mass Transport through Sub-2-Nanometer Carbon Nanotubes. *Science* **2006,** *312*, 1034-7.

7. Bocquet, L.; Charlaix, E., Nanofluidics, from Bulk to Interfaces. *Chem. Soc. Rev.* **2010,** *39*, 1073-95.

8. Li, Q.; Song, J.; Besenbacher, F.; Dong, M., Two-Dimensional Material Confined Water. *Acc. Chem. Res.* **2015,** *48*, 119-27.

9. Nair, R. R.; Wu, H. A.; Jayaram, P. N.; Grigorieva, I. V.; Geim, A. K., Unimpeded Permeation of Water through Helium-Leak-Tight Graphene-Based Membranes. *Science* **2012,** *335*, 442-4.

10. Maier, S.; Salmeron, M., Adsorption of Water. In *Surface and Interface Science*, **2016**; pp 357-390.

11. Thiel, P. A.; Madey, T. E., The Interaction of Water with Solid Surfaces: Fundamental Aspects. *Surf. Sci. Rep.* **1987,** *7*, 211-385.

12. Ranea, V. A.; Michaelides, A.; Ramirez, R.; de Andres, P. L.; Verges, J. A.; King, D. A., Water Dimer Diffusion on Pd[111] Assisted by an H-Bond Donor-Acceptor Tunneling Exchange. *Phys. Rev. Lett.* **2004,** *92*, 136104.

13. Verdaguer, A.; Sacha, G. M.; Bluhm, H.; Salmeron, M., Molecular Structure of Water at Interfaces: Wetting at the Nanometer Scale. *Chem. Rev.* **2006,** *106*, 1478-510.

14. Michaelides, A., Density Functional Theory Simulations of Water–Metal Interfaces: Waltzing Waters, a Novel 2d Ice Phase, and More. *Appl. Phys. A* **2006,** *85*, 415-425.

15. Xu, K.; Cao, P.; Heath, J. R., Graphene Visualizes the First Water Adlayers on Mica at Ambient Conditions. *Science* **2010,** *329*, 1188-91.

16. Cao, P.; Xu, K.; Varghese, J. O.; Heath, J. R., The Microscopic Structure of Adsorbed Water on Hydrophobic Surfaces under Ambient Conditions. *Nano Lett.* **2011,** *11*, 5581-6.

17. Severin, N.; Lange, P.; Sokolov, I. M.; Rabe, J. P., Reversible Dewetting of a Molecularly Thin Fluid Water Film in a Soft Graphene-Mica Slit Pore. *Nano Lett.* **2012,** *12*, 774-9.

18. Shim, J.; Lui, C. H.; Ko, T. Y.; Yu, Y. J.; Kim, P.; Heinz, T. F.; Ryu, S., Water-Gated Charge Doping of Graphene Induced by Mica Substrates. *Nano Lett.* **2012,** *12*, 648-54.

19. Lee, M. J.; Choi, J. S.; Kim, J.-S.; Byun, I.-S.; Lee, D. H.; Ryu, S.; Lee, C.; Park, B. H., Characteristics and Effects of Diffused Water between Graphene and a Sio_2 Substrate. *Nano Res.* **2012,** *5*, 710-717.

20. Song, J.; Li, Q.; Wang, X.; Li, J.; Zhang, S.; Kjems, J.; Besenbacher, F.; Dong, M., Evidence of Stranski-Krastanov Growth at the Initial Stage of Atmospheric Water Condensation. *Nat. Commun.* **2014,** *5*, 4837.

21. Ochedowski, O.; Bussmann, B. K.; Schleberger, M., Graphene on Mica - Intercalated Water Trapped for Life. *Sci. Rep.* **2014,** *4*, 6003.

22. Bampoulis, P.; Siekman, M. H.; Kooij, E. S.; Lohse, D.; Zandvliet, H. J.; Poelsema, B., Latent Heat Induced Rotation Limited Aggregation in 2d Ice Nanocrystals. *J. Chem. Phys.* **2015,** *143*, 034702.

23. Lin, H.; Schilo, A.; Kamoka, A. R.; Severin, N.; Sokolov, I. M.; Rabe, J. P., Insight into the Wetting of a Graphene-Mica Slit Pore with a Monolayer of Water. *Phys. Rev. B* **2017,** *95*, 195414.

24. Rauf, A.; Schilo, A.; Severin, N.; Sokolov, I. M.; Rabe, J. P., Non-Monotonous Wetting of Graphene-Mica and Mos2-Mica Interfaces with a Molecular Layer of Water. *Langmuir* **2018,** *34*, 15228-15237.

25. Lee, C.; Wei, X.; Kysar, J. W.; Hone, J., Measurement of the Elastic Properties and Intrinsic Strength of Monolayer Graphene. *Science* **2008,** *321*, 385-8.

26. Bunch, J. S.; Verbridge, S. S.; Alden, J. S.; van der Zande, A. M.; Parpia, J. M.;

Craighead, H. G.; McEuen, P. L., Impermeable Atomic Membranes from Graphene Sheets. *Nano Lett.* **2008,** *8*, 2458-62.

27. Lange, P.; Dorn, M.; Severin, N.; Vanden Bout, D. A.; Rabe, J. P., Single- and Double-Layer Graphenes as Ultrabarriers for Fluorescent Polymer Films. *J. Phys. Chem. C* **2011,** *115*, 23057-23061.

28. Zhu, Y.; Granick, S., Viscosity of Interfacial Water. *Phys. Rev. Lett.* **2001,** *87*, 096104.

29. Christenson, H. K.; Thomson, N. H., The Nature of the Air-Cleaved Mica Surface. *Surf. Sci. Rep.* **2016,** *71*, 367-390.

30. Severin, N.; Gienger, J.; Scenev, V.; Lange, P.; Sokolov, I. M.; Rabe, J. P., Nanophase Separation in Monomolecularly Thin Water-Ethanol Films Controlled by Graphene. *Nano Lett.* **2015,** *15*, 1171-6.

31. Bampoulis, P.; Witteveen, J. P.; Kooij, E. S.; Lohse, D.; Poelsema, B.; Zandvliet, H. J., Structure and Dynamics of Confined Alcohol-Water Mixtures. *ACS Nano* **2016,** *10*, 6762-8.

32. Kuhs, W. F.; Lehmann, M. S., The Structure of Ice-I_h. In *Water Science Reviews 2*, Franks, F., Ed. Cambridge University Press: Cambridge, **1986**; Vol. 2, pp 1-66.

33. He, K. T.; Wood, J. D.; Doidge, G. P.; Pop, E.; Lyding, J. W., Scanning Tunneling Microscopy Study and Nanomanipulation of Graphene-Coated Water on Mica. *Nano Lett.* **2012,** *12*, 2665-72.

34. Bollmann, T. R. J.; Antipina, L. Y.; Temmen, M.; Reichling, M.; Sorokin, P. B., Hole-Doping of Mechanically Exfoliated Graphene by Confined Hydration Layers. *Nano Res.* **2015,** *8*, 3020-3026.

35. Lee, H.; Ko, J. H.; Choi, J. S.; Hwang, J. H.; Kim, Y. H.; Salmeron, M.; Park, J. Y., Enhancement of Friction by Water Intercalated between Graphene and Mica. *J. Phys. Chem. Lett.* **2017,** *8*, 3482-3487.

36. Lin, H.; Cojal Gonzalez, J. D.; Severin, N.; Sokolov, I. M.; Rabe, J. P., Reversible Switching of Charge Transfer at the Graphene-Mica Interface with Intercalating Molecules. *ACS Nano* **2020,** *14*, 11594-11604.

37. Lafkioti, M.; Krauss, B.; Lohmann, T.; Zschieschang, U.; Klauk, H.; Klitzing, K. V.; Smet, J. H., Graphene on a Hydrophobic Substrate: Doping Reduction and Hysteresis Suppression under Ambient Conditions. *Nano Lett.* **2010,** *10*, 1149-53.

38. Zhou, S. Y.; Gweon, G. H.; Fedorov, A. V.; First, P. N.; de Heer, W. A.; Lee, D. H.;

Guinea, F.; Castro Neto, A. H.; Lanzara, A., Substrate-Induced Bandgap Opening in Epitaxial Graphene. *Nat. Mater.* **2007,** *6*, 770-5.

39. Ryu, S.; Liu, L.; Berciaud, S.; Yu, Y. J.; Liu, H.; Kim, P.; Flynn, G. W.; Brus, L. E., Atmospheric Oxygen Binding and Hole Doping in Deformed Graphene on a Sio(2) Substrate. *Nano Lett.* **2010,** *10*, 4944-51.

40. Wehling, T. O.; Lichtenstein, A. I.; Katsnelson, M. I., First-Principles Studies of Water Adsorption on Graphene: The Role of the Substrate. *Appl. Phys. Lett.* **2008,** *93*, 202110.

41. Decker, R.; Wang, Y.; Brar, V. W.; Regan, W.; Tsai, H. Z.; Wu, Q.; Gannett, W.; Zettl, A.; Crommie, M. F., Local Electronic Properties of Graphene on a Bn Substrate Via Scanning Tunneling Microscopy. *Nano Lett.* **2011,** *11*, 2291-5.

42. Lee, D.; Ahn, G.; Ryu, S., Two-Dimensional Water Diffusion at a Graphene-Silica Interface. *J. Am. Chem. Soc.* **2014,** *136*, 6634-42.

43. Cao, P.; Varghese, J. O.; Xu, K.; Heath, J. R., Visualizing Local Doping Effects of Individual Water Clusters on Gold(111)-Supported Graphene. *Nano Lett.* **2012,** *12*, 1459-63.

44. Gui, G.; Li, J.; Zhong, J., Band Structure Engineering of Graphene by Strain: First-Principles Calculations. *Phys. Rev. B* **2008,** *78*, 075435.

45. Pereira, V. M.; Castro Neto, A. H., Strain Engineering of Graphene's Electronic Structure. *Phys. Rev. Lett.* **2009,** *103*, 046801.

46. Guo, B.; Fang, L.; Zhang, B.; Gong, J. R., Graphene Doping: A Review. *Insciences J.* **2011,** *1*, 80-89.

47. Kitt, A. L.; Qi, Z.; Remi, S.; Park, H. S.; Swan, A. K.; Goldberg, B. B., How Graphene Slides: Measurement and Theory of Strain-Dependent Frictional Forces between Graphene and Sio2. *Nano Lett.* **2013,** *13*, 2605-10.

48. Koga, K.; Gao, G. T.; Tanaka, H.; Zeng, X. C., Formation of Ordered Ice Nanotubes inside Carbon Nanotubes. *Nature* **2001,** *412*, 802-5.

49. Beckstein, O.; Sansom, M. S., Liquid-Vapor Oscillations of Water in Hydrophobic Nanopores. *Proc. Natl. Acad. Sci. U.S.A.* **2003,** *100*, 7063-8.

50. Majumder, M.; Chopra, N.; Andrews, R.; Hinds, B. J., Nanoscale Hydrodynamics: Enhanced Flow in Carbon Nanotubes. *Nature* **2005,** *438*, 44.

51. Secchi, E.; Marbach, S.; Nigues, A.; Stein, D.; Siria, A.; Bocquet, L., Massive Radius-

Dependent Flow Slippage in Carbon Nanotubes. *Nature* **2016,** *537*, 210-3.

52. Hodgson, A.; Haq, S., Water Adsorption and the Wetting of Metal Surfaces. *Surf. Sci. Rep.* **2009,** *64*, 381-451.

53. Izvekov, S.; Voth, G. A., Ab Initiomolecular Dynamics Simulation of the Ag(111)-Water Interface. *J. Chem. Phys.* **2001,** *115*, 7196-7206.

54. Michaelides, A.; Ranea, V. A.; de Andres, P. L.; King, D. A., General Model for Water Monomer Adsorption on Close-Packed Transition and Noble Metal Surfaces. *Phys. Rev. Lett.* **2003,** *90*, 216102.

55. Motobayashi, K.; Matsumoto, C.; Kim, Y.; Kawai, M., Vibrational Study of Water Dimers on Pt(111) Using a Scanning Tunneling Microscope. *Surf. Sci.* **2008,** *602*, 3136-3139.

56. Carrasco, J.; Michaelides, A.; Forster, M.; Haq, S.; Raval, R.; Hodgson, A., A One-Dimensional Ice Structure Built from Pentagons. *Nat. Mater.* **2009,** *8*, 427-31.

57. Doering, D. L.; Madey, T. E., The Adsorption of Water on Clean and Oxygen-Dosed Ru(011). *Surf. Sci.* **1982,** *123*, 305-337.

58. Tatarkhanov, M.; Ogletree, D. F.; Rose, F.; Mitsui, T.; Fomin, E.; Maier, S.; Rose, M.; Cerda, J. I.; Salmeron, M., Metal- and Hydrogen-Bonding Competition During Water Adsorption on Pd(111) and Ru(0001). *J. Am. Chem. Soc.* **2009,** *131*, 18425-34.

59. Leenaerts, O.; Partoens, B.; Peeters, F. M., Water on Graphene: Hydrophobicity and Dipole Moment Using Density Functional Theory. *Phys. Rev. B* **2009,** *79*, 235440.

60. Li, H.; Zeng, X. C., Two Dimensional Epitaxial Water Adlayer on Mica with Graphene Coating: An Ab Initio Molecular Dynamics Study. *J. Chem. Theory Comput.* **2012,** *8*, 3034-43.

61. Kim, J. S.; Choi, J. S.; Lee, M. J.; Park, B. H.; Bukhvalov, D.; Son, Y. W.; Yoon, D.; Cheong, H.; Yun, J. N.; Jung, Y.*, et al.*, Between Scylla and Charybdis: Hydrophobic Graphene-Guided Water Diffusion on Hydrophilic Substrates. *Sci. Rep.* **2013,** *3*, 2309.

62. Bampoulis, P.; Sotthewes, K.; Siekman, M. H.; Zandvliet, H. J.; Poelsema, B., Graphene Visualizes the Ion Distribution on Air-Cleaved Mica. *Sci. Rep.* **2017,** *7*, 43451.

63. Malard, L. M.; Pimenta, M. A.; Dresselhaus, G.; Dresselhaus, M. S., Raman Spectroscopy in Graphene. *Phys. Rep.* **2009,** *473*, 51-87.

64. Castro Neto, A. H.; Guinea, F.; Peres, N. M. R.; Novoselov, K. S.; Geim, A. K., The

Electronic Properties of Graphene. *Rev. Mod. Phys.* **2009,** *81*, 109-162.

65. Novoselov, K. S.; Geim, A. K.; Morozov, S. V.; Jiang, D.; Katsnelson, M. I.; Grigorieva, I. V.; Dubonos, S. V.; Firsov, A. A., Two-Dimensional Gas of Massless Dirac Fermions in Graphene. *Nature* **2005,** *438*, 197-200.

66. Chen, W.; Qi, D.; Gao, X.; Wee, A. T. S., Surface Transfer Doping of Semiconductors. *Prog. Surf. Sci.* **2009,** *84*, 279-321.

67. Zhu, Y.; Murali, S.; Cai, W.; Li, X.; Suk, J. W.; Potts, J. R.; Ruoff, R. S., Graphene and Graphene Oxide: Synthesis, Properties, and Applications. *Adv. Mater.* **2010,** *22*, 3906-24.

68. Nair, R. R.; Blake, P.; Grigorenko, A. N.; Novoselov, K. S.; Booth, T. J.; Stauber, T.; Peres, N. M.; Geim, A. K., Fine Structure Constant Defines Visual Transparency of Graphene. *Science* **2008,** *320*, 1308.

69. Dorn, M.; Lange, P.; Chekushin, A.; Severin, N.; Rabe, J. P., High Contrast Optical Detection of Single Graphenes on Optically Transparent Substrates. *J. Appl. Phys.* **2010,** *108*, 106101.

70. Ferrari, A. C.; Meyer, J. C.; Scardaci, V.; Casiraghi, C.; Lazzeri, M.; Mauri, F.; Piscanec, S.; Jiang, D.; Novoselov, K. S.; Roth, S*., et al.*, Raman Spectrum of Graphene and Graphene Layers. *Phys. Rev. Lett.* **2006,** *97*, 187401.

71. Poppa, H.; Elliot, A. G., The Surface Composition of Mica Substrates. *Surf. Sci.* **1971,** *24*, 149-163.

72. Drake, B.; Prater, C. B.; Weisenhorn, A. L.; Gould, S. A.; Albrecht, T. R.; Quate, C. F.; Cannell, D. S.; Hansma, H. G.; Hansma, P. K., Imaging Crystals, Polymers, and Processes in Water with the Atomic Force Microscope. *Science* **1989,** *243*, 1586-9.

73. Mogg, L.; Hao, G. P.; Zhang, S.; Bacaksiz, C.; Zou, Y. C.; Haigh, S. J.; Peeters, F. M.; Geim, A. K.; Lozada-Hidalgo, M., Atomically Thin Micas as Proton-Conducting Membranes. *Nat. Nanotechnol.* **2019,** *14*, 962-966.

74. Raviv, U.; Laurat, P.; Klein, J., Fluidity of Water Confined to Subnanometre Films. *Nature* **2001,** *413*, 51-4.

75. Rezania, B.; Dorn, M.; Severin, N.; Rabe, J. P., Influence of Graphene Exfoliation on the Properties of Water-Containing Adlayers Visualized by Graphenes and Scanning Force Microscopy. *J. Colloid Interface Sci.* **2013,** *407*, 500-4.

76. McCreery, R. L., *Raman Spectroscopy for Chemical Analysis*. Wiley Intersci.: New

York, **2000**; Vol. 157, p 1-5.

77. Ferrari, A. C., Raman Spectroscopy of Graphene and Graphite: Disorder, Electron–Phonon Coupling, Doping and Nonadiabatic Effects. *Solid State Commun.* **2007,** *143*, 47-57.

78. Ferraro, J. R.; Nakamoto, K.; Brown, C. W., Basic Theory. In *Introductory Raman Spectroscopy*, Academic Press: San Diego, **2003**; pp 1-94.

79. Bampoulis, P.; Sotthewes, K.; Dollekamp, E.; Poelsema, B., Water Confined in Two-Dimensions: Fundamentals and Applications. *Surf. Sci. Rep.* **2018,** *73*, 233-264.

80. Odelius, M.; Bernasconi, M.; Parrinello, M., Two Dimensional Ice Adsorbed on Mica Surface. *Phys. Rev. Lett.* **1997,** *78*, 2855-2858.

81. Beams, R.; Gustavo Cancado, L.; Novotny, L., Raman Characterization of Defects and Dopants in Graphene. *J. Condens. Matter Phys.* **2015,** *27*, 083002.

82. Reich, S.; Thomsen, C., Raman Spectroscopy of Graphite. *Philos. Trans. R. Soc. A* **2004,** *362*, 2271-88.

83. Ferrari, A. C.; Basko, D. M., Raman Spectroscopy as a Versatile Tool for Studying the Properties of Graphene. *Nat. Nanotechnol.* **2013,** *8*, 235-46.

84. Casiraghi, C.; Pisana, S.; Novoselov, K. S.; Geim, A. K.; Ferrari, A. C., Raman Fingerprint of Charged Impurities in Graphene. *Appl. Phys. Lett.* **2007,** *91*, 233108.

85. Pisana, S.; Lazzeri, M.; Casiraghi, C.; Novoselov, K. S.; Geim, A. K.; Ferrari, A. C.; Mauri, F., Breakdown of the Adiabatic Born-Oppenheimer Approximation in Graphene. *Nat. Mater.* **2007,** *6*, 198-201.

86. Das, A.; Pisana, S.; Chakraborty, B.; Piscanec, S.; Saha, S. K.; Waghmare, U. V.; Novoselov, K. S.; Krishnamurthy, H. R.; Geim, A. K.; Ferrari, A. C*., et al.*, Monitoring Dopants by Raman Scattering in an Electrochemically Top-Gated Graphene Transistor. *Nat. Nanotechnol.* **2008,** *3*, 210-5.

87. Piscanec, S.; Lazzeri, M.; Mauri, F.; Ferrari, A. C.; Robertson, J., Kohn Anomalies and Electron-Phonon Interactions in Graphite. *Phys. Rev. Lett.* **2004,** *93*, 185503.

88. Casiraghi, C., Raman Intensity of Graphene. *Phys. Status Solidi B* **2011,** *248*, 2593-2597.

89. Mohiuddin, T. M. G.; Lombardo, A.; Nair, R. R.; Bonetti, A.; Savini, G.; Jalil, R.; Bonini, N.; Basko, D. M.; Galiotis, C.; Marzari, N*., et al.*, Uniaxial Strain in Graphene by Raman

Spectroscopy:Gpeak Splitting, Grüneisen Parameters, and Sample Orientation. *Phys. Rev. B* **2009,** *79*, 205433.

90. Zabel, J.; Nair, R. R.; Ott, A.; Georgiou, T.; Geim, A. K.; Novoselov, K. S.; Casiraghi, C., Raman Spectroscopy of Graphene and Bilayer under Biaxial Strain: Bubbles and Balloons. *Nano Lett.* **2012,** *12*, 617-21.

91. Huang, M.; Yan, H.; Chen, C.; Song, D.; Heinz, T. F.; Hone, J., Phonon Softening and Crystallographic Orientation of Strained Graphene Studied by Raman Spectroscopy. *Proc. Natl. Acad. Sci. U.S.A.* **2009,** *106*, 7304-8.

92. Yoon, D.; Son, Y. W.; Cheong, H., Strain-Dependent Splitting of the Double-Resonance Raman Scattering Band in Graphene. *Phys. Rev. Lett.* **2011,** *106*, 155502.

93. Lee, J. E.; Ahn, G.; Shim, J.; Lee, Y. S.; Ryu, S., Optical Separation of Mechanical Strain from Charge Doping in Graphene. *Nat. Commun.* **2012,** *3*, 1024.

94. Metten, D.; Federspiel, F.; Romeo, M.; Berciaud, S., All-Optical Blister Test of Suspended Graphene Using Micro-Raman Spectroscopy. *Phys. Rev. Appl.* **2014,** *2*, 054008.

95. Das, A.; Chakraborty, B.; Piscanec, S.; Pisana, S.; Sood, A. K.; Ferrari, A. C., Phonon Renormalization in Doped Bilayer Graphene. *Phys. Rev. B* **2009,** *79*, 155417.

96. Froehlicher, G.; Berciaud, S., Raman Spectroscopy of Electrochemically Gated Graphene Transistors: Geometrical Capacitance, Electron-Phonon, Electron-Electron, and Electron-Defect Scattering. *Phys. Rev. B* **2015,** *91*, 205413.

97. Armano, A.; Buscarino, G.; Cannas, M.; Gelardi, F. M.; Giannazzo, F.; Schilirò, E.; Agnello, S., Monolayer Graphene Doping and Strain Dynamics Induced by Thermal Treatments in Controlled Atmosphere. *Carbon* **2018,** *127*, 270-279.

98. Bluhm, H.; Inoue, T.; Salmeron, M., Formation of Dipole-Oriented Water Films on Mica Substrates at Ambient Conditions. *Surf. Sci.* **2000,** *462*, L599-L602.

99. Goncher, S. J.; Zhao, L.; Pasupathy, A. N.; Flynn, G. W., Substrate Level Control of the Local Doping in Graphene. *Nano Lett.* **2013,** *13*, 1386-92.

100. Levesque, P. L.; Sabri, S. S.; Aguirre, C. M.; Guillemette, J.; Siaj, M.; Desjardins, P.; Szkopek, T.; Martel, R., Probing Charge Transfer at Surfaces Using Graphene Transistors. *Nano Lett.* **2011,** *11*, 132-7.

101. Schedin, F.; Geim, A. K.; Morozov, S. V.; Hill, E. W.; Blake, P.; Katsnelson, M. I.; Novoselov, K. S., Detection of Individual Gas Molecules Adsorbed on Graphene. *Nat.*

Mater. **2007,** *6*, 652-5.

102. Couto, N. J. G.; Costanzo, D.; Engels, S.; Ki, D.-K.; Watanabe, K.; Taniguchi, T.; Stampfer, C.; Guinea, F.; Morpurgo, A. F., Random Strain Fluctuations as Dominant Disorder Source for High-Quality on-Substrate Graphene Devices. *Phys. Rev. X.* **2014,** *4*, 041019.

103. Shaina, P. R.; George, L.; Yadav, V.; Jaiswal, M., Estimating the Thermal Expansion Coefficient of Graphene: The Role of Graphene-Substrate Interactions. *J. Condens. Matter Phys.* **2016,** *28*, 085301.

104. Bluhm, H.; Inoue, T.; Salmeron, M., Friction of Ice Measured Using Lateral Force Microscopy. *Phys. Rev. B* **2000,** *61*, 7760-7765.

105. Ikari, M. J.; Saffer, D. M.; Marone, C., Effect of Hydration State on the Frictional Properties of Montmorillonite-Based Fault Gouge. *J. Geophys. Res.* **2007,** *112*.

106. Schlaich, A.; Kappler, J.; Netz, R. R., Hydration Friction in Nanoconfinement: From Bulk Via Interfacial to Dry Friction. *Nano Lett.* **2017,** *17*, 5969-5976.

107. Ferraro, J. R.; Nakamoto, K.; Brown, C. W., Instrumentation and Experimental Techniques. In *Introductory Raman Spectroscopy*, Academic Press: San Diego, **2003**; pp 95-146.

108. Giridhar, G.; Manepalli, R. R. K. N.; Apparao, G., Confocal Raman Spectroscopy. In *Spectroscopic Methods for Nanomaterials Characterization*, Elsevier: **2017**; pp 141-161.

109. Binnig, G.; Quate, C. F.; Gerber, C., Atomic Force Microscope. *Phys. Rev. Lett.* **1986,** *56*, 930-933.

110. Cappella, B.; Dietler, G., Force-Distance Curves by Atomic Force Microscopy. *Surf. Sci. Rep.* **1999,** *34*, 1-104.

111. Jalili, N.; Laxminarayana, K., A Review of Atomic Force Microscopy Imaging Systems: Application to Molecular Metrology and Biological Sciences. *Mechatronics* **2004,** *14*, 907-945.

112. Lin, H.; Rauf, A.; Severin, N.; Sokolov, I. M.; Rabe, J. P., Influence of Interface Hydration on Sliding of Graphene and Molybdenum-Disulfide Single-Layers. *J. Colloid Interface Sci.* **2019,** *540*, 142-147.

113. Bampoulis, P.; Lohse, D.; Zandvliet, H. J. W.; Poelsema, B., Coarsening Dynamics of Ice Crystals Intercalated between Graphene and Supporting Mica. *Appl. Phys. Lett.* **2016,** *108*, 011601.

114. Schmitz, I.; Schreiner, M.; Friedbacher, G.; Grasserbauer, M., Phase Imaging as an Extension to Tapping Mode Afm for the Identification of Material Properties on Humidity-Sensitive Surfaces. *Appl. Surf. Sci.* **1997,** *115*, 190-198.

115. Algara-Siller, G.; Lehtinen, O.; Wang, F. C.; Nair, R. R.; Kaiser, U.; Wu, H. A.; Geim, A. K.; Grigorieva, I. V., Square Ice in Graphene Nanocapillaries. *Nature* **2015,** *519*, 443-5.

116. Burns, G., Surface Science. In *Solid State Phys.*, Academic Press: San Diego, **1985**; pp 671-712.

117. Venezuela, P.; Lazzeri, M.; Mauri, F., Theory of Double-Resonant Raman Spectra in Graphene: Intensity and Line Shape of Defect-Induced and Two-Phonon Bands. *Phys. Rev. B* **2011,** *84*, 035433.

118. Forster, F.; Molina-Sanchez, A.; Engels, S.; Epping, A.; Watanabe, K.; Taniguchi, T.; Wirtz, L.; Stampfer, C., Dielectric Screening of the Kohn Anomaly of Graphene on Hexagonal Boron Nitride. *Phys. Rev. B* **2013,** *88*, 085419.

119. Eckmann, A.; Park, J.; Yang, H.; Elias, D.; Mayorov, A. S.; Yu, G.; Jalil, R.; Novoselov, K. S.; Gorbachev, R. V.; Lazzeri, M.*, et al.*, Raman Fingerprint of Aligned Graphene/H-Bn Superlattices. *Nano Lett.* **2013,** *13*, 5242-6.

120. Shannon, R. D., Revised Effective Ionic Radii and Systematic Studies of Interatomic Distances in Halides and Chalcogenides. *Acta Crystallogr., Sect. A: Found. Crystallogr.* **1976,** *32*, 751-767.

121. Cheng, X.; Noh, Y.-Y.; Wang, J.; Tello, M.; Frisch, J.; Blum, R.-P.; Vollmer, A.; Rabe, J. P.; Koch, N.; Sirringhaus, H., Controlling Electron and Hole Charge Injection in Ambipolar Organic Field-Effect Transistors by Self-Assembled Monolayers. *Adv. Funct. Mater.* **2009,** *19*, 2407-2415.

122. Vilan, A.; Cahen, D., Chemical Modification of Semiconductor Surfaces for Molecular Electronics. *Chem. Rev.* **2017,** *117*, 4624-4666.

123. Nouchi, R., Dipolar Switching of Charge-Injection Barriers at Electrode/Semiconductor Interfaces as a Mechanism for Water-Induced Instabilities of Organic Devices. *Adv. Mater. Interfaces* **2018,** *5*, 1801261.

124. Lide, D. R., *Crc Handbook of Chemistry and Physics*. 84th ed.; CRC Press: **2004**; p 1376-1378.

125. Shin, S. H.; Kwon, Y. H.; Kim, Y. H.; Jung, J. Y.; Lee, M. H.; Nah, J., Triboelectric Charging Sequence Induced by Surface Functionalization as a Method to Fabricate High Performance Triboelectric Generators. *ACS Nano* **2015,** *9*, 4621-7.

126. Mestari, A.; Gaufrès, R.; Huguet, P., Behaviour of the Calibration of a Raman Spectrometer with Temperature Changes. *J. Raman Spectrosc.* **1997,** *28*, 785-789.

127. Sansonetti, J. E.; Martin, W. C., Handbook of Basic Atomic Spectroscopic Data. *J. Phys. Chem. Ref. Data* **2005,** *34*, 1559-2259.

128. Severin, N.; Sokolov, I. M.; Rabe, J. P., Dynamics of Ethanol and Water Mixtures Observed in a Self-Adjusting Molecularly Thin Slit Pore. *Langmuir* **2014,** *30*, 3455-9.

129. Rauf, A.; Cojal González, J. D.; Balkan, A.; Severin, N.; Sokolov, I. M.; Rabe, J. P., Shaping Surfaces and Interfaces of 2d Materials on Mica with Intercalating Water and Ethanol. *Mol. Phys.* **2021,** *119*, e1947534.

130. Wan, K.-T.; Smith, D. T.; Lawn, B. R., Fracture and Contact Adhesion Energies of Mica-Mica, Silica-Silica, and Mica-Silica Interfaces in Dry and Moist Atmospheres. *J. Am. Ceram. Soc.* **1992,** *75*, 667-676.

131. Guckenberger, R.; Heim, M.; Cevc, G.; Knapp, H. F.; Wiegrabe, W.; Hillebrand, A., Scanning Tunneling Microscopy of Insulators and Biological Specimens Based on Lateral Conductivity of Ultrathin Water Films. *Science* **1994,** *266*, 1538-40.

132. Xu, L.; Lio, A.; Hu, J.; Ogletree, D. F.; Salmeron, M., Wetting and Capillary Phenomena of Water on Mica. *J. Phys. Chem. B* **1998,** *102*, 540-548.

133. Revilla, R. I.; Yang, Y.-L.; Wang, C., Local Surface Charge Dissipation Studied Using Force Spectroscopy Method of Atomic Force Microscopy. *Surf. Interface Anal.* **2015,** *47*, 657-662.

134. Freitas, R. R.; Rivelino, R.; Mota Fde, B.; de Castilho, C. M., Dft Studies of the Interactions of a Graphene Layer with Small Water Aggregates. *J. Phys. Chem. A* **2011,** *115*, 12348-56.

135. Kozbial, A.; Li, Z.; Sun, J.; Gong, X.; Zhou, F.; Wang, Y.; Xu, H.; Liu, H.; Li, L., Understanding the Intrinsic Water Wettability of Graphite. *Carbon* **2014,** *74*, 218-225.

136. Kozbial, A.; Zhou, F.; Li, Z.; Liu, H.; Li, L., Are Graphitic Surfaces Hydrophobic? *Acc. Chem. Res.* **2016,** *49*, 2765-2773.

137. Schmickler, W., Tunneling of Electrons through Thin Layers of Water. *Surf. Sci.* **1995,** *335*, 416-421.

138. Hahn, J. R.; Hong, Y. A.; Kang, H., Electron Tunneling across an Interfacial Water Layer inside an Stm Junction: Tunneling Distance, Barrier Height and Water Polarization Effect. *Appl. Phys. A* **1998,** *66*, S467-S472.

139. Eckmann, A.; Felten, A.; Mishchenko, A.; Britnell, L.; Krupke, R.; Novoselov, K. S.; Casiraghi, C., Probing the Nature of Defects in Graphene by Raman Spectroscopy. *Nano Lett.* **2012,** *12*, 3925-30.

140. Rudenko, A. N.; Keil, F. J.; Katsnelson, M. I.; Lichtenstein, A. I., Graphene Adhesion on Mica: Role of Surface Morphology. *Phys. Rev. B* **2011,** *83*, 045409.

141. Davidson, A. T.; Vickers, A. F., The Optical Properties of Mica in the Vacuum Ultraviolet. *J. Phys. Condens. Matter* **1972,** *5*, 879-887.

142. Kristianpoller, N.; Kirsh, Y.; Shoval, S.; Weiss, D.; Chen, R., Thermoluminescent Properties of Mica. *Int. J. Radiat. Appl. Instrum. D* **1988,** *14*, 101-104.

143. Kalita, J. M.; Wary, G., Estimation of Band Gap of Muscovite Mineral Using Thermoluminescence (Tl) Analysis. *Physica B Condens. Matter* **2016,** *485*, 53-59.

144. Seol, M.; Kim, S.; Cho, Y.; Byun, K. E.; Kim, H.; Kim, J.; Kim, S. K.; Kim, S. W.; Shin, H. J.; Park, S., Triboelectric Series of 2d Layered Materials. *Adv. Mater.* **2018,** *30*, e1801210.

145. Miranda, P. B.; Xu, L.; Shen, Y. R.; Salmeron, M., Icelike Water Monolayer Adsorbed on Mica at Room Temperature. *Phys. Rev. Lett.* **1998,** *81*, 5876-5879.

146. Malani, A.; Ayappa, K. G., Adsorption Isotherms of Water on Mica: Redistribution and Film Growth. *J. Phys. Chem. B* **2009,** *113*, 1058-67.

147. McCreary, A.; Ghosh, R.; Amani, M.; Wang, J.; Duerloo, K. A.; Sharma, A.; Jarvis, K.; Reed, E. J.; Dongare, A. M.; Banerjee, S. K*., et al.*, Effects of Uniaxial and Biaxial Strain on Few-Layered Terrace Structures of Mos(2) Grown by Vapor Transport. *ACS Nano* **2016,** *10*, 3186-97.

148. Gong, L.; Kinloch, I. A.; Young, R. J.; Riaz, I.; Jalil, R.; Novoselov, K. S., Interfacial Stress Transfer in a Graphene Monolayer Nanocomposite. *Adv. Mater.* **2010,** *22*, 2694-7.

149. Savage, R. H., Graphite Lubrication. *J. Appl. Phys.* **1948,** *19*, 1-10.

150. Levita, G.; Righi, M. C., Effects of Water Intercalation and Tribochemistry on Mos2 Lubricity: An Ab Initio Molecular Dynamics Investigation. *Chemphyschem* **2017,** *18*, 1475-1480.

151. Conley, H. J.; Wang, B.; Ziegler, J. I.; Haglund, R. F., Jr.; Pantelides, S. T.; Bolotin, K. I., Bandgap Engineering of Strained Monolayer and Bilayer Mos2. *Nano Lett.* **2013,** *13*, 3626-30.

152. Zhu, C. R.; Wang, G.; Liu, B. L.; Marie, X.; Qiao, X. F.; Zhang, X.; Wu, X. X.; Fan, H.; Tan, P. H.; Amand, T*., et al.*, Strain Tuning of Optical Emission Energy and Polarization in Monolayer and Bilayer Mos_2. *Phys. Rev. B* **2013,** *88*, 121301.

153. Tongay, S.; Zhou, J.; Ataca, C.; Liu, J.; Kang, J. S.; Matthews, T. S.; You, L.; Li, J.; Grossman, J. C.; Wu, J., Broad-Range Modulation of Light Emission in Two-Dimensional Semiconductors by Molecular Physisorption Gating. *Nano Lett.* **2013,** *13*, 2831-6.

154. Lin, Y.; Ling, X.; Yu, L.; Huang, S.; Hsu, A. L.; Lee, Y. H.; Kong, J.; Dresselhaus, M. S.; Palacios, T., Dielectric Screening of Excitons and Trions in Single-Layer Mos2. *Nano Lett.* **2014,** *14*, 5569-76.

155. Mak, K. F.; He, K.; Lee, C.; Lee, G. H.; Hone, J.; Heinz, T. F.; Shan, J., Tightly Bound Trions in Monolayer Mos2. *Nat. Mater.* **2013,** *12*, 207-11.

156. Mouri, S.; Miyauchi, Y.; Matsuda, K., Tunable Photoluminescence of Monolayer Mos(2) Via Chemical Doping. *Nano Lett.* **2013,** *13*, 5944-8.

157. He, K.; Poole, C.; Mak, K. F.; Shan, J., Experimental Demonstration of Continuous Electronic Structure Tuning Via Strain in Atomically Thin Mos2. *Nano Lett.* **2013,** *13*, 2931-6.

158. Jiang, T.; Huang, R.; Zhu, Y., Interfacial Sliding and Buckling of Monolayer Graphene on a Stretchable Substrate. *Adv. Funct. Mater.* **2014,** *24*, 396-402.

159. Wang, G.; Dai, Z.; Liu, L.; Hu, H.; Dai, Q.; Zhang, Z., Tuning the Interfacial Mechanical Behaviors of Monolayer Graphene/Pmma Nanocomposites. *ACS Appl. Mater. Interfaces* **2016,** *8*, 22554-62.

160. Memarian, F.; Fereidoon, A.; Darvish Ganji, M., Graphene Young's Modulus: Molecular Mechanics and Dft Treatments. *Superlattices Microstruct.* **2015,** *85*, 348-356.

161. Bernal, J. D.; Bragg, W. L., The Structure of Graphite. *Proc. R. Soc. London, Ser. A* **1997,** *106*, 749-773.

Acknowledgments

I would like to express my gratitude to the following individuals for their help and support:

My supervisor, **Prof. Jürgen P. Rabe,** has supervised all of my work. He not only gave me many valuable advice and instructions for my experimental research, but also trained my skills in scholar writing and presentations. This must be greatly beneficial for my future career. Most importantly, I am very grateful for his huge effort in searching for funding to cover my whole doctoral research and meanwhile support the living of my family in Berlin. I would not have finished this work without the financial support he found from *International Max Planck Research Schools (IMPRS)*, Collaborative Research Centre 951 (CRC 951) and *Integrative Research Institute for the Sciences* (*IRIS Adlershof)*.

Prof. Igor M. Sokolov provided the most theoretical support for interpretations of my experimental results. I was deeply impressed with his rich knowledge of physics. I appreciated him for his patient and fruitful discussions in terms of my project. Besides, I would like to thank him again for his guidance on my study in the *Quantum Mechanics* course.

I would especially stress my great thankfulness to **Dr. Nikolai Severin** for his tons of aid throughout my entire research project, without which I would not have been able to complete my project in time. He taught me to use scientific instruments such as SFM, STM and different kinds of spectroscopy technologies. His detailed explanations helped me to better understand the working principle behind these instruments. Furthermore, he also conveyed a lot of knowledge in physics, skills about scientific writing and presentations to me. I feel so lucky to have him as both my best colleague and an excellent mentor.

I am also grateful for the help from **PD. Dr. Stephen Kirstein**. His extensive knowledge in physics, especially in the optical and quantum mechanics fields, also benefited me a lot. I could always find clear explanations from him when I had questions about optical spectroscopy.

Finally, I would like to thank **Dr. Jose D. Cojal Gonzales** for providing MD simulations and related discussions, as well as PMM members such as **Evi Poblenz**, **Abdul Rauf**, **M. Fardin Gholami** and **Dr. Bita Rezania**, for their kindness and help in these years. I am so fortunate to be a member of the PMM group.

Declaration

I declare that I have completed the thesis independently using only the aids and tools specified. The experimental work has been conducted by myself, the theoretical calculations and computer simulations done by my colleagues were acknowledged in the text. Some results contained in this thesis were published in the following journals, and all citations are appropriately indicated:

1. Lin, H.; Schilo, A.; Kamoka, A. R.; Severin, N.; Sokolov, I. M.; Rabe, J. P., Insight into the Wetting of a Graphene-Mica Slit Pore with a Monolayer of Water, *Physical Review B* **2017**, 95, 195414.

2. Lin, H.; Rauf, A.; Severin, N.; Sokolov, I. M.; Rabe, J. P., Influence of Interface Hydration on Sliding of Graphene and MoS_2 Single-Layers, *Journal of Colloid & Interface Science* **2019**, 540, 142-147.

3. Lin, H.; Cojal Gonzalez, J. D.; Severin, N.; Sokolov, I. M.; Rabe, J. P., Reversible Switching of Charge Transfer at the GrapheneMica Interface with Intercalating Molecules, *ACS Nano* **2020**, *14*, 11594-11604.

I have not applied for a doctor's degree in the doctoral subject elsewhere and do not hold a corresponding doctor's degree. I have taken due note of the Faculty of Mathematics and Natural Sciences Ph.D. Regulations, published in the Official Gazette of Humboldt-Universität zu Berlin no. 42/2018 on 11/07/2018.

Berlin, 1.3.2022